2016

Nucleation, Growth And Transformations In Dna Linked Colloidal Assemblies

Ian Collins Jenkins
University of Pennsylvania, jenkinsi@seas.upenn.edu

Nucleation, Growth And Transformations In Dna Linked Colloidal Assemblies

Abstract
The use of short, synthetic DNA strands to mediate self-assembly of a collection of colloidal particles into ordered structures is now quite well established experimentally. However, it is increasingly apparent that DNA-linked colloidal assemblies (DLCA) are subject to many of the processing challenges relevant to atomic materials, including kinetic barriers related to nucleation and growth, defect formation, and even diffusionless transformations between different crystal symmetries. Understanding, and ultimately controlling, these phenomena will be required to truly utilize this technology to make new materials.

Here, I describe a series of computational studies—based on a complementary suite of tools that includes Brownian dynamics, free energy calculations, vibrational mode theory, and hydrodynamic drag analysis—that address several issues related to the nucleation, growth, and stability of DNA-linked colloidal assemblies. The primary focus is on understanding the nature of the apparently enormous number of diffusionless solid-solid phase transformations that occur in crystallites assembled from DNA-functionalized colloidal particles. We find that the ubiquitous nature of these transformations is largely due to the short-ranged nature of DNA mediated interactions, which produces a panoply of zero-energy barrier pathways (or zero frequency vibrational modes) in a number of crystalline configurations. Furthermore, it is shown that hydrodynamic drag forces play a key role in biasing the transformations towards specific pathways, leading to unexpected order in the final arrangements. Additional studies also highlight how heterogeneity in the surface density of DNA strands grafted onto the particles may be used to improve nucleation and growth behavior, which is generally difficult in systems near the 'sticky-sphere' limit in which the interaction range is short relative to the particle size. In the final chapter of the thesis, a general and powerful technique is presented for extracting particle-particle interactions directly from particle trajectory data.

Degree Type
Dissertation

Degree Name
Doctor of Philosophy (PhD)

Graduate Group
Chemical and Biomolecular Engineering

First Advisor
Talid Sinno

Keywords
Colloids, DNA, Self-assembly

Subject Categories
Chemical Engineering

NUCLEATION, GROWTH AND TRANSFORMATIONS IN DNA LINKED COLLOIDAL ASSEMBLIES

Ian C. Jenkins

A DISSERTATION

in

Chemical and Biomolecular Engineering

Presented to the Faculties of the University of Pennsylvania

in

Partial Fulfillment of the Requirements for the

Degree of Doctor of Philosophy

2017

Supervisor of Dissertation

_____

Talid Sinno, Professor of Chemical and Biomolecular Engineering

Graduate Group Chairperson

_____

Dr. John C. Crocker, Professor of Chemical and Biomolecular Engineering

Dissertation Committee

Dr. Daeyeon Lee, Professor of Chemical and Biomolecular Engineering

Dr. John C. Crocker, Professor of Chemical and Biomolecular Engineering

Dr. Kathleen J. Stebe, Professor of Chemical and Biomolecular Engineering

Dr. Paulo E. Arratia, Professor of Mechanical Engineering & Applied Mechanics

ABSTRACT

NUCLEATION, GROWTH AND TRANSFORMATIONS IN DNA LINKED COLLOIDAL ASSEMBLIES

Ian C. Jenkins

Talid Sinno

The use of short, synthetic DNA strands to mediate self-assembly of a collection of colloidal particles into ordered structures is now quite well established experimentally. However, it is increasingly apparent that DNA-linked colloidal assemblies (DLCA) are subject to many of the processing challenges relevant to atomic materials, including kinetic barriers related to nucleation and growth, defect formation, and even diffusionless transformations between different crystal symmetries. Understanding, and ultimately controlling, these phenomena will be required to truly utilize this technology to make new materials.

Here, I describe a series of computational studies—based on a complementary suite of tools that includes Brownian dynamics, free energy calculations, vibrational mode theory, and hydrodynamic drag analysis—that address several issues related to the nucleation, growth, and stability of DNA-linked colloidal assemblies. The primary focus is on understanding the nature of the apparently enormous number of diffusionless solid-solid phase transformations that occur in crystallites assembled from DNA-functionalized colloidal particles. We find that the ubiquitous nature of these transformations is largely due to the short-ranged nature of DNA mediated interactions, which produces a panoply of zero-energy barrier pathways (or zero frequency vibrational modes) in a number of crystalline configurations. Furthermore, it is shown that

hydrodynamic drag forces play a key role in biasing the transformations towards specific pathways, leading to unexpected order in the final arrangements. Additional studies also highlight how heterogeneity in the surface density of DNA strands grafted onto the particles may be used to improve nucleation and growth behavior, which is generally difficult in systems near the 'sticky-sphere' limit in which the interaction range is short relative to the particle size. In the final chapter of the thesis, a general and powerful technique is presented for extracting particle-particle interactions directly from particle trajectory data.

TABLE OF CONTENTS

LIST OF ILLUSTRATIONS

1. INTRODUCTION

1.1 DNA Mediated Self-Assembly

Self-assembly is any process in which a system of distinct components spontaneously self-organizes into a larger, more complex, ordered structure. Self-assembly is found throughout nature, from ice crystals forming in water to the growth of nearly every living organism. The complexity of structures produced through such self-assembly processes greatly surpasses what can be designed and built manually. In order to match the level of complexity present in nature we must learn to use its primary tool, self-assembly.

The science of self-assembly has undergone significant development since its inception. A variety of approaches for producing component parts capable of both spontaneous and induced assembly have been developed, varying both with regard to the underlying mechanisms responsible for driving the assembly processes, such as electrostatics (1-3), magnetics (4-6), depletion effects (7), and even fluid flow (8), and the length-scale of the component particles, which range from the nano through the micro scale (9) and beyond (10). Through both experiment and simulation it has been demonstrated that human-designed self-assembling systems are capable of producing an enormous variety of structures and a significant amount of research has been done to optimize these systems both in regard to the robustness of the growth process and the accuracy of the final product structure (11-14).

One particular interaction mechanism which has demonstrated promise in guiding self-assembly is DNA hybridization. DNA hybridization occurs when two single

strands of DNA with complementary nucleotide sequences come into contact. Once in contact each individual complementary nucleotide base pair forms a hydrogen bond, linking the strands together. The hybridization of single-stranded DNA has been employed in a variety of ways to induce self-assembly behavior in in systems comprised purely of DNA as well as in systems in which other objects are guided by DNA. In the former case a wide variety of structures have been assembled, including nanotubes(15, 16), 2D crystals(17), 3D periodic arrays(18) as well as a variety of structures built from DNA bricks(19, 20) and origami(21-25). However, there are two significant drawbacks to using DNA in this manner. First, by relying entirely upon DNA as a construction material, you are limited to producing structures which exhibit the thermal, electrical and optical properties of DNA. Second, and more importantly, DNA is costly to produce, making large scale production of materials constructed entirely of DNA prohibitively expensive. It is possible to simultaneously avoid both of these issues by using a second, less expensive material, such as polystyrene, as the bulk material, while still relying on DNA to drive the self-assembly process. This second approach is the focus of my research.

In pioneering work performed by Mirkin *et al.(26)* and Alivisatos(27) gold nanoparticles were functionalized with DNA by exposing single-stranded DNA capped with a thiol group to the gold nanoparticles, which ranged in size from 1 to 13nm. The thiol groups covalently bonded to the surface of the gold nanoparticles, covering them with freely dangling single-stranded DNA brushes. In these examples, two non-complementary nucleotide sequences were used, with each gold nanoparticle exposed to only one of the two. Once prepared, the functionalized nanoparticles were exposed to free-floating DNA duplexes containing the two nucleotide sequences complementary to

those bonded to the nanoparticles. These duplexes were therefore designed to act as intermediates between the two particle species, allowing particles functionalized with different sequences to become connected by the DNA bridges. Once a suspension had been populated with duplexes and both particle species, the temperature of the system was reduced in order to allow hybridization between surface and duplex DNA to occur. The overall process used by Mirkin et al. is illustrated below in Figure 1.1. While the nanoparticles produced using this approach have proven useful in various biodiagnostic tools (28, 29), intercellular probes (30) and gene regulators (31), attempts at assembling them into ordered structures were not successful and only amorphous aggregates were obtained.

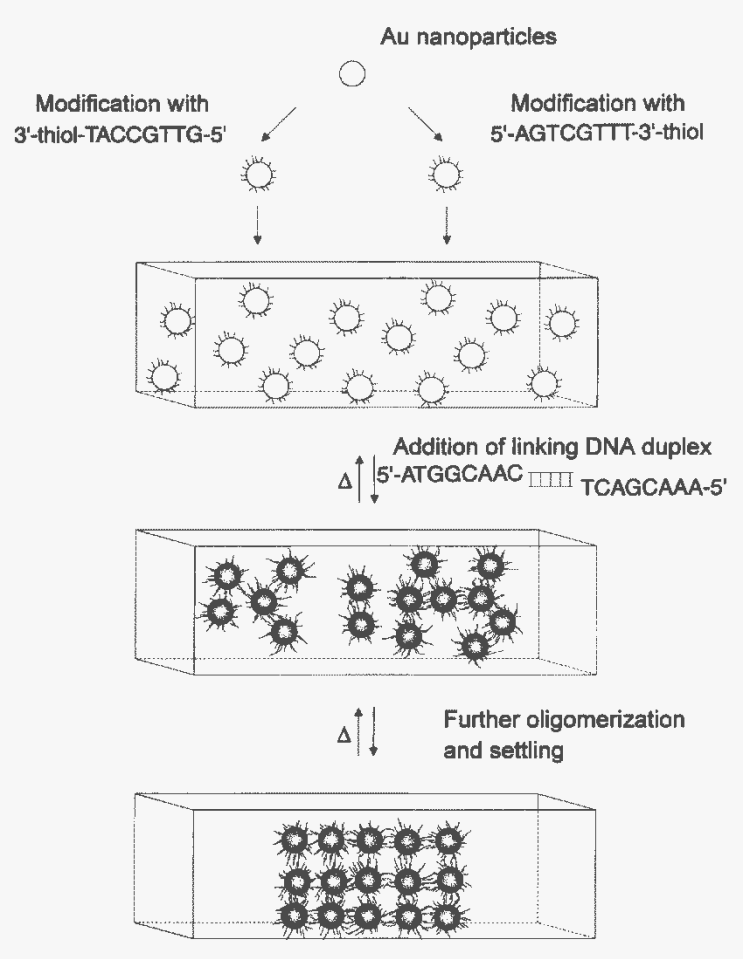

Figure 1.1. Repurposed from Ref. (26). Illustration of the process used by Mirking to assemble DNA functionalized colloidal particles.

The first successes in producing ordered crystallites of nanoparticles using DNA directed self-assembly came from the work of Nykypanchuk *et al (32).* and Park *et al (33).* In this work, flexible spacers made from non-complementary DNA oligomers were introduced between the gold-bonding thiol group and the duplex-complementary DNA sequences. These spacers increased the effective interaction range between the

particles, in turn allowing the self-assembly process to occur at much higher temperatures. At these higher temperatures DNA hybridization is reversible allowing the hybridized DNA to dynamically dissociate and reform. With the particles able to dynamically connect and disconnect, the growth of ordered crystallites becomes possible. Initially only two ordered crystal lattices were observed. The first, with face centered cubic (fcc) symmetry, occurred when only one species of single-stranded DNA was used to functionalize particles. In such a system, the freely floating duplexes are symmetric and interaction between all particles is identical. The second lattice, with body centered cubic (bcc) symmetry, was only observed in multi-component systems. Here, two particle-bound DNA species were employed, and each particle was functionalized with only a single type of DNA oligomer. In this particular binary system, the DNA sequences were chosen such that only particle pairs functionalized with different species of DNA were able to bond. The system used by Park *et al* is illustrated below in Figure 1.2.

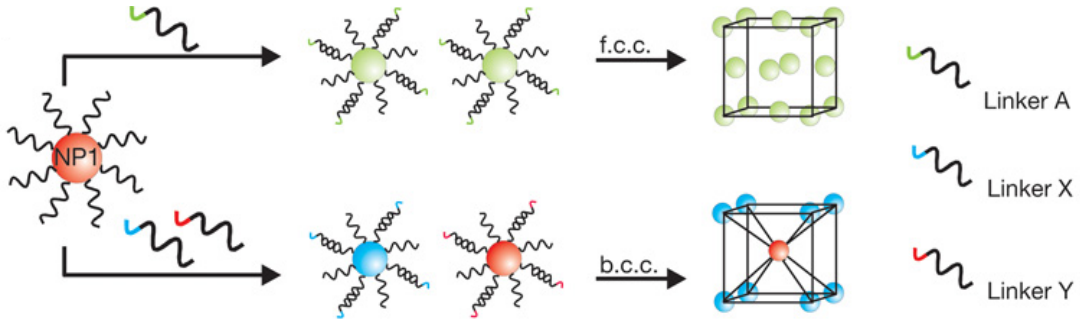

Figure 1.2: Repurposed from Ref. (33). Illustration of both the binary and single component systems used by Park et al which produce bcc and fcc respectively. The sticky end (colored section) of Linker A is self-complementary, while the sticky ends of Linker X and Y are only complementary with each other.

Although the work of Nykypanchuk *et al.* and Park *et al.* only resulted in two distinct nanoparticle crystal lattices, their results demonstrated that it is possible to target specific assembly structures by intelligently designing the DNA sequence grafter onto functionalized particles. Since then, a very large body of work has been done in further improving upon this basic approach in order to explore what crystal structures can be produced with the assembly of nanoparticles *(34-47).* Macfarlane *et al. (35)* in particular have demonstrated the viability of a significant number of ordered lattices including AlB_2, Cr_3Si and Cs_6C_{60}. In this work, three key design parameters were identified that were proposed to fully characterize a given system: particle size, lattice parameters, which are closely linked to particle interaction range and crystallographic symmetry. They also introduced a set of six rules which qualitatively link these particle design parameters to a number of crystalline properties. For example, their first rule states that when all particles in a system are of the same size, the system will tend to spontaneously assemble into a crystal which maximizes particle-particle contacts. A cartoon representation of how these three design parameters can be used, as well as an overview of the various crystalline lattices assembled from DNA functionalized particles, is shown below in Figure 1.3.

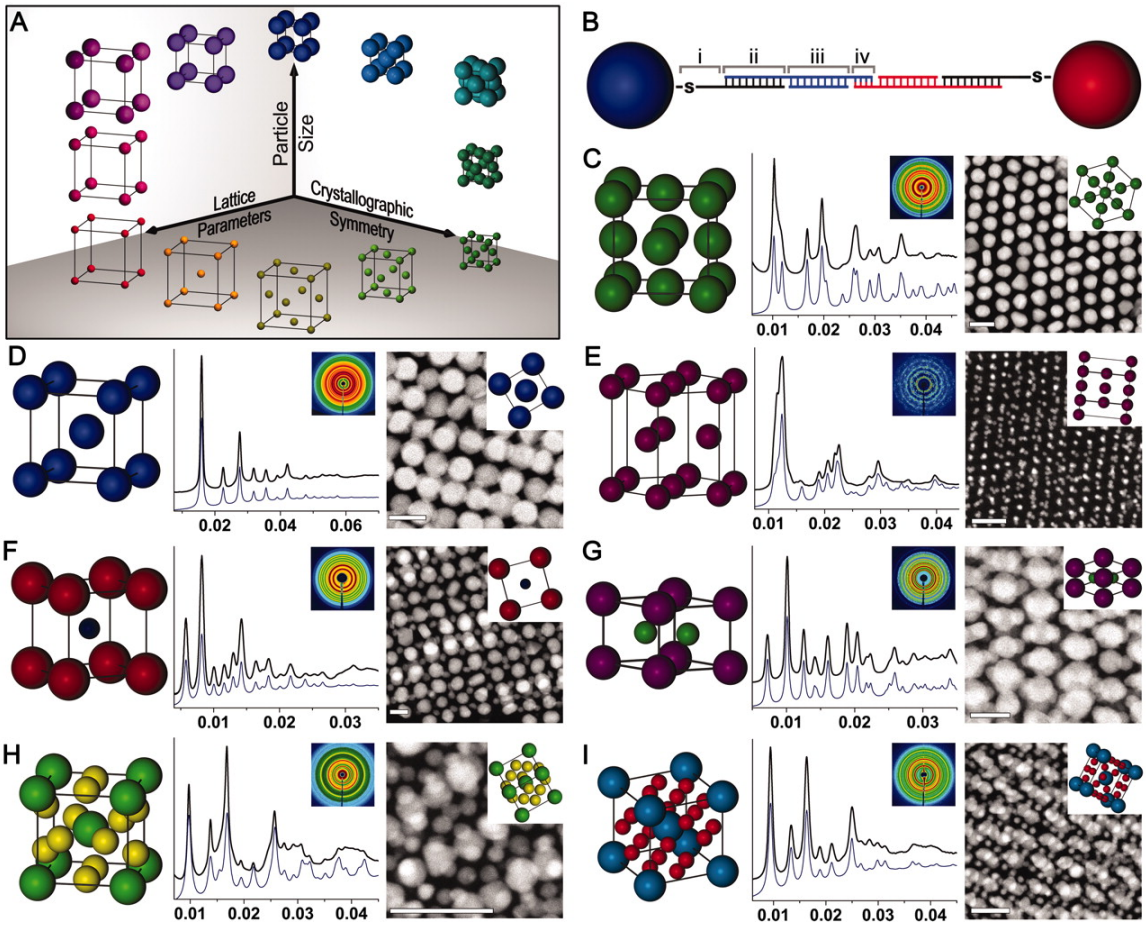

Figure 1.3: Repurposed from Ref. (35). (A) Illustration of how the three design parameters in the Macfarlane system: Lattice Parameters, Crystallographic Symmetry and Particle Size can be used to predict the structure of the lattice produced through spontaneous self-assembly. Also shown are a number of crystalline lattices which have been observed in systems of DNA functionalized nanoparticles: (C) fcc (D) bcc (E) hcp (F) CsCl (G) AlB_2 (H) Cr_3Si (I) Cs_6C_{60}.

There has also been parallel progress in extending DNA mediated self-assembly to micrometer scale particles (48-56). Generally speaking, the larger particle size to

interaction range ratio at these particle size scales makes ordered structures more difficult to grow, typically resulting in lower quality crystallites than are observed at the nanoscale. In large part this relative difficulty arises because micron-scale particles are closer to the 'sticky-sphere' limit (57) where entropic barriers act to slow down and inhibit assembly. On the other hand, micron-scale particles are of great interest for assembling ordered metamaterials (58) with interesting photonic and/or phononic properties. Although this goal has not yet been achieved, significant progress has been made in improving the crystallization behavior at this length-scale and identifying what crystal lattices are achievable. The work in this thesis is aimed precisely at elucidating the various mechanisms by which micron-scale particle assemblies nucleation, grow and transform.

Some of the first evidence for the viability of DNA mediated self-assembly at the micron scale was demonstrated by Crocker *et al (59, 60).* Their system of interest, was a bidisperse system with particles at diameters of 1.87μm and 1.1μm, the design of the particle-DNA construct was roughly equivalent to that used in the nanoscale studies. Rather than make use of free floating DNA duplexes to act as linkers, the nucleotide sequences were chosen such that the surface DNA oligomers could hybridize directly. A schematic representation of the linker-less system is shown below in Figure 1.4. Much like early attempts at producing ordered crystals at the nanoscale however, they were initially only successful at producing disordered aggregates.

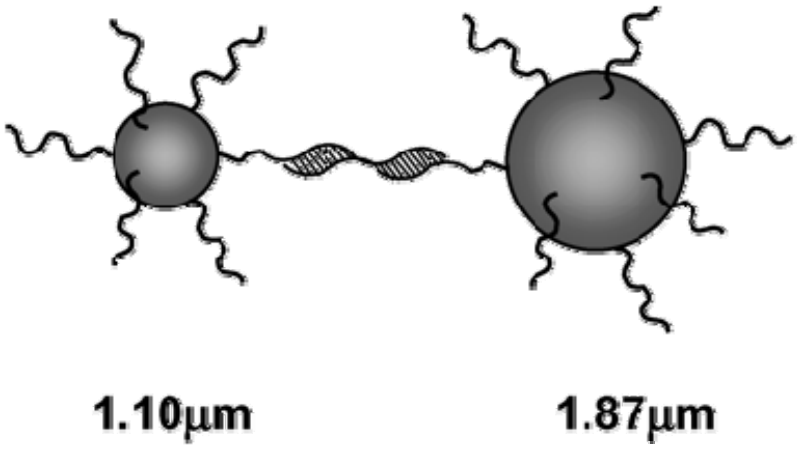

Figure 1.4: Adapted from Ref. (60). Schematic representation of direct hybridization between DNA on the surface of two micron-scale particles.

Further refinement of this approach came from the identification of polyethylene glycol (PEG) as an ideal material for constructing spacers, along with the introduction of linker-DNA, as previously described. These changes finally allowed for the production of large high quality crystallites (53). This technique was then expanded upon by adopting an approach based on DNA mixing (49). In this approach each particle is functionalized with two single stranded DNA sequences. The DNA sequences are chosen such that they are complementary with each other but not with themselves. Two types of particles are then defined according to the dominant DNA type on each particle type, such that type A particles are predominantly covered in type A DNA. This approach allows the binding strength between like and unlike particle pairs to be tuned independently by not only changing the DNA sequence and surface density, but also the degree of mixing. A overview of this approach is shown below in Figure 1.5.

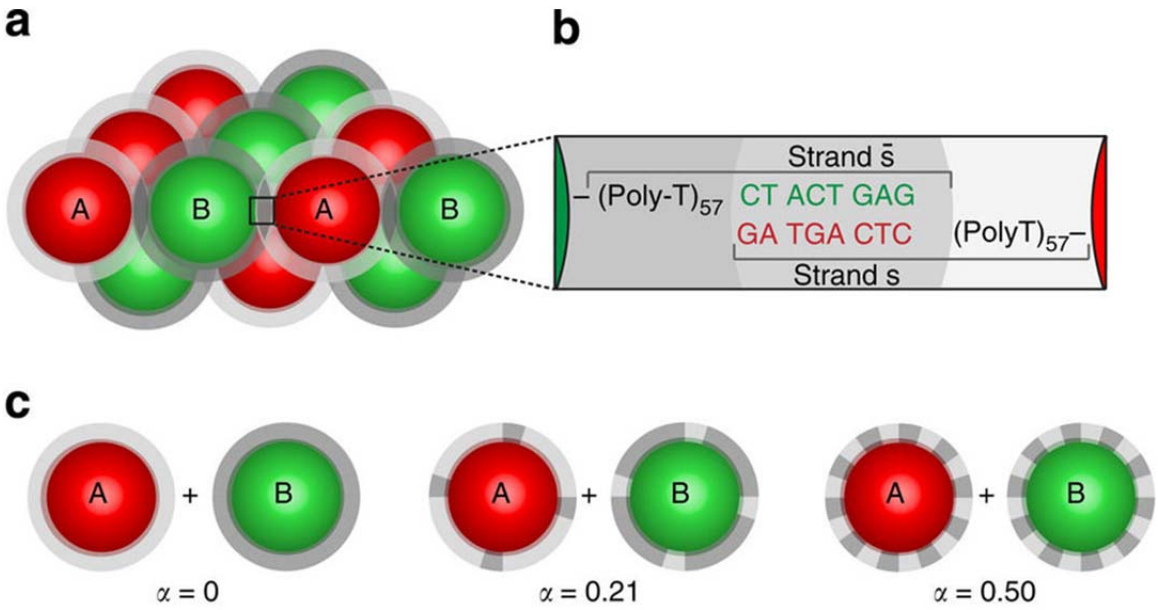

Figure 1.5: Adapted from Ref. (49). (A) Binary crystallite constructed from 400nm diameter particles. Interactions between particles are mediated by DNA hybridization, as shown in (B). (C) Cartoon representation of how binding strengths between unlike particle types can be controlled by modifying the density of complementary DNA on each particles surface. The *α* parameter is the mixing ratio, defined such that when *α* is 0 all DNA on the surface of type A particles is type A, and all DNA on the surface of type B particles is type B. At a mixing ratio of 0 particles of the same type have a binding strength of zero ($E_{AB} > E_{AA} = E_{BB} = 0$). A mixing ratio of 0.5 indicates both particle types have an even mix of the two DNA types on their surface. At a mixing ratio of 0.5 all particle binding strengths are equal ($E_{AB} = E_{AA} = E_{BB}$).

1.2 Numerical Simulations of DNA Functionalized Particles

Precisely and accurately constructing DNA functionalized particles at both the nano- and micro-scales is very challenging. Simulations offer a means to study these systems while avoiding this rather difficult assembly process. However, direct, explicit simulation of the various components of a system of DNA functionalized particles can be very computationally demanding. In order to successfully simulate such a system on a useful timescale, it is necessary to use a coarse grained model for the interactions between particles.

One common approach is to simulate the DNA oligomers using a method based on bead-spring polymer models (61, 62). One of the first examples of this approach is the model developed by Starr and Sciortino (63) which was designed to simulate the system studied by Stewart and McLaughlin (64). In this nanoscale system the DNA duplexes often used to mediate interactions between DNA functionalized particles are excluded. Instead, the single-stranded DNA sequences are chosen such that they are directly complementary. Additionally, each particle in this system is functionalized with only four strands of DNA in a tetragonal configuration. In the model each pair of neighboring monomers in a DNA strand are connected through a finitely-extensible, non-linear elastic anharmonic spring potential of the form

$$U_{FENE}(r) = -\frac{kR_0^2}{2}\ln\left(1-\left(\frac{r}{R_0}\right)^2\right). \qquad (1.1)$$

In addition to this two-body spring potential, a three body harmonic angular spring, dependent upon the angle between three sequential monomers of the form

$$U_\theta = k_l\left(1-\cos\left(\theta\right)\right), \tag{1.2}$$

is also included, limiting the flexibility of the strands. Each monomer in the DNA strand is also assigned a "bonding site". These bonding sites are each assigned a type: A, T, C or G and are connected to their associated monomer using the same anharmonic spring potential used to connect neighboring monomer sites. Interactions between binding sites are modeled using a truncated Lennard-Jones (LJ) potential. This potential is truncated differently depending upon the types of the interacting bonding sites. If the bonding sites are complementary, either A and T or C and G, the LJ potential is truncated at 2.5σ. However, if the bonding sites are non-complementary the LJ potential is truncated at 1.12 σ, such that the interaction is purely repulsive. A snapshot from a simulation using this model, in which the coarse-graining resolution is visible, is shown below in Figure 1.6.

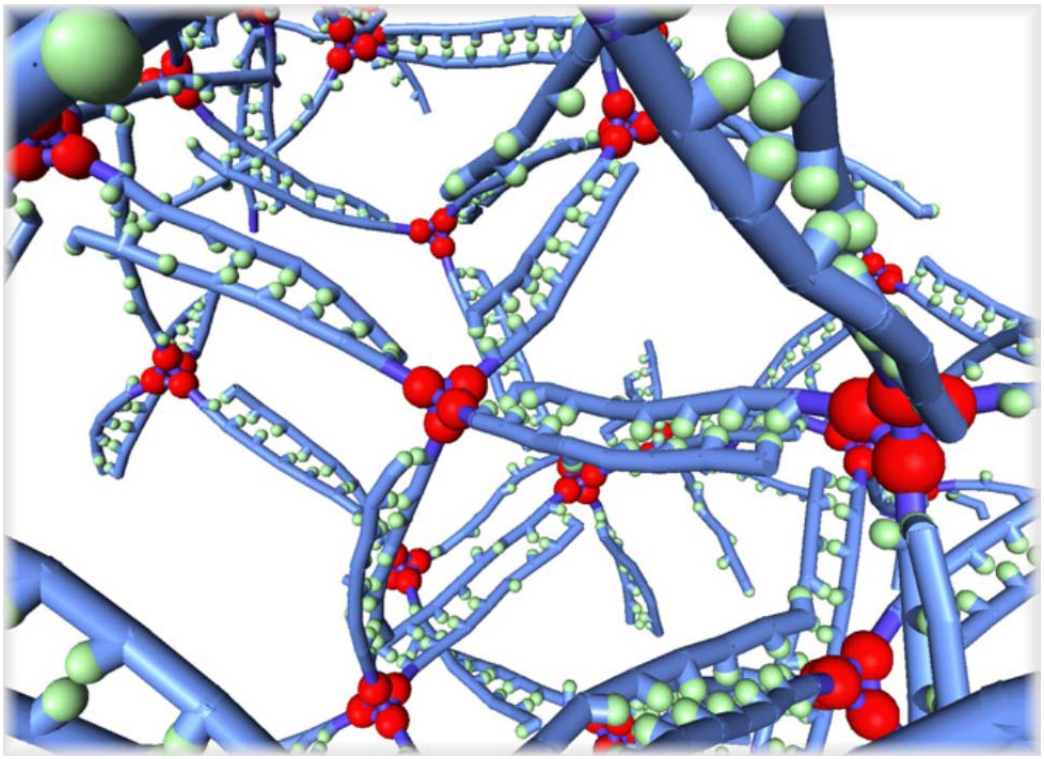

Figure 1.6: Repurposed from Ref. (63). Snapshot of a simulation utilizing the model proposed by Starr and Sciortino. The core of each functionalized particle is shown in red, single stranded DNA are shown in blue and bonding sites are shown in light green.

Another approach, developed by Knorowski, Burleigh, and Travesset(65) introduces “Flanker Beads” to the model of Star and Sciortino. These flanker beads sterically provide two improvements to the model. First, they prevent the simultaneous hybridization of three bases at a single site. Second, they provide directionality to the interaction between linker monomers, forcing hybridization between base pairs to occur perpendicular to the tangent of the single stranded DNA. In this model neighboring linker and spacer monomers are connected using a simple harmonic spring potential. Each linker monomer has an associated “central bead” (CT) to which it is also connected via a

harmonic spring. These CT units play a similar role to the bonding sites used by Starr and Sciortino (63). The CT units in neighboring linker monomers interact through a harmonic angular spring, designed to limit the flexibility of the linkers. Two flanker beads (FL) are attached to each CT via harmonic springs, along with a harmonic angular spring which is dependent on the angle between the two flankers and the central bead. LJ potentials are used to simulate interactions between non-adjacent linkers. Complementary linkers experience full LJ potentials while non-complementary linkers experience only the repulsive term in the LJ potential. In both cases the LJ potential is truncated at 3σ. A schematic representation of this model is shown below in Figure 1.7.

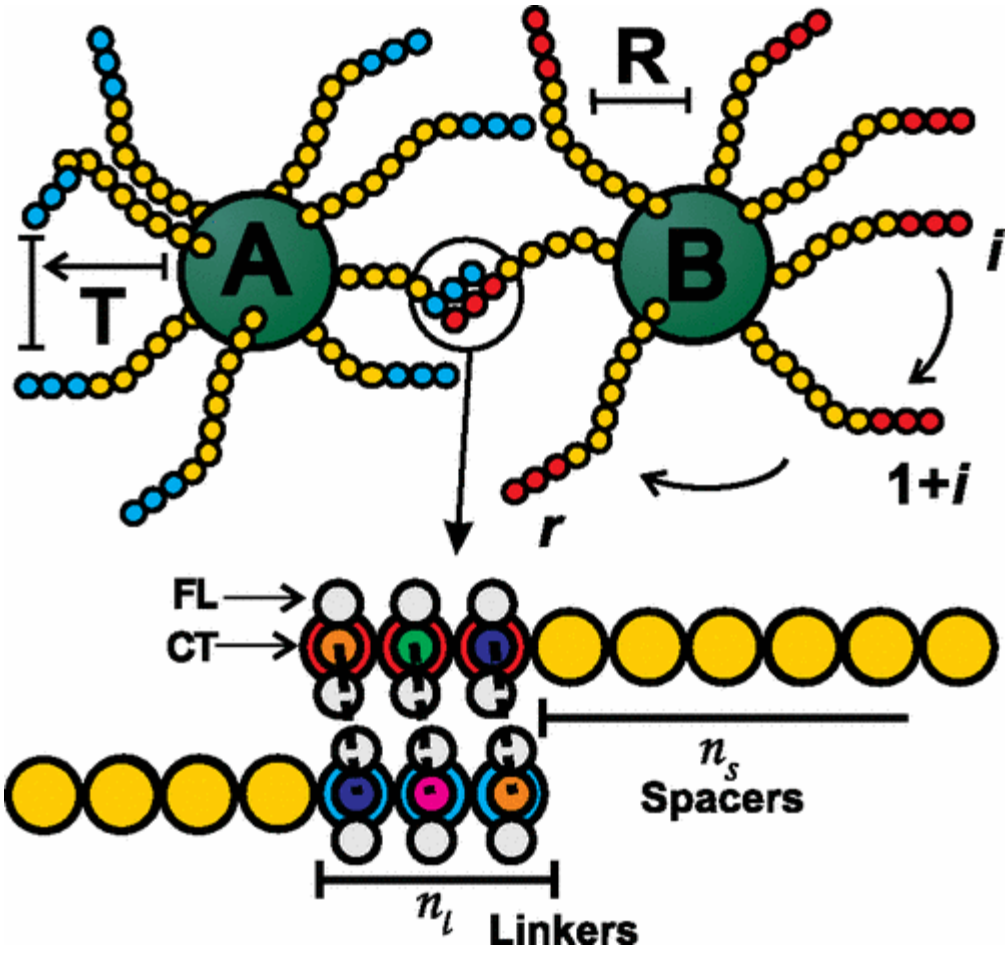

Figure 1.7: Repurposed from Ref. (65). Schematic representation of the model proposed by Knorowski, Burleigh, and Travesset. Each strand consists of n_s non-bonding spacer monomers and n_l bonding linker monomers. Each linker monomer is modeled with two flanker beads (FL) and a central bead (CT).

While these coarse grained models work well for nanoscale particles, where the number of DNA oligomers per particle is relatively small, they become numerically intractable at the microscale. As a result, many groups studying micron scale particles, as well as some studying nanoparticles with particularly dense DNA packing, make use

of more implicit, coarse grained models (65-79). One such model is used by Largo *et al.* (80) and Theodorakis *et al. (81)* in which Metropolis Monte Carlo (MMC) simulations of two DNA functionalized nanoparticles, simulated using the previously described approach developed by Starr and Sciortino (63), are used to generate statistical information about the relative orientation and center-to-center distance of pairs of particles. These statistics are then used to determine the probability of finding the system in any given configuration, where the configuration is assumed to be entirely described by the orientations of the two particles, (ϕ_1, ϕ_2) and their center-to-center distance. Here, ϕ_i is defined as the smallest angle between any DNA strand on particle i and the center-center vector between particles. This probability distribution, $p(r, \phi_1, \phi_2)$, is then used to calculate the effective potential between the two particles using the expression

$$U(r, \phi_1, \phi_2) = \frac{\ln\left(p(r, \phi_1, \phi_2)\right)}{\ln\left(p(r_\infty, \phi_1, \phi_2)\right)}, \tag{1.3}$$

where r_∞ is any distance beyond the maximum interaction range of the particles.

An entirely different approach to generating a coarse grained model is used by Leunissen and Frenkel (69). In their model they approximate interactions between DNA functionalized particles using large flat plates. These plates are randomly populated with double jointed rigid rods. The inner section of the rod represents the DNA spacer and is non-interacting, and allowed to freely swivel around its tethering point on the plate. The outer section of the rod represents the sticky, complementary, end of the DNA strand. It

is allowed to freely swivel about its connection to the inner rod and interacts with other outer rods according a two state potential: bound or unbound, such that there is a constant energy associated with binding. A schematic representation of this system is shown in Figure 1.8. Once two plates have been populated with these rods they are placed a fixed distance apart and Monte Carlo moves are proposed for the rods. These moves are made by first randomly selecting a rod, *i,* from one of the two plates. The list of all rods, *k,* on the opposing plate which are within range of rod *i* is then generated. Next the probability of rod *i* binding to any particular rod, *j,* is calculated as

$$p_{ij} = \frac{e^{\beta \Delta G_{ij}}}{1 + \sum_k e^{\beta \Delta G_{ik}}} \tag{1.4}$$

and the probability of forming no bond is

$$p_{i,unbound} = \frac{1}{1 + \sum_k e^{\beta \Delta G_{ik}}} \ , \tag{1.5}$$

where ΔG_{ij} is the free energy associated with the hybridization between rod *i* and rod *j*. The value of ΔG_{ij} is calculated using the expression

$$\Delta G_{ij} = \Delta G_{ij,solution} - k_B T \ln\left(\frac{\Omega_{ij}}{\Omega_j \Omega_i} \frac{1}{\rho_0} \right), \tag{1.6}$$

where Ω_i , Ω_j and Ω_{ij} are measures of the configuration space accessible to rod *i*, rod *j* and the bound *i-j* pair, respectively and ρ_0 is the number density of inner rods. The average free energy of the system is then calculated over many plate-plate separation

distances. The DNA interaction free energy as a function of separation distance can then be found using the expression

$$G(h) = -2k_B T \sum_N \ln\left(\frac{\Omega_{n,confined}}{\Omega_{n,unconfined}}\right) - \int_{\Delta G_{ik,solution}}^{0} \left\langle n_{bonds} \right\rangle_{\Delta G_{ik,solution},h} d\Delta G_{ik,solution} \,, \tag{1.7}$$

where $\left\langle n_{bonds} \right\rangle_{\Delta G_{ik,solution},h}$ is the number of pairs of hybridized DNA strands averaged over a specific value of $\Delta G_{ik,solution}$ and plate separation distance.

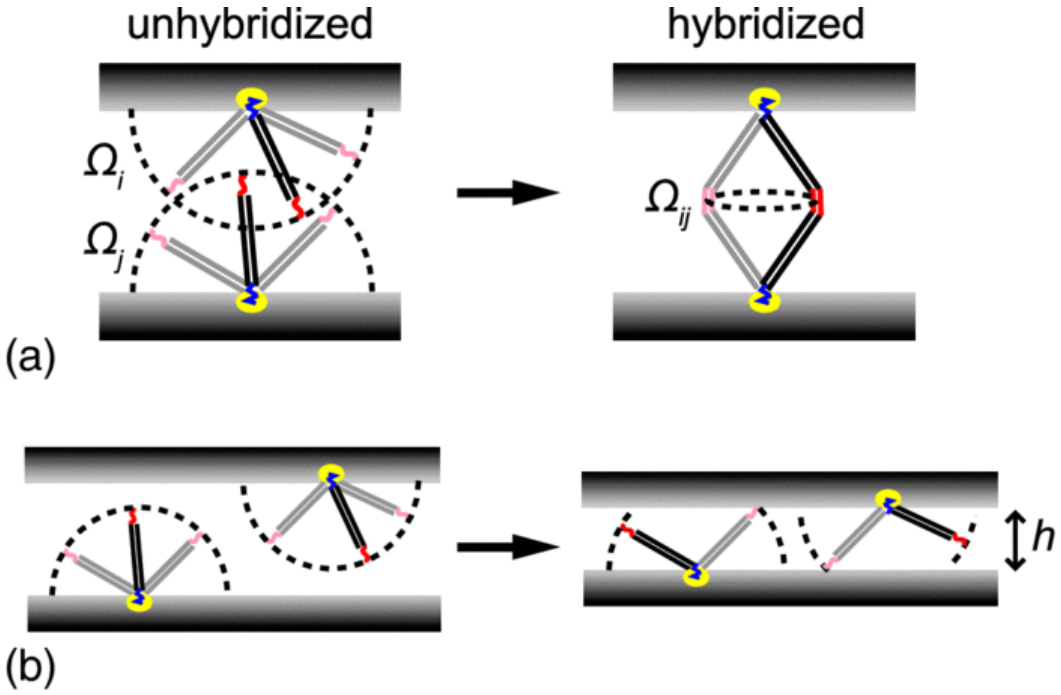

Figure 1.8: Repurposed from Ref. (69). Schematic representation of the model proposed Leunissen and Frenkel. Each DNA strand consists of two, freely-swiveling, rigid rods. The inner rod acts as a DNA spacer and is non-interacting. The outer rod acts as the sticky, binding end to a DNA oligomer. Two different cases are shown: a) when opposing rods are tethered such that they are able to interact and b) when opposing rods are

unable to interact. Ω_i , Ω_i and Ω_{ij} are the configuration spaces accessible to rod *i*, rod *j* and the bound *i-j* pair.

The coarse grained model I employ for all simulations reported in this thesis was developed and confirmed against experimental data by Rogers *et al*.(82). This coarse grained approach begins by proposing a model for describing two micron-scale DNA functionalized colloidal particles, separated by some fixed distance, *h.* While the most general calculation of the interaction potential between DNA-linked particles must include terms correcting for DNA polymer non-ideality and other terms in the partition function, (69, 70, 83), for the particular DNA configuration we use, an idealized model gives an acceptably accurate result (84, 85). Additionally, while smaller particles, whose interactions may be non-pairwise additive, require explicit polymer simulations to compute the effective interaction potential(86-88), the micron-scale spheres in this study, are large enough that their interactions are demonstrably pair-wise additive and implicit polymer models can be used.

The colloidal particles themselves are treated as hard spheres, such that the energy associated with overlap between a DNA strand and a colloidal particle is infinite. The single stranded DNA is treated as a tethered flexible chain with a contour length of 40nm, 8 times that of the Kuhn length of DNA (89). Upon initialization, the system contains no DNA, only the two hard spheres. Monte Carlo moves are then performed, in which a single move consists of eight randomly oriented steps starting from a random position on the surface of one of the hard sphere particles. This chain of 8 random walks represents a single configuration of a single DNA brush. The coordinate of the final segment in the DNA strand is recorded and binned spatially. With sufficient sampling this

binning process can be used to approximate the continuous number density of DNA in the region between the two particles. A schematic representation of this process is shown below in Figure 1.9. During this process it is necessary to record two other numbers: the number of proposed strands which do not intersect the anchor sphere, $\Omega_{\infty}(h)$ and the number of these strands which do not intersect with the opposing sphere, $\Omega(h)$. Due to the reversible nature of DNA bridge formation, it is assumed that the equilibrium concentration of DNA bridges between two particles can be calculated using the chemical equilibrium expression

$$C_{AB}(\mathbf{r}) = \frac{C_A(\mathbf{r})C_B(\mathbf{r})}{C_0} e^{-G_{hyb}/k_B T}, \tag{1.8}$$

along with the conservation equations

$$C_A^0(\mathbf{r}) = C_A(\mathbf{r}) + C_{AB}(\mathbf{r}) \tag{1.9}$$

and

$$C_B^0(\mathbf{r}) = C_B(\mathbf{r}) + C_{AB}(\mathbf{r}), \tag{1.10}$$

where G_{hyb} is the hybridization Gibbs free energy, $C_{AB}(\mathbf{r})$, $C_A(\mathbf{r})$ and $C_B(\mathbf{r})$ are the equilibrium concentrations of hybridized DNA, non-hybridized DNA from particle A and non-hybridized DNA from particle B, respectively, $C_A^0(\mathbf{r})$ and $C_B^0(\mathbf{r})$ are the values of $C_A(\mathbf{r})$ and $C_B(\mathbf{r})$ when no hybridization has occurred and C_0 is a reference concentration, set to 1M. Using the binned number densities gathered previously these equations can be solved to calculate $C_{AB}(\mathbf{r})$. Next, an expression relating the average

number of DNA bridges, $\left\langle N_{bridge} \right\rangle$ to the attraction interaction energy between the particles is invoked (90-92)

$$\frac{\Delta E_a}{k_B T} = -\left\langle N_{bridge} \right\rangle . \tag{1.11}$$

The value of $\left\langle N_{bridge} \right\rangle$, and therefore ΔE_a can be calculated by integrating over the spatial bins using the expression

$$\left\langle N_{bridge} \right\rangle = -N_{Av} \int d^3\mathbf{r} C_{AB}\left(\mathbf{r}\right), \tag{1.12}$$

where N_{Av} is Avagadro's number. Finally, the energy associated with entropic repulsion due to brush compression (90) can be calculated using the expression

$$\frac{\Delta E_r\left(h\right)}{k_B T} = -\ln\left(\frac{\Omega\left(h\right)}{\Omega_\infty\left(h\right)}\right). \tag{1.13}$$

The sum of $\Delta E_a\left(h\right)$ and $\Delta E_r\left(h\right)$ then gives the interaction energy between a pair of DNA functionalized particles separated by a distance *h*.

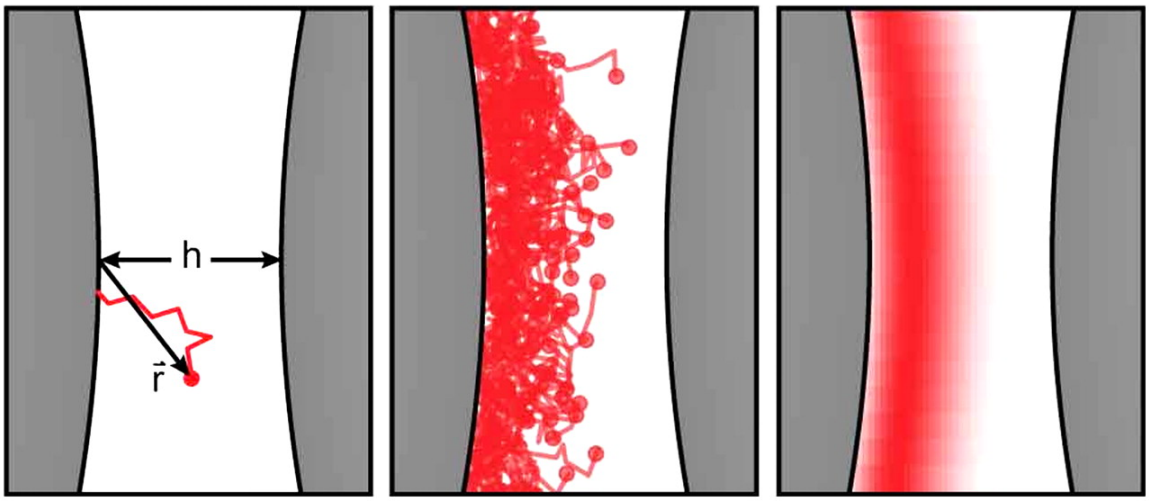

Figure 1.9: Repurposed from Ref. (82). Schematic representation of the method used to calculate the average number density of DNA. Left: A random walk is used to propose the configuration of a DNA brush. Center: Multiple random walks with uniformly distributed tethering points. Right: The final, averaged, DNA density profile, only the final coordinate in the random walk is used in the averaging process.

1.3 Thesis Outline

In this thesis I present my work studying the behavior of DNA functionalized particles ranging from 100nm to 1000nm in size using a complementary set of computational tools. The specific particles I simulate are based closely on the particles used in collaborative experimental work performed in the laboratory of Prof. John Crocker (49, 50, 59, 82, 93-96). In all of the work I present here I use the coarse-grained model of Rogers *et al*.(82) to simulate the behavior of these particles. In Chapter 2 I present a study of phase transformations in the binary CsCl superlattice. This study was inspired by an experimental observation which indicated a diffusionless (Martensitic)

transformation between the CsCl and CuAu superlattices was possible. Simulations revealed that due to the very low degree of rigidity in the CsCl superlattice, many such transformations are possible and that the final transformation observed in experiment is guided by hydrodynamic effects—which have largely been ignored in the literature. In Chapter 3 I demonstrate my work on the nucleation behavior of DNA functionalized colloidal particles. In particular, I focus on how their nucleation behavior can be improved by introducing a small amount of heterogeneity to the DNA surface density. This work is inspired by heretofore unexplained observations that certain chemistries for grafting DNA oligomers to particles have been more successful than others, even though the nominal DNA densities are similar. In Chapter 4 I expand upon the analysis of solid-solid phase transformations available to this self-assembly system and demonstrate how changing the relative size of particle types and particle-particle binding strengths enables additional diffusionless transformations which produce superlattices that are otherwise inaccessible by direct nucleation and growth. Finally, in Chapter 5, I will discuss a numerical approach for extracting particle-particle potential interaction profiles directly from non-equilibrium particle trajectory data.

2. A CASE STUDY: PHASE TRANSFORMATIONS IN CsCl SUPERLATTICES

2.1 Introduction

This study was inspired by a spontaneous bcc-to-fcc diffusionless (solid-solid) transformation experimentally observed by Casey et al. (49) in DNA-assembled, micron-scale, binary colloidal superlattice crystals. Although such transformations are well-studied in atomic materials because of their considerable technological importance (e.g., Martensitic transformation in steel hardening (97) and shape memory alloys (98)), their analysis in DLPAs is essentially non-existent. Understanding the nature of such transitions in colloidal assemblies may provide additional pathways for manipulating DLPAs to produce desired configurations that are otherwise difficult or impossible to access by direct nucleation.

The experimental system in question (49) consisted of two sub-populations of 400 nm diameter polystyrene particles, “A” and “B”, that were functionally differentiated by the composition of DNA oligomers grafted onto the particle surfaces. The two populations interact with binding energies that obey $E_{AB} \geq E_{AA}, E_{BB}$ and $E_{AA} = E_{BB}$, thereby generally favouring the formation of binary superlattice crystals over phase-separated single-component packings (32, 35, 49, 68, 99, 100).

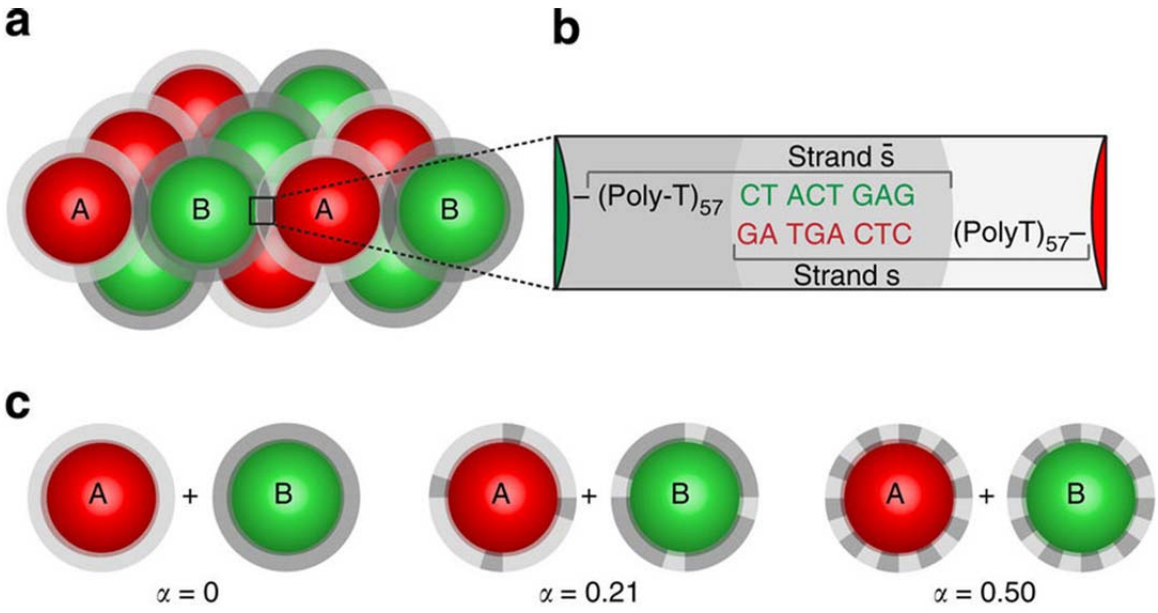

Figure 2.1: Adapted from Ref. (49). (A) Binary crystallite constructed from 400nm diameter particles. Interactions between particles are mediated by DNA hybridization, as shown in (B). (C) Cartoon representation of how binding strengths between unlike particle types can be controlled by modifying the density of complementary DNA on each particles surface. The *α* parameter is the mixing ratio, defined such that when *α* is 0 all DNA on the surface of type A particles is type A, and all DNA on the surface of type B particles is type B. At a mixing ratio of 0 particles of the same type have a binding strength of zero ($E_{AB} > E_{AA} = E_{BB} = 0$). A mixing ratio of 0.5 indicates both particle types have an even mix of the two DNA types on their surface. At a mixing ratio of 0.5 all particle binding strengths are equal ($E_{AB} = E_{AA} = E_{BB}$).

Crystallization experiments were performed by placing an equal number of A and B particles into solution and gradually cooling the system. Depending on the interaction

combination (E_{AB}, E_{AA}), it was found that annealed samples either yielded mixtures of two different types of well-ordered binary superlattice crystals, CsCl (bcc lattice type) and CuAu-I (fcc lattice type), or randomly substituted solid-solution crystals having a face-centered-cubic (fcc) structure (fcc-SS). Several examples of these crystallites are shown below in Figure 2.2.

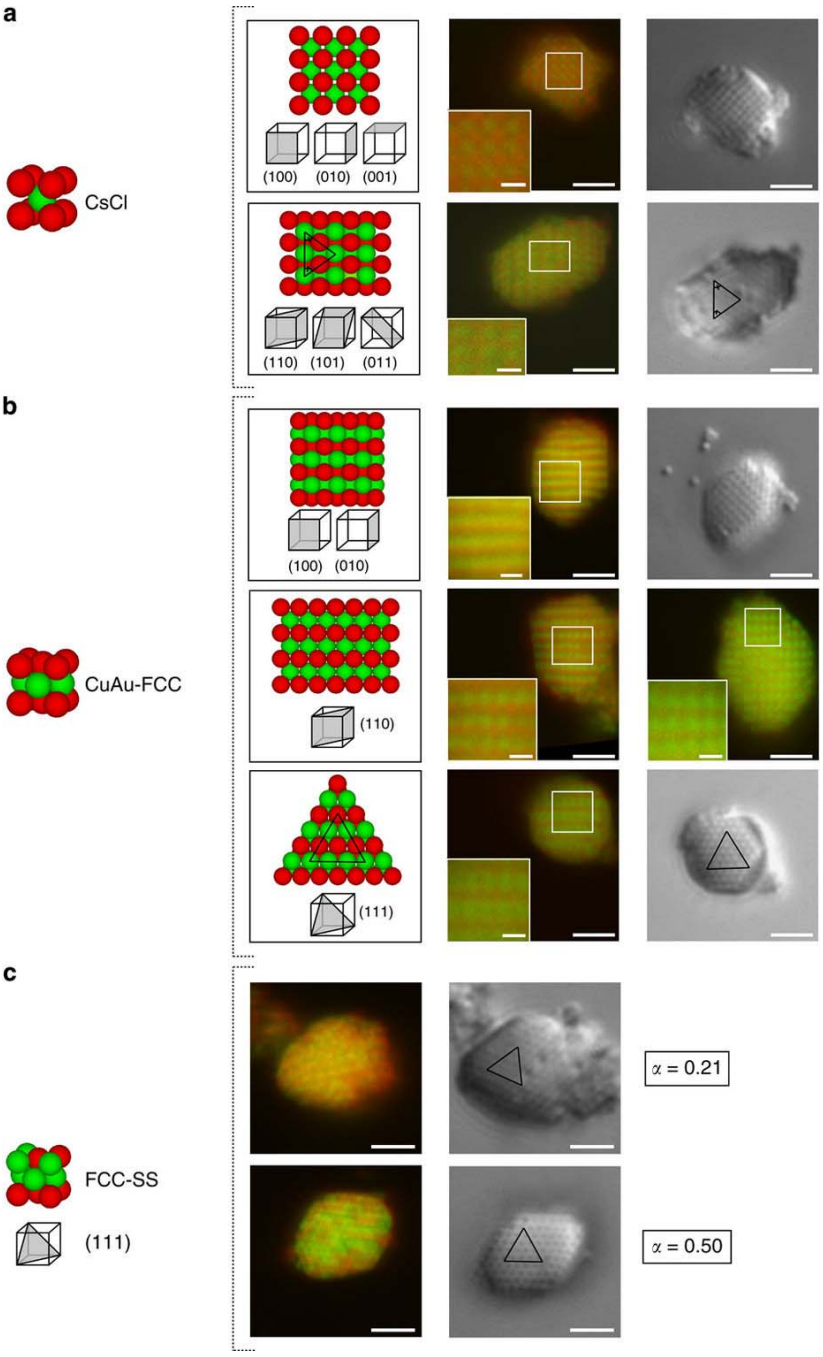

Figure 2.2: Adapted from Ref. (49). Sample crystallites observed in experiment. CsCl (A), CuAu-fcc (B) and fcc-SS (C) are shown. Scale bars indicate 2μm or 0.5 μm in insets.

The action of a displacive (or diffusionless), transformation was deduced based on two principal observations. First, a small number of the crystallites were found to exhibit two distinct domains (CsCl and CuAu-I) separated by a sharp, coherent interface, similar to the Martensite-Austenite interfaces observed in steels (101) as shown below in Figure 2.3. A more indirect suggestion for the presence of a diffusionless transformation between CsCl and CuAu-I came from the observation that the vast majority of CuAu-I crystallites found in experiment were perfectly ordered, in contrast to previous modeling studies performed by Scarlett et al. (99) which indicate homogeneous nucleation and growth of close-packed phases in this system give rise to numerous compositional ordering defects.

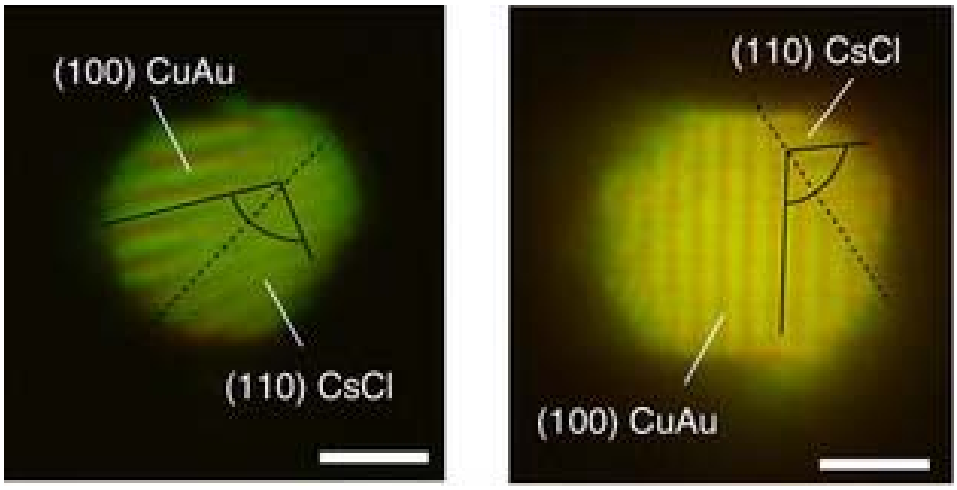

Figure 2.3: Adapted from Ref. (49). Two examples of DNA functionalized colloidal particle crystallites exhibiting the CsCl and CuAu superlattices simultaneously. Scale bars indicate a length of 2μm.

In the following, we first employ direct Langevin dynamics (LD) simulations and establish the feasibility of the transformation, although we find that the resulting close-packed configurations are always more structurally diverse than the uniform CuAu-I observed in experiment. We understand the source of this diversity by performing a vibrational mode analysis which enables us to identify all possible energetically degenerate transformation pathways that lead to different final (close-packed) configurations. Finally, we consider the role of hydrodynamic correlations on the effective multi-particle diffusivity of the system configuration along different transformation pathways, and find that the anomalous configurations seen in experiment are precisely those that are strongly favored by hydrodynamics. Furthermore, we conjecture that such hydrodynamic selection may play a role in other colloidal systems displaying collective particle dynamics, such as hard-sphere and attractive glasses.

2.2 Langevin Dynamics Simulations

We first performed LD simulations that consist of numerical integration of the Langevin equation for a system of particles that are subject to interparticle forces as well as forces due to the presence of an implicit solvent, i.e.,

$$m\ddot{\mathbf{r}} = \mathbf{F}(\mathbf{r}) - \gamma\dot{\mathbf{r}} + \sqrt{2\gamma m k_B T}\,\mathbf{R}(t) \tag{2.1}$$

where **r** is the time-dependent vector of particle positions, $\mathbf{F}(\mathbf{r})$ represents the interparticle forces, γ is the damping, or friction, coefficient ($\gamma = k_B T / D$), and $\mathbf{R}(t)$ is a random Brownian force modeled as a delta-correlated Gaussian process with zero mean

so that $\langle \mathbf{R}(t) \rangle = 0$ and $\langle \mathbf{R}(t)\mathbf{R}(t') \rangle = \delta(t-t')$. All LD simulations were performed using the LAMMPS software package (102), with particle interactions calculated using the coarse-grained inter-particle pair potential model developed by Rogers *et al*. (82) which is described in detail in Section 1.2.

The LD simulations of CsCl→CuAu-I transformation were initialized by placing spherical CsCl crystallites in a colloidal fluid of randomly-placed particles corresponding to a particle volume fraction of 0.3. An example of the initial system configuration is shown below in Figure 2.4. The colloidal fluid particles were used to stabilize the crystallite against dissolution. In each run, the simulation was first allowed to reach equilibrium using interparticle interactions that favored the CsCl phase $\left(E_{AB} = 6.0k_BT,\ E_{AA} = 0\right)$ once equilibrium was reached the interactions were adjusted to favor CuAu-I and the simulation continued until the transformation (if present) was completed. The final crystallite structure was analyzed using LAMMPS' common neighbor analysis (CNA).

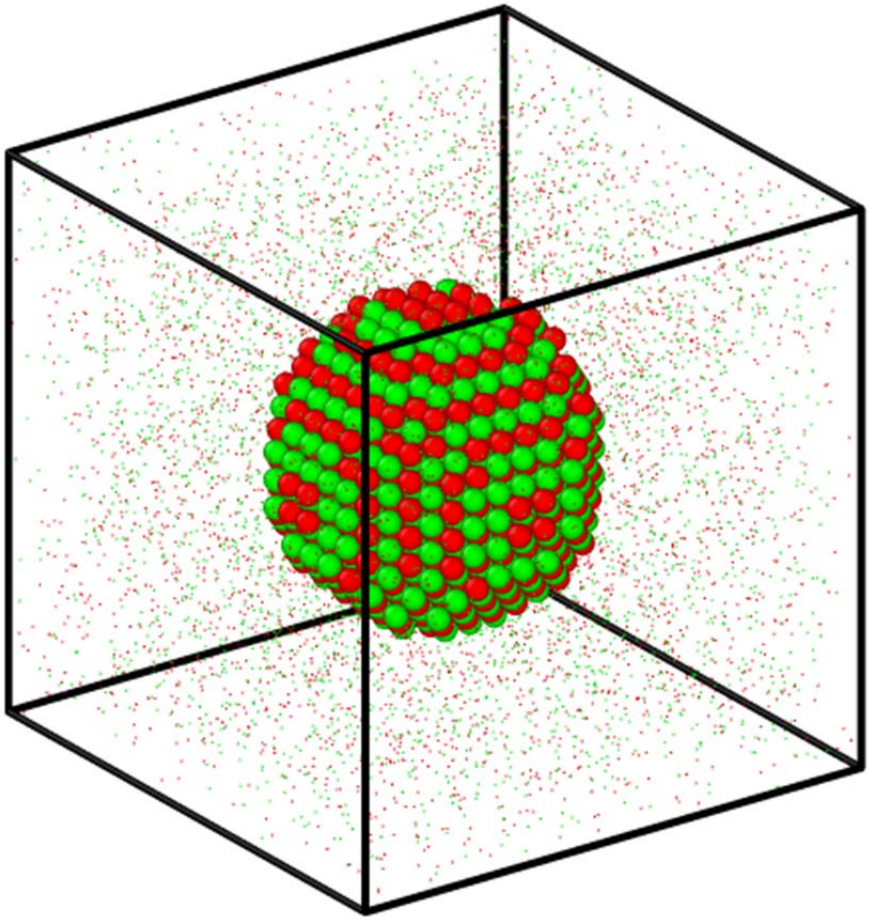

Figure 2.4: Example initial system configuration for a 1500 particle seed. Non-crystal particles are shown at 10% actual size for visualization purposes.

Several parameters were varied in order to probe their possible influence on the transformation. These include the crystallite size (220-8000 particles), the implicit fluid viscosity (0-5% of water), AB interaction strength $(4k_BT \le E_{AB} \le 6k_BT)$, and (AA/BB) interaction strength $(1.0k_BT \le E_{AA} \le 2.5k_BT)$. Examples of transformed crystallite configurations are shown in Figure 2.5. In general, the transformed close-packed

crystallites are of rhcp character with randomly distributed hcp and fcc planes although most of the samples are biased towards hcp, a feature we return to later. A few transformed crystals are highly defected and appear to exhibit multiple transformations nucleated along different directions leading to “locked” configurations. For example, the configuration in Figure 2.5B shows a situation in which locking leads to a metastable, untransformed CsCl interior section (blue) that is surrounded by rhcp regions (red/green). In Figure 2.5C, locking leads to regions of unidentifiable structure (grey) that presumably consist of partial cp and bcc character. Generally, only larger crystals run at higher viscosities tended to exhibit such configurations, which may be explained by the fact that damping reduces the correlation length scale of nucleated transformations, allowing multiple independent transformations to nucleate simultaneously.

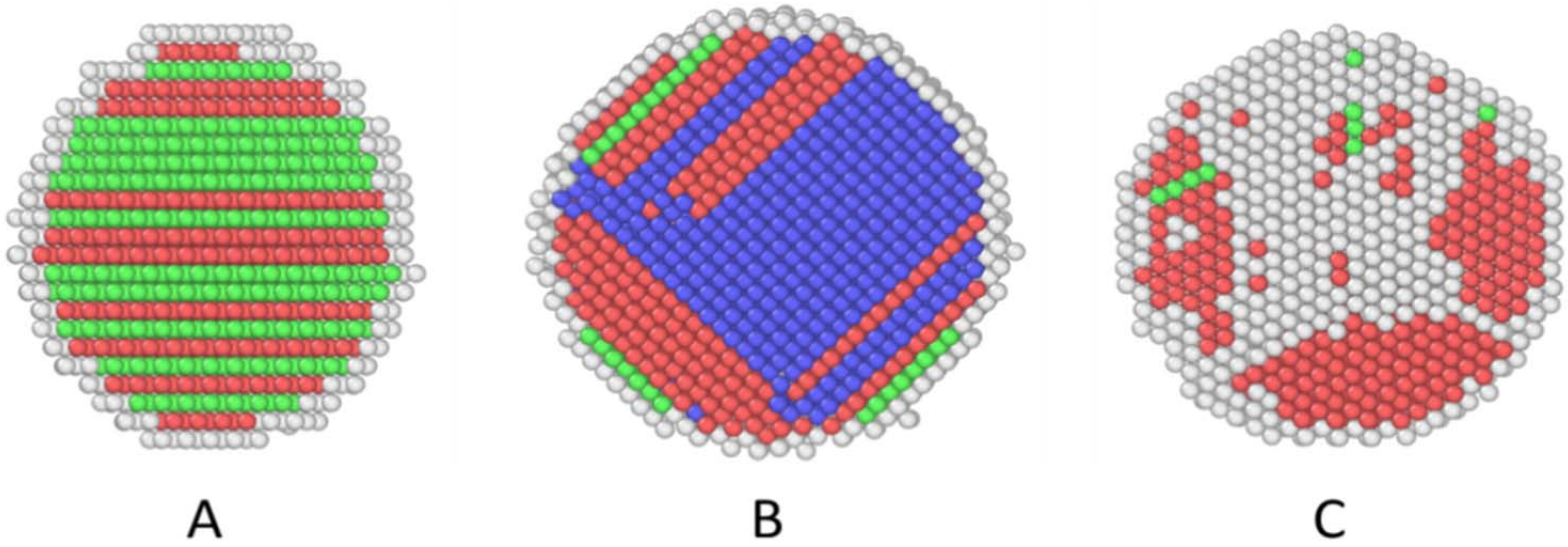

Figure 2.5: Examples of transformed crystallite configurations observed in LD simulations (see text). Crystallites initially contain 5000 (case A) or 8000 (cases B and C) particles, which are colored according to their structure as determined by CNA. Red particles are identified as hcp, green particles as fcc, blue particles as bcc and grey as “unidentified”.

In order to better quantify the differences between the rhcp structures produced by Langevin simulations of the bcc-cp transformations and those seen in experiment, an order parameter, χ, was defined as the ratio of close-packed planes in the crystallite which possess fcc structure to those that possess hcp structure. A χ value of 1 would then indicate an equal distribution of fcc- and hcp-like crystallite planes. A total of 4 parameters were investigated: the crystallite size (220-8000 particles), the implicit fluid viscosity (0-500% of water), unlike interaction strength $(4k_BT \le E_{AB} \le 6k_BT)$, and like interaction strength $(1.0k_BT \le E_{AA} \le 2.5k_BT)$. The range of viscosity was sufficient to span the transition from overdamped to inertial dynamics. A system of interacting particles in a viscous medium is considered overdamped when (103)

$$\frac{\gamma}{2\sqrt{mk}} > 1 \tag{2.2}$$

where *m* is the particle mass, *k* is the effective spring constant experienced by a particle in the system and γ is the drag coefficient. The drag coefficient is given by

$$\gamma = 3\pi\mu d_p \tag{2.3}$$

where μ is the fluid medium viscosity and d_p is the particle diameter. In the present calculations, the value of gamma for a system at 5% the viscosity of water, μ_w, with 400nm-diameter particles is 3.36×10^{-9} kg/s. Furthermore, the value of mk when the interaction potential is at maximum strength (highest spring constant) is 4.24×10^{-8} kg^2/s^2, which gives $\gamma / 2\sqrt{mk}$ ~1.5. In other words, the maximum viscosity considered here is sufficient to achieve fully overdamped conditions. Shown in Figs. 2.6-2.9 are

representative samples of transformed crystallites obtained at various combinations of the above parameters

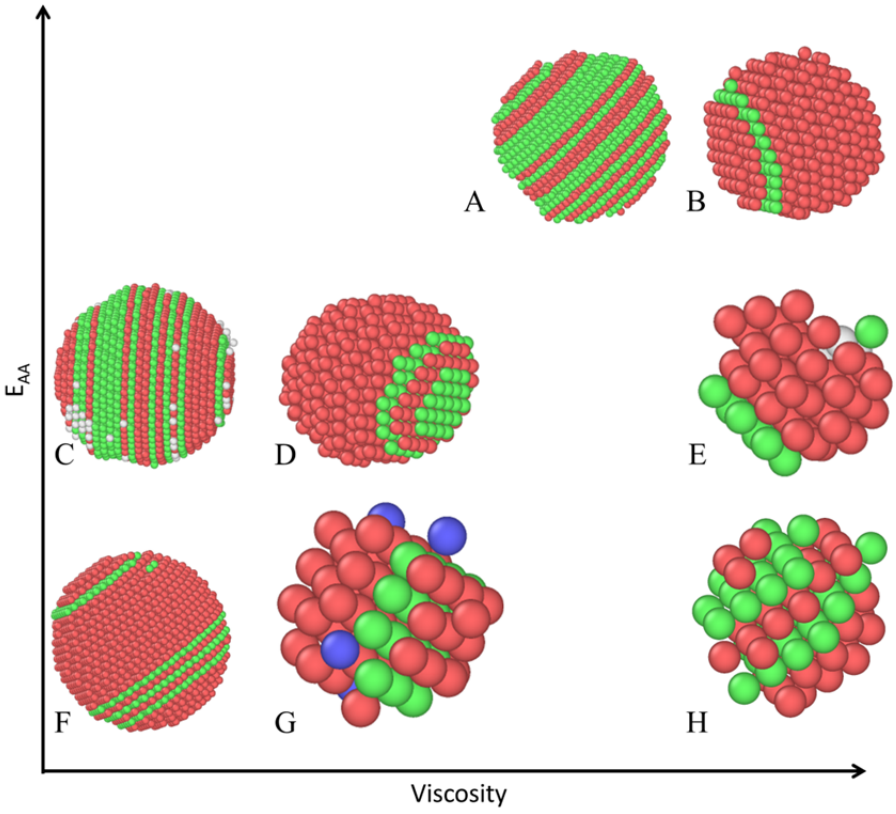

Figure 2.6: Sample crystallites for like particle interaction strength (E_{AA}) versus system viscosity. System parameters are (all energies in units of k_BT): A) $E_{AB}=6$, $E_{AA}=2.5$, $\mu=0.01\mu_w$, $n=5000$; B) $E_{AB}=6$, $E_{AA}=2.5$, $\mu=0.05\mu_w$, $n=5000$; C) $E_{AB}=6$, $E_{AA}=1.5$, $\mu=0$, $n=8000$; D) $E_{AB}=5$, $E_{AA}=1.5$, $\mu=0.005\mu_w$, $n=1500$; E) $E_{AB}=4$, $E_{AA}=1.5$, $\mu=0.05\mu_w$, $n=220$; F) $E_{AB}=4$, $E_{AA}=1$, $\mu=0$, $n=8000$; G) $E_{AB}=6$, $E_{AA}=1$, $\mu=0.005\mu_w$, $n=220$; H) $E_{AB}=5$, $E_{AA}=1$, $\mu=0.05\mu_w$, $n=220$.

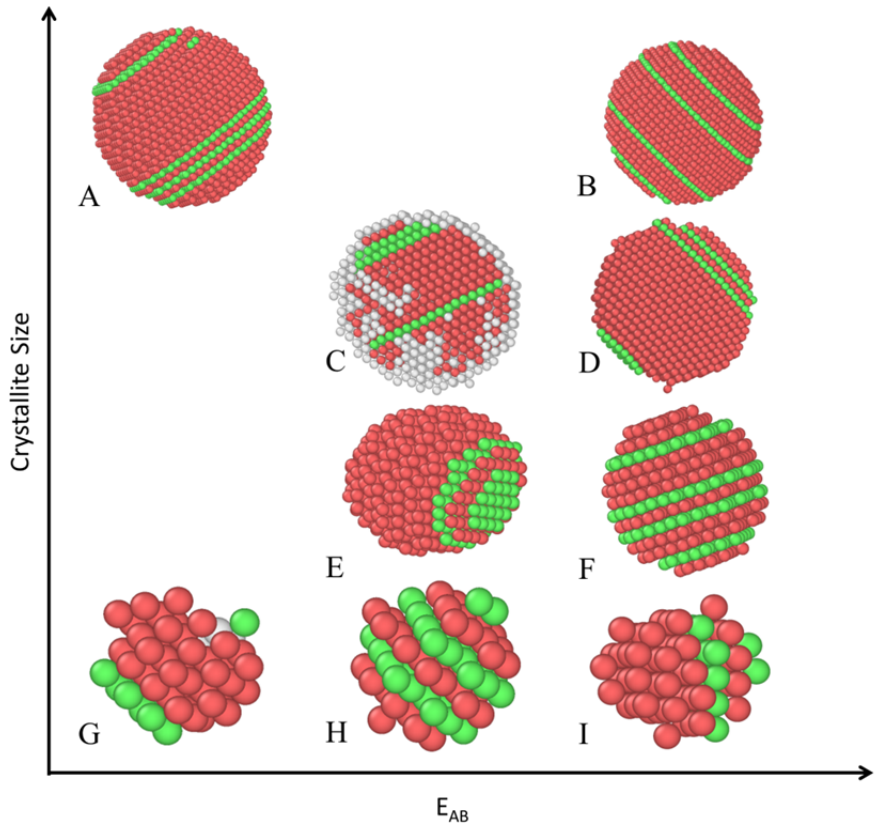

Figure 2.7: Sample crystallites for crystallite size versus unlike particle interaction strength. System parameters are (all energies in units of k_BT): A) $E_{AB}=4$, $E_{AA}=1$, $\mu=0$, $n=8000$; B) $E_{AB}=6$, $E_{AA}=2.5$, $\mu=0$, $n=8000$; C) $E_{AB}=5$, $E_{AA}=1.5$, $\mu=0.005\mu_w$, $n=5000$; D) $E_{AB}=6$, $E_{AA}=1.5$, $\mu=0, n=5000$; E) $E_{AB}=5$, $E_{AA}=1.5$, $\mu=0.005\mu_w, n=1500$; F) $E_{AB}=6$, $E_{AA}=1.5$, $\mu=0.005\mu_w$, $n=1500$; G) $E_{AB}=4$, $E_{AA}=1.5$, $\mu=0.05\mu_w$, $n=220$; H) $E_{AB}=5$, $E_{AA}=2.5$, $\mu=0, n=220$; I) $E_{AB}=6$, $E_{AA}=1.5$, $\mu=0.05\mu_w$, $n=220$.

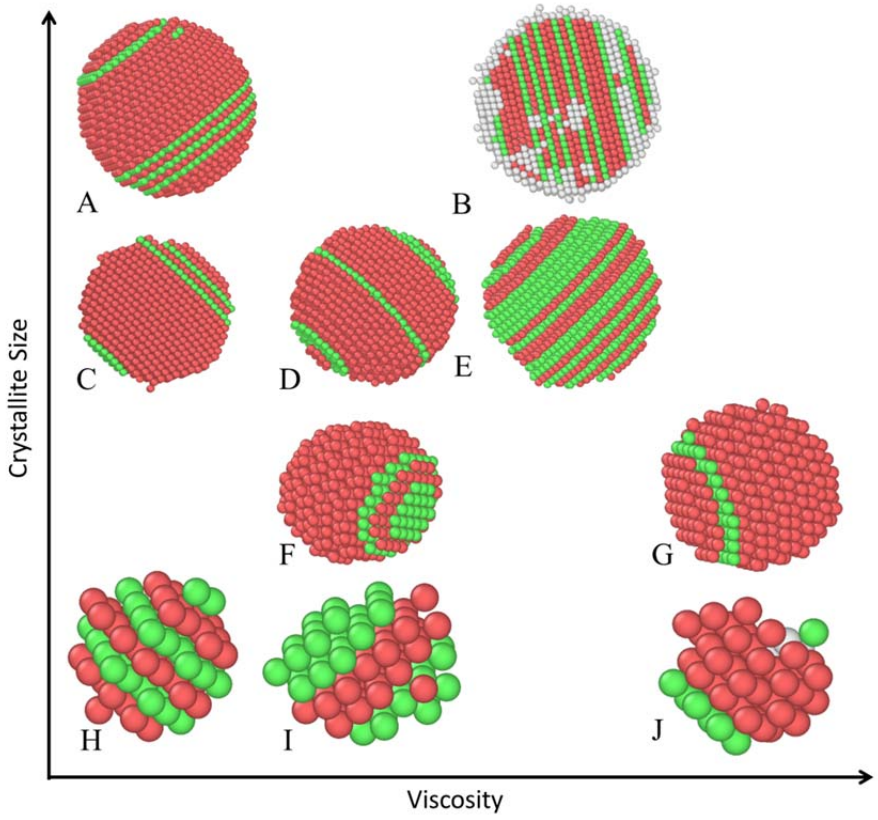

Figure 2.8: Sample crystallites for crystallite size versus viscosity. System parameters are (all energies in units of k_BT): A) $E_{AB}=4$, $E_{AA}=1$, $\mu=0$, $n=8000$; B) $E_{AB}=6$, $E_{AA}=1.5$, $\mu=0.01\mu_w$, $n=8000$; C) $E_{AB}=6$, $E_{AA}=1.5$, $\mu=0$, $n=5000$; D) $E_{AB}=6$, $E_{AA}=1.5$, $\mu=0.005\mu_w$, $n=5000$; E) $E_{AB}=6$, $E_{AA}=2.5$, $\mu=0.01\mu_w$, $n=5000$; F) $E_{AB}=5$, $E_{AA}=1.5$, $\mu=0.005\mu_w$, $n=1500$; G) $E_{AB}=6$, $E_{AA}=2.5$, $\mu=0.05\mu_w$, $n=1500$; H) $E_{AB}=5$, $E_{AA}=2.5$, $\mu=0$, $n=220$; I) $E_{AB}=6$, $E_{AA}=1$, $\mu=0.005\mu_w$, $n=220$; J) $E_{AB}=4$, $E_{AA}=1.5$, $\mu=0.05\mu_w$, $n=220$.

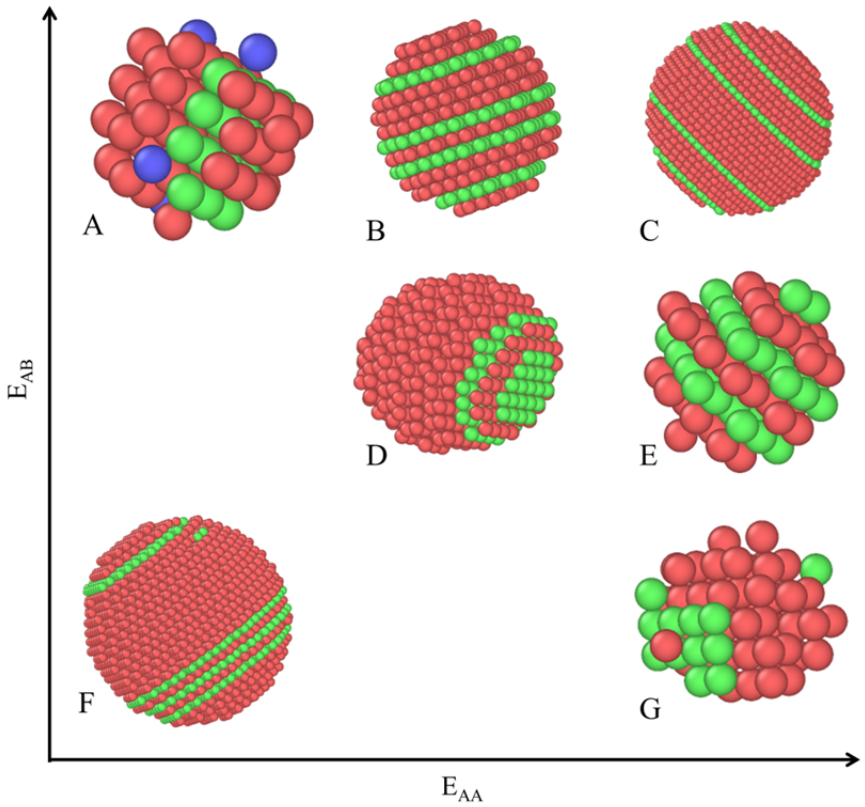

Figure 2.9: Sample crystallites for unlike particle interaction strength versus like particle interaction strength. System parameters are (all energies in units of k_BT): A) $E_{AB}=6$, $E_{AA}=1$, $\mu=0.005\mu_w$, $n=220$; B) $E_{AB}=6$, $E_{AA}=1.5$, $\mu=0.005\mu_w$, $n=1500$; C) $E_{AB}=6$, $E_{AA}=2.5$, $\mu=0$, $n=8000$; D) $E_{AB}=5$, $E_{AA}=1.5$, $\mu=0.005\mu_w$, $n=1500$; E) $E_{AB}=5$, $E_{AA}=2.5$, $\mu=0$, $n=220$; F) $E_{AB}=4$, $E_{AA}=1$, $\mu=0$, $n=8000$ $n=220$; G) $E_{AB}=4$, $E_{AA}=2.5$, $\mu=0$, $n=220$.

In Figure 2.10, plots of the fcc-hcp order parameter, χ, are shown as a function of each of the 4 parameters. The plots exhibit large amounts of scatter and do not reveal any significant correlation between the order parameter and any of the 4 simulation parameters, although some weak effects may be apparent such as higher hcp fraction with increasing viscosity. Most importantly, there does not appear to be any parameter combination that leads to very high values of χ (pure fcc), as observed in the experimental crystals.

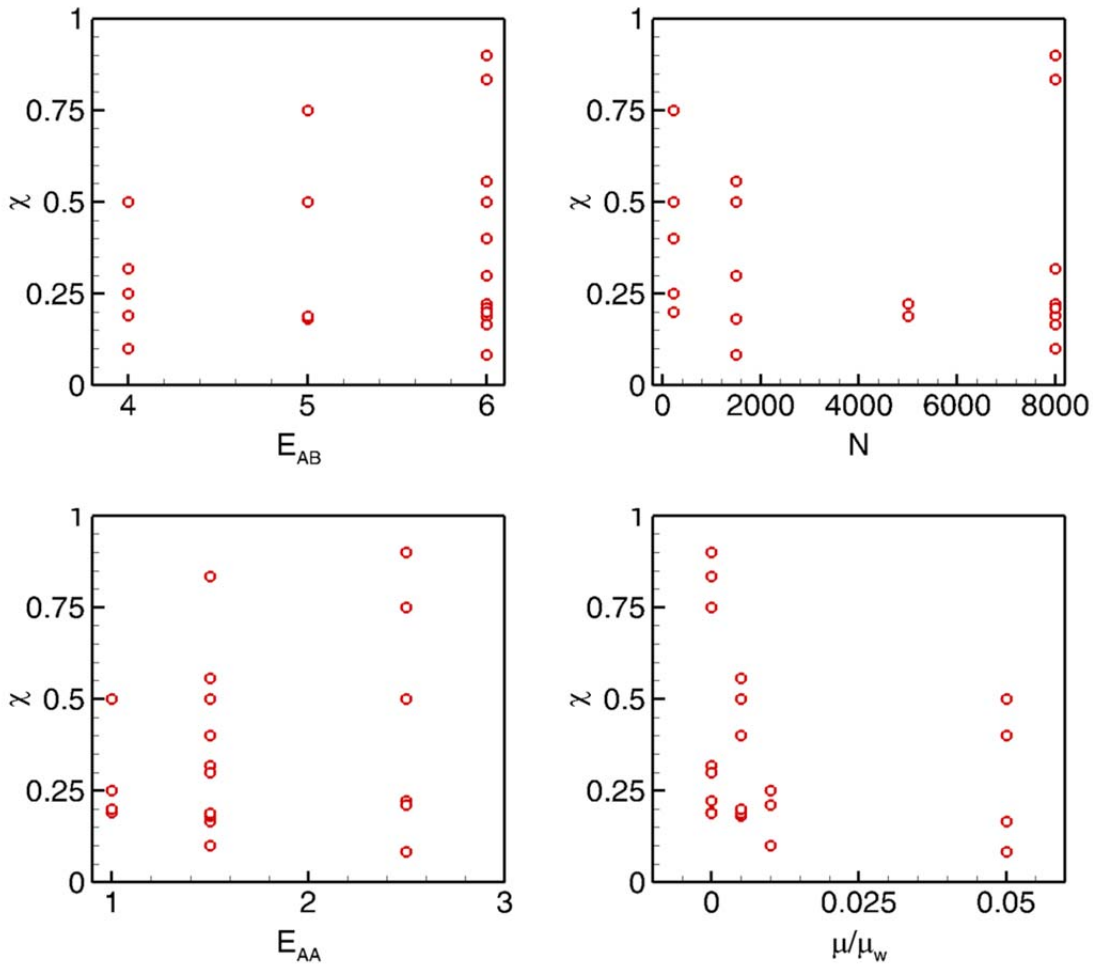

Figure 2.10: fcc-to-hcp order parameter, χ , as a function of each of the 4 simulation parameters: Unlike particle type binding strength E_{AB}, like particle interaction strength E_{AA} fluid viscosity relative to water μ / μ_w and crystallite size N .

2.3 Vibrational Mode Analysis

The persistent discrepancy between simulated and experimental transformed crystallites suggests the presence of multiple accessible transformation pathways. In this section we seek to generate a basis for identifying all possible pathways and thus a mechanism that would explain the discrepancy. We first performed a vibrational mode analysis of the CsCl (and CuAu-I) superlattice DLPAs. Note that the experimental system is overdamped and the vibrational frequencies we describe below do not imply oscillatory behavior (104). Vibrational mode analysis was carried out within the harmonic approximation (HA) about the perfect CsCl (or CuAu-I) configuration, i.e.,

$$U = U_0 + \frac{1}{2}\mathbf{u}^T \cdot \mathbf{H} \cdot \mathbf{u} + O(\mathbf{u}^3), \tag{2.4}$$

where U_0 is the reference potential energy, $\mathbf{u} \in \mathbb{R}^{3N}$ is the perturbation vector away from the reference, $\mathbf{r_0}$, and $\mathbf{H} \in \mathbb{R}^{3N \times 3N}$ is the dynamical (or Hessian) matrix given by

$$H_{\alpha,\beta}^{i,j} = \left(\frac{\partial^2 U}{\partial r_i^\alpha \partial_j^\beta} \right)_{\mathbf{r_0}}, \tag{2.5}$$

where *i* and *j* are atom indices, and α and β are direction indices. The 3*N* eigenvalues, $\{\lambda_i\}$, and corresponding eigenvectors, $\left\{\mathbf{v} \in \mathbb{R}^{3N}\right\}$, of **H** are related to the vibrational frequencies and vibrational mode vectors, respectively, of the system about the reference configuration.

Shown in Figure 2.11 are the vibrational density-of-states (V-DOS) for spherical CsCl and CuAu-I crystallites containing 1000 particles with interactions $E_{AB} = 6\ k_B T$ and

$E_{AA}, E_{BB} = 0.6 k_B T$ (CsCl) or $E_{AA}, E_{BB} = 6\ k_B T$ (CuAu-I). Both V-DOS distributions exhibit broad ranges of vibrational mode frequencies but CsCl also shows a large number of zero-frequency modes, $\{\mathbf{v}_0\}$: while there are 6 such eigenvectors for CuAu-I, there are 77 for the CsCl crystallite. The 6 zero-frequency CuAu-I modes correspond to 3 crystallite translation modes and 3 rotation modes that are always present for any finite particle assembly. The additional CsCl zero frequency, or "floppy", modes, suggest that displacive transformations in colloidal DLPAs may have a different character than in atomic systems where (in general) no zero-frequency modes exist due to the long-range and multi-body nature of atomic interactions. Nonetheless, transformations in both types of materials are expected to proceed along the lowest energy pathways – for the particular colloidal DPLAs we consider here these pathways are apparently barrier-less.

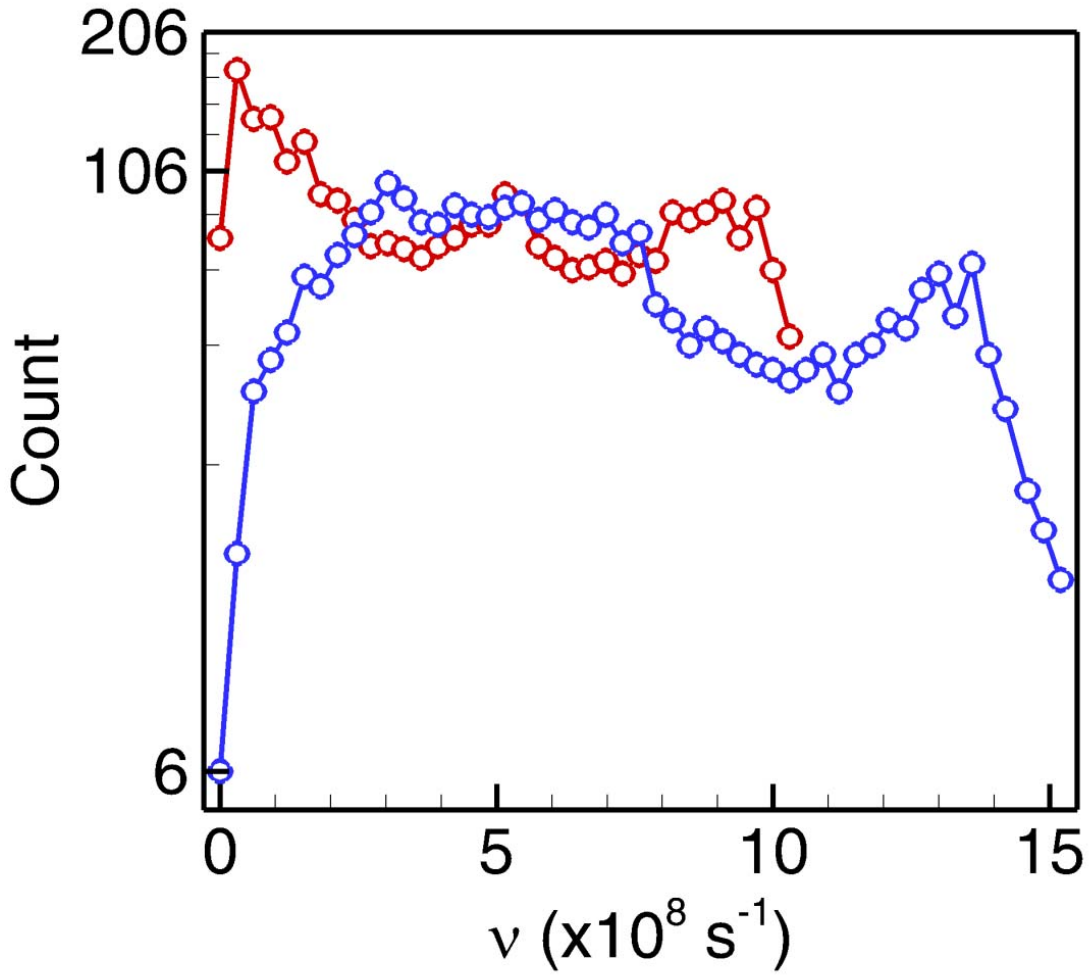

Figure 2.11: Vibrational density-of-states for spherical crystallites. Frequencies correspond to the square-root of the Hessian eigenvalues. Blue – 1000-particle CuAu-I crystallite $\left(E_{AA}=E_{AB}=6k_BT\right)$; red – 1000-particle CsCl crystallite $\left(E_{AB}=6k_BT, E_{AA}=0\right)$

.

The existence of a flat energy sub-space (corresponding to the *kernel* or null-space of the Hessian matrix) that is spanned by a large number of zero-frequency eigenvectors makes difficult the identification of specific bcc→cp transformation

pathways. Shown in Figure 2.12A is a randomly selected floppy eigenvector for the CsCl superlattice (200-particle cubic crystallite). This eigenvector is an arbitrary linear combination of all zero-frequency modes and does not provide insight into the different transformation pathways. In ref. (105), Holmes-Cerfon *et al*. elegantly demonstrated how the floppy sub-space can be geometrically analyzed and mapped for small clusters in the limit of infinitely short-ranged interactions, i.e., the so-called “sticky sphere” limit. Here, we take a different approach that relaxes the sticky-sphere and small cluster limits imposed in ref. (105). Starting with a perfect CsCl crystallite, we sequentially assign harmonic springs to random particles that tether them to their equilibrium positions. Each time an additional particle is tethered, the vibrational mode spectrum is recalculated. The effect of incremental tethering is to systematically reduce the dimensionality of the floppy sub-space by eliminating zero-frequency modes (increasing rigidity). The process is repeated until a single zero-frequency mode remains. If the number of floppy modes reaches zero before reaching one, the tethers are removed and the process reinitiated. Shown in Figure 2.12B is an example single floppy mode that remains following the tethering procedure. Unlike the random vector shown in Figure 2.12A, this mode denotes a well-defined in-plane motion of particles lying in a single (110) plane of the CsCl superlattice.

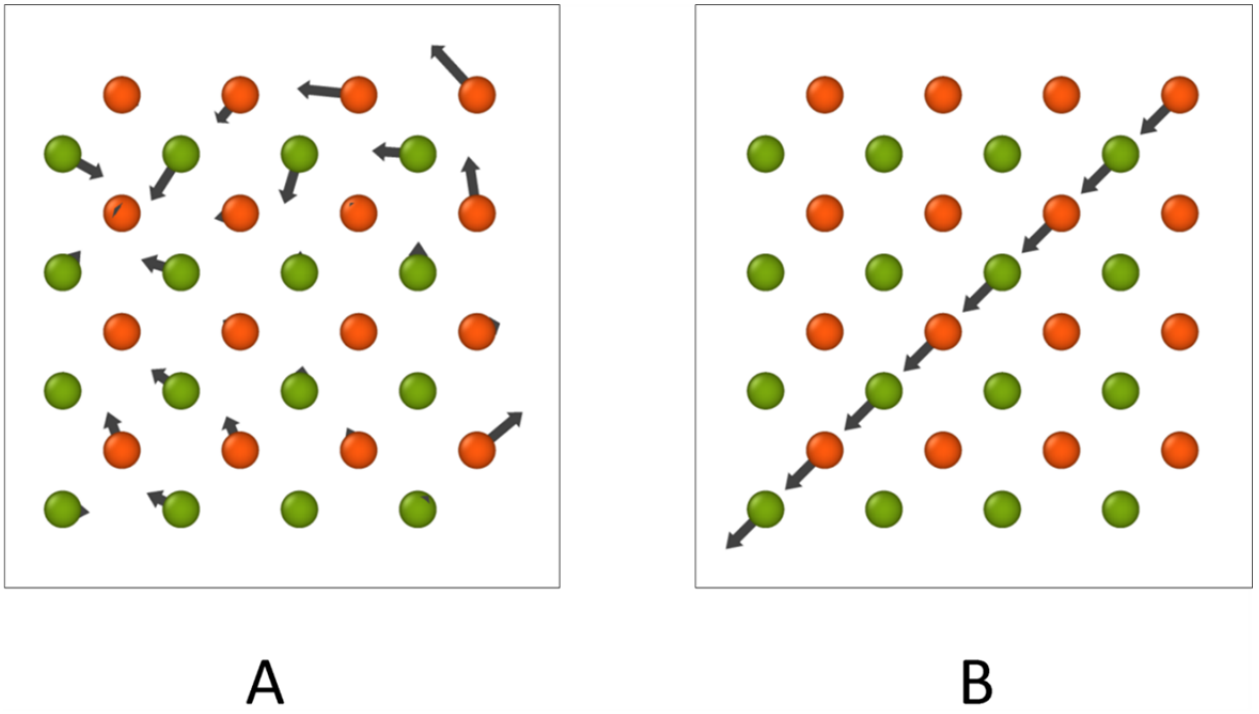

Figure 2.12: (A) (100) plan view of an arbitrary zero-frequency eigenvector for the ideal CsCl configuration of a cubic crystallite with 200 particles. (B) (100) plan view of the center-plane “modelet” eigenvector showing center-plane particles moving along the (110) direction while all other particles are stationary.

We refer to the eigenvector depicted in Figure 2.12B as a “modelet”; a crystal-wide displacive transformation, $\mathbf{v}_T$, that evolves the crystallite from CsCl to CuAu-I (or something else) is comprised of a linear combination of *P* modelets so that

$$\mathbf{v}_T = \sum_{i=1}^{P} \alpha_i \mathbf{m}_i \tag{2.6}$$

where *P* is the number of (110) planes in the crystallite and α_i are coefficients. Note that modelets corresponding to different particle planes along (110) are mutually orthogonal ($\mathbf{m}_i \cdot \mathbf{m}_j = 0$) because each initially only involves motion within a single plane. Similar arguments may be made for the symmetrically equivalent sets of transformations along the $(1\,\bar{1}\,0)$, (101), $(10\,\bar{1})$, (011) and $(01\,\bar{1})$ planes. Although the orthogonality property does not generally hold between modelets with different orientations, e.g., $\mathbf{m}_i^{(110)} \cdot \mathbf{m}_j^{(101)} \neq 0$, they are still always (pairwise) linearly independent. Consequently, the modelet basis identified by our tethering procedure is expected to at most span a linear vector space with dimension *P*. In fact, the precise value is *P*-4 because some modelet combinations are not linearly independent. Importantly, *P*-4 is found to always be exactly equal to the total number of zero eigenvalues in a CsCl crystallite, demonstrating that the modelet basis can be used to systematically define all possible barrier-less bcc-cp transformations.

In order to demonstrate why there are precisely *P*-4 independent modelets we must first express a basis for the zero-frequency subspace in terms of the *P* pair-wise

linearly independent modelets However, we show here that this "naïve" *P*-dimensional basis includes several linear dependencies so that

$$q = P - d \ , \tag{2.7}$$

where *d* is the number of linear dependencies.

Next, we consider the modelet combinations that produce rigid body translation (RBT) and rotation (RBR). Along each of the six (110) orientations ((110), (1-10), (101), etc…), a rigid body translation can be generated by combining modelets such that all p_i atomic planes are translated by equal amounts. However, only three such rigid body translations are linearly independent implying three linear dependencies. We can also test RBR for similar dependencies. RBRs can be constructed as the sum of shear modes along orthogonal pairs of (110) planes, e.g., for (110) and (1-10)

$$\mathbf{v}_{RBR}^{[001]} = \mathbf{v}_{Shear}^{(110)} - \mathbf{v}_{Shear}^{(1\bar{1}0)} . \tag{2.8}$$

Since there exist only three such combinations, no additional linear dependencies arise from RBR.

It is tempting to assume that *d*=3. However, one additional linear dependence is present in the naïve modelet basis. Consider a two-dimensional tetragonal deformation mode, $\mathbf{v}_D^{[100],[010]}$, defined as consisting of an expansion in the [100] direction and a contraction in the [010] direction. This tetragonal deformation can be constructed by the addition of two shear (zero-frequency) modes, i.e.,

$$\mathbf{v}_D^{[100],[010]} = \mathbf{v}_{Shear}^{(110)} + \mathbf{v}_{Shear}^{(1\bar{1}0)} , \tag{2.9}$$

where the shear modes are constructed by sums over modelets, e.g.,

$$\mathbf{v}_{Shear}^{(110)} = \sum_{i=1}^{p_{(110)}} i\mathbf{m}_i^{(110)} \,. \tag{2.10}$$

Now we consider the well-known three-dimensional tetragonal Bain transformation mode, which can be expressed as a sum over three distinct two-dimensional distortions:

$$\mathbf{v}_{Bain}^{[100]} = a\mathbf{v}_D^{[100],[010]} + (1-a)\,\mathbf{v}_D^{[100],[001]} + \left(a - \frac{1}{2}\right)\mathbf{v}_D^{[010],[001]} \,. \tag{2.11}$$

Here, the single unconstrained parameter, *a*, directly implies that it is possible to construct identical Bain modes with different linear combinations of deformation modes and indicates the presence of one additional degree of linear dependence among the *P* modelets so that *d*=4 and

$$q = P - 4 \,. \tag{2.12}$$

The completeness of the *P*-4 dimensional basis was verified by calculating the number of zero-frequency modes for three differently-sized spherical CsCl crystallites containing *P*=51, 63, and 75 (110) planes, respectively. For the three crystallites, the number of floppy modes was 47, 59, and 71 (*P*-4).

We tracked several transformation pathways constructed with different modelet combinations. The crystal-wide combinations were constructed using eq. (2.6) after normalizing the modelets so that the planar velocity has a value of unity. The coefficients, α_i, were then selected so that a constant relative velocity between adjacent planes was imposed. For example, if the first coefficient is unity, the second is given by either +c or –c, where c>1, thereby creating a relative velocity between the first two

modelets/particle planes. The next modelet/particle plane is then displaced at a velocity of either +c or –c relative to the second modelet, and so on until every plane has been assigned a velocity. According to this scheme, the total number of crystal-wide modes along a given (110) orientation is 2^{p_i-1} where p_i is the number of crystal planes along orientation *i*.

Mode tracking was performed by evolving the particle positions numerically along a given transformation vector, i.e.

$$\mathbf{r}_{new} = \mathbf{r}_{old} + \delta \mathbf{v}_T(\mathbf{r}), \tag{2.13}$$

where δ represents the step size. An important aspect of this procedure is the fact that as the crystallite configuration transforms, each modelet evolves from a single plane vector to a more complex one that involves the translation of additional, out-of-plane particles. As a result, the zero-frequency sub-space changes and a new Hessian kernel, **K**, must be computed repeatedly about the current configuration, $\mathbf{r}_{new}$. One consequence of this evolution is that the orthogonality properties of modelets computed at the ideal CsCl configuration do not necessarily hold as the crystal is deformed (although linear independence is maintained). Attempting to reconstruct a new modelet basis each time a new kernel is obtained, e.g., with the tethering procedure described above, would be prohibitively difficult. Instead, we use the least squares approximation to find the mode contained within the new kernel that is closest to the current mode, such that

$$\mathbf{v}_T^{new} = \mathbf{K}\left[\left(\mathbf{K}^T\mathbf{K}\right)^{-1}\left(\mathbf{K}^T\mathbf{v}_T^{old}\right)\right] \tag{2.14}$$

where $\left(\mathbf{K}^T\mathbf{K}\right)^{-1}\left(\mathbf{K}^T\mathbf{v}_T^{old}\right)$ produces a vector containing the magnitude of the contribution to the new mode from each component of the kernel. The process in eqs. (2.13)-(2.14) is repeated until the dimensionality of the kernel decreases to a value of six, at which point the system is no longer floppy and a boundary of the zero-frequency sub-space is located. At this location, a local (downhill) energy minimization is performed using the Fast Inertial Relaxation Mechanism (FIRE) method (106) and the configuration tested for evidence of a transformation.

We considered three specific combinations of modelets, the first two being constructed along a single [110] direction: (1) the magnitudes of all modelets are shifted by +c relative to their neighbors, and (2) the shift alternates between +c and –c across the entire crystallite. The first case corresponds to a uniform shear along the (110) direction (Figure 2.13A), while the second case corresponds to a “zig-zag” displacement field along (110) as shown in Figure 2.13B. The third case (Figure 2.13C) is the well-known Bain strain (107)..

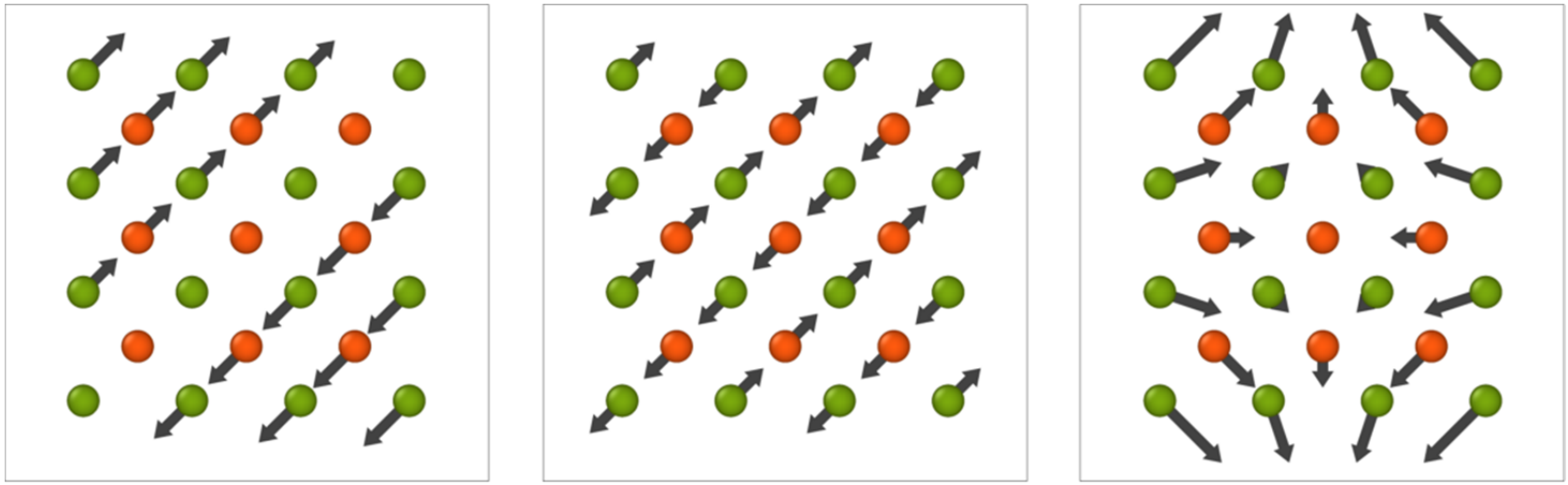

Figure 2.13: (100) plan views of different transformation modes constructed using linear combinations of modelets. (A) Shear, (B) “zig-zag”, and (C) Bain.

Evolving the (initially CsCl) crystallite along each of these modes we find that once the flat energy sub-space is reached (i.e., once the energy begins to change), further evolution along the mode vector corresponds to a negative energy change. Local energy minimizations initiated at these locations then rapidly lead to the final cp states. Shown below in Figure 2.14 are sample configuration states along the transformation pathway of a CsCl crystallite into hcp via the so-called zig-zag mode. The top row shows the transformation looking down along the z-axis onto a (100) surface, while the lower row shows the same configurations looking down the y-axis onto the (010) surface. The zig-zag transformation initially proceeds via the motion of atomic planes along (110) as shown in A and D. The configuration shown in B and E represent the point at which the zero-frequency eigenvector disappears and corresponds to a location at the boundary of the flat energy manifold. A downhill energy minimization performed at this location produces the configuration shown in C and F.

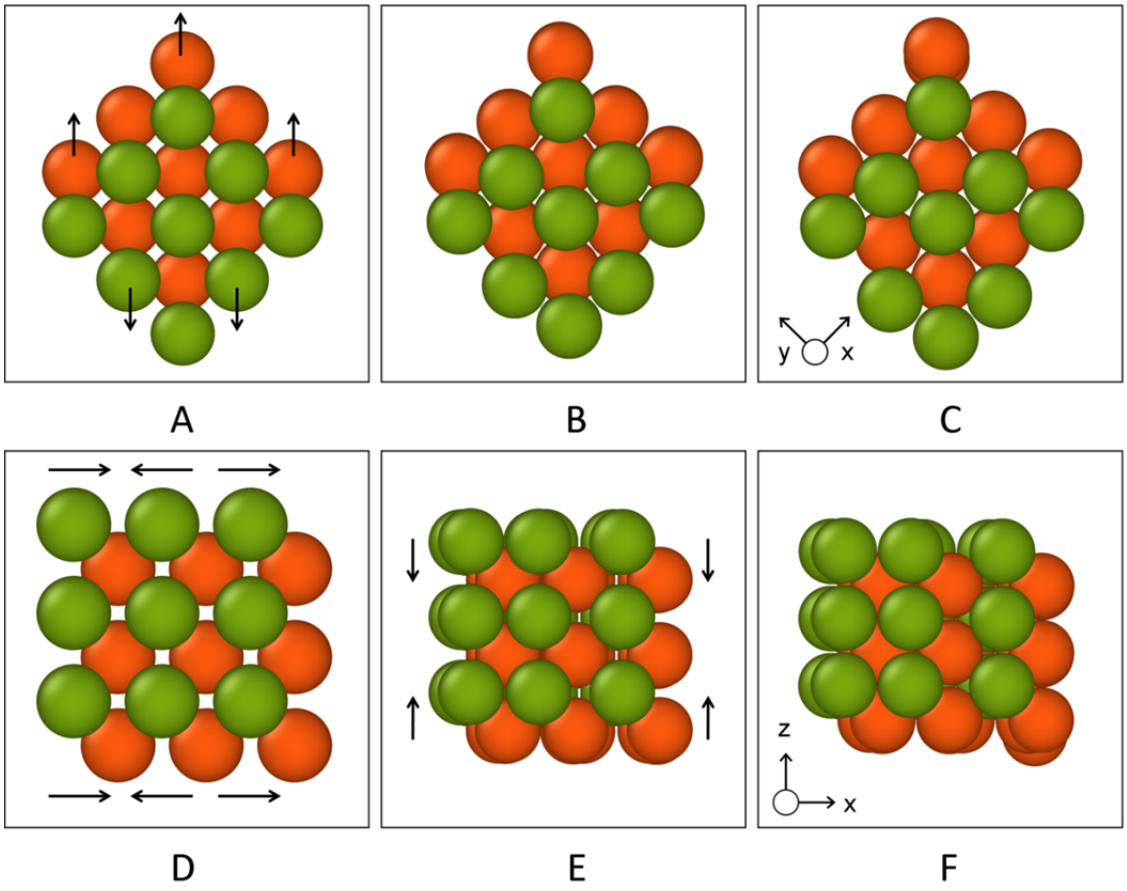

Figure 2.14: Visualization of the various stages experienced by a transforming crystallite during the zig-zag mode transformation. Arrows indicate the deformations occurring during each stage of the transformation. A and D are the (100) (z) and (010) (y) views of the original CsCl lattice. B and E show the (100) and (010) views of the partially transformed system, after the zero frequency evolution process has been completed. C and F show the (100) and (010) views of the system once the energy minimization has terminated.

For the uniform shear and Bain strain cases, the resulting crystallite is CuAu-I (Figure 2.15A), while the zig-zag displacement leads to an ordered hcp superlattice as shown in Figure 2.15B. Additional calculations using combinations of shear and zig-zag displacements lead to rhcp (Figure 2.15C). Note that the CuAu-I, hcp, and rhcp superlattices are all compositionally (and energetically) equivalent, i.e., in each case every particle is subject to 8 unlike (AB) contacts and 4 like (AA/BB) contacts.

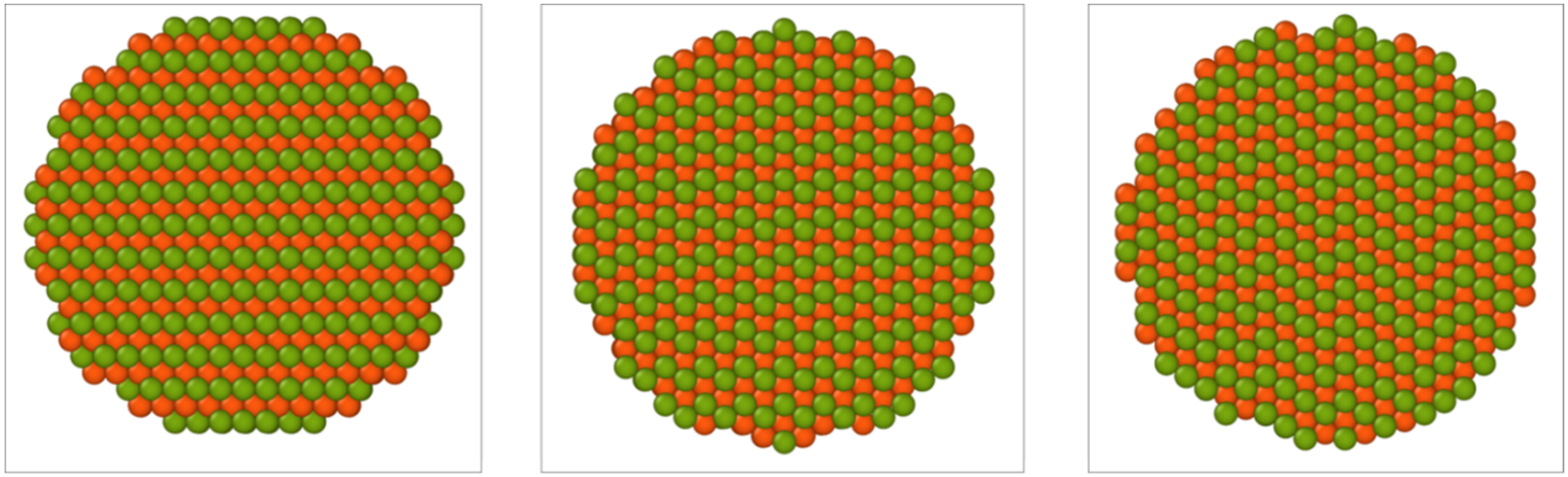

Figure 2.15: Compositionally ordered CuAu-I (A), hcp (B) and rhcp (C) superlattice structures. Each cp structure exhibits 8 like contacts and 4 unlike contacts for every particle.

It is worth emphasizing that, by contrast, downhill energy minimizations initiated at edges of the zero-frequency manifold found using arbitrary zero-frequency eigenvectors (e.g., Figure 2.12A) never lead to bcc-cp transformations: only properly constructed eigenvectors find paths to a cp configuration. This observation suggests that the topology of the zero-frequency manifold is of "hub-and-spoke" type with the ideal CsCl configuration at the center of the "hub". While most excursions from CsCl quickly become blocked at the hub boundary, narrow openings (the spokes) lead to the various cp states. Taken together, these results provide a simple entropic explanation for why LD simulations initiated at the ideal CsCl configuration generally lead to rhcp transformed crystals rather than fcc CuAu-I (or pure hcp): there are far more modelet combinations that correspond to rhcp $\left(6(2^{P-1}-4)\right)$ than either pure hcp (6) or fcc (9). In the case of the 1000-particle crystallite considered previously, this amounts to 36,867 rhcp states, each with its own microscopically distinct transformation pathway.

It is possible that subtle details of the zero-frequency manifold structure, such as funnels, or differences in the "spoke" hyper-geometries could cause a bias in the end-state distribution and thus explain the CuAu-I selection observed experimentally. However, as mentioned earlier, the only apparent bias appears to favor transformation to hcp rather than fcc. The observed hcp bias can be qualitatively explained by considering the difference in the way the fcc- and hcp-producing transformations occur on a local scale: while relative motion between two adjacent (110) planes immediately

leads to a locally hcp configuration, creation of an fcc plane requires the concerted motion of three adjacent planes in the parent CsCl crystal.

2.4 Hydrodynamic Correlation and Anisotropic Diffusion

The preceding vibrational mode analysis appears to fully explain the structural diversity observed in the LD simulations – but provides no clues regarding the discrepancy with respect to the experimental structures. Here, we consider the possibility of biasing induced by hydrodynamic correlations between the particles. Hydrodynamic forces are known to be important in driven (non-equilibrium) systems, e.g., when a shearing force is applied externally (108), but they are usually neglected when considering particle assembly in quiescent solvents, particularly when only the final configuration (rather than the kinetics) is of interest.

We introduce hydrodynamic correlations in incompressible fluids by modifying eq. (2.1) to include the hydrodynamic force, $\mathbf{F_H}$, which is given by

$$\mathbf{F}_{H,i} = \gamma \sum_{\substack{j=1 \\ j \neq i}}^{n} \frac{\mathbf{D}_{ij}}{k_B T} \cdot \mathbf{F}_j(\mathbf{r}), \tag{2.15}$$

where $\mathbf{D}$ is the mobility tensor. The hydrodynamic force on particle *i* represents viscous drag created by flow induced via the motion of other particles. In the full Stokesian dynamics approach (109), a further modification of eq. (2.1) is required in which the single-particle random Brownian force, $\mathbf{R}(t)$, is replaced by a new random force, $\mathbf{R}'(t)$, that accounts for correlations between Brownian forces acting upon different particles so that $\left\langle \mathbf{R}'_i(t)\mathbf{R}'_j(t) \right\rangle = 2\mathbf{D}_{ij}dt$. However, this modification greatly increases the

computational cost of the simulation and is not directly relevant for the present analysis. Instead, we consider the non-Brownian (fluctuation-free) limit and further assume that the particles are inertia-less for simplicity. We also consider particle rotation so that the coupled force and torque balance equations are given by

$$\begin{bmatrix} \dot{\mathbf{r}} \\ \dot{\boldsymbol{\theta}} \end{bmatrix} = \frac{1}{k_B T} \begin{bmatrix} \mathbf{D}_{tt} & \mathbf{D}_{tr} \\ \mathbf{D}_{rt} & \mathbf{D}_{rr} \end{bmatrix} \cdot \begin{bmatrix} \mathbf{F} \\ \boldsymbol{\tau} \end{bmatrix}, \tag{2.16}$$

where the mobility tensor is comprised of 4 sub-tensors, $\mathbf{D}_{\alpha\beta}$, that describe the influence of hydrodynamic correlations on particle translation ("t") and rotation ("r"). The terms of the mobility matrix, $\mathbf{D}$, are approximated using asymptotic expansions as described in ref. (110). In particular, we employ expansions up to 12th order in the center-to-center distance between pairs of particles. The single particle contributions to the mobility matrix are

$$\mathbf{D}_{ii}^{tt} = k_B T \left(4\pi\eta A_0^S \right)^{-1} \mathbf{I}, \tag{2.17}$$

$$\mathbf{D}_{ii}^{rr} = k_B T \left(8\pi\eta A_1^T \right)^{-1} \mathbf{I}, \tag{2.18}$$

where $\mathbf{D}_{ii}^{tt}$ is the translational mobility for a single sphere, $\mathbf{D}_{ii}^{rr}$ is the rotational mobility for a single sphere, and A_0^S and A_1^T are scattering coefficients. The two-particle interaction terms are given by

$$D_{ij,\alpha\beta}^{tt}\left(\mathbf{R}_{ij}\right) = k_B T \left(\alpha_{ij}^{tt}\left(R\right) \hat{R}_{ij,\alpha} \hat{R}_{ij,\beta} + \beta_{ij}^{tt}\left(R_{ij}\right)\left(\delta_{\alpha\beta} - \hat{R}_{ij,\alpha}\hat{R}_{ij,\beta}\right)\right) \tag{2.19}$$

$$D_{ij,\alpha\beta}^{tr}\left(\mathbf{R}_{ij}\right) = k_B T \left(\beta_{ij}^{tr}\left(R_{ij}\right) \boldsymbol{\varepsilon} \hat{R}_{ij,\gamma} \right) \tag{2.20}$$

$$D^{rr}_{ij,\alpha\beta}\left(\mathbf{R}_{ij}\right)=k_BT\left(\alpha^{rr}_{ij}\left(R_{ij}\right)\hat{R}_{ij,\alpha}\hat{R}_{ij,\beta}+\beta^{rr}_{ij}\left(R_{ij}\right)\left(\delta_{\alpha\beta}-\hat{R}_{ij,\alpha}\hat{R}_{ij,\beta}\right)\right)\ , \tag{2.21}$$

where $\mathbf{R}_{ij}$ is the center-to-center distance vector between a pair of particles $\mathbf{R}_{ij}=\mathbf{r}_i-\mathbf{r}_j$, $\hat{R}_{ij,\alpha}$ is a normalized directional component of $\mathbf{R}_{ij}$ such that $\hat{R}_{ij,\alpha}=R_{ij,\alpha}/R_{ij}$, $\boldsymbol{\varepsilon}$ is the completely antisymmetric Levi-Civita tensor. Values for the various α and β parameters are given by

$$\begin{aligned}4\pi\eta\alpha^{tt}_{ij}\left(R_{ij}\right)&=\frac{1}{2}R_{ij}^{-1}-\frac{1}{15}S_iR_{ij}^{-3}+A^S_{1,i}A^S_{1,j}R_{ij}^{-7}\\&+\left[A^S_{1,1}\left(-6B^S_{1,j}+\frac{18}{5}A^S_{2,j}+\frac{3}{5}\hat{B}^P_{2,j}\right)-\frac{2}{5}S_1A^S_{1,i}A^S_{1,j}\right]R_{ij}^{-9}\\&+\left\{A^S_{1,i}\left(-\frac{48}{5}B^S_{2,j}+\frac{40}{7}A^S_{3,j}+\frac{12}{7}B^P_{3,j}\right)-B^S_{1,i}\left(-5B^S_{1,j}+\frac{68}{5}A^S_{2,j}+\frac{3}{5}\hat{B}^P_{2,j}\right)\right.\\&+\mathrm{A}^S_{2,i}\left(\frac{21}{5}A^S_{2,j}+\frac{6}{5}B^P_{2,j}\right)-\frac{4}{5}S_i\left[A^S_{1,i}\left(-B^S_{1,\mathrm{j}}+\frac{3}{2}A^S_{2,j}\right)\right.\\&\left.\left.+\left(-\frac{3}{2}B^S_{1,i}+\frac{9}{10}A^S_{2,i}+\frac{3}{20}\hat{B}^P_{2,i}\right)A^S_{1,j}\right]+\frac{1}{450}S_iS_jA^S_{1,i}A^S_{1,j}\right\}R_{ij}^{-11}+\left[i\leftrightarrow j\right]+O\left(R_{ij}^{-13}\right)\end{aligned} \tag{2.22}$$

$$\begin{aligned}4\pi\eta\beta^{tt}_{ij}(R_{ij})&=\frac{1}{4}R_{ij}^{-1}+\frac{1}{30}S_iR_{ij}^{-3}-\left\{B^S_{1,i}\left(-\frac{1}{6}B^S_{1,j}+\frac{4}{15}A^S_{2,j}+\frac{2}{3}A^T_{2,j}+\frac{1}{10}\hat{B}^P_{2,j}\right)\right.\\&+A^S_{2,i}\left(\frac{61}{480}A^S_{2,j}+\frac{5}{12}A^T_{2,j}+\frac{3}{40}\hat{B}^P_{2,j}\right)-\frac{2}{3}A^T_{2,\mathrm{i}}A^T_{2,j}-\frac{1}{15}\mathrm{S}_i\\&\mathrm{x}\left(-\mathrm{B}^S_{1,i}+\frac{4}{5}\mathrm{A}^S_{2,i}+2\,\mathrm{A}^T_{2,i}+\frac{3}{10}\hat{\mathrm{B}}^P_{2,i}\right)\mathrm{A}^S_{1,j}\\&\left.+\frac{1}{150}\mathrm{S}_i\mathrm{S}_j\mathrm{A}^S_{1,i}\mathrm{A}^S_{1,\mathrm{j}}\right\}\mathrm{R}_{ij}^{-11}+\left[i\leftrightarrow j\right]+O\left(R_{ij}^{-13}\right)\end{aligned} \tag{2.23}$$

$$
\begin{aligned}
8\pi\eta\beta_{ij}^{tr}\left(R_{ij}\right) = &-R^{-2} - A_{1,i}^{S}\left(-B_{1,j}^{S} + \frac{4}{5}A + 2A_{2,j}^{T} + \frac{3}{10}\hat{B}_{2,j}^{P} - S_i A_{1,j}^{S}\right)R^{-10} \\
&- \{A_{1,i}^{S}\left(-\frac{39}{10}B_{2,j}^{S} + \frac{15}{7}A_{3,j}^{S} + \frac{5}{2}A_{3,j}^{T} + \frac{8}{7}B_{3,j}^{P}\right) - B_{1,i}^{S}\left(-\frac{8}{3}B_{1,j}^{S} + \frac{5}{2}A_{2,j}^{S}\right) \\
&+ A_{2,i}^{S}\left(-\frac{8}{3}B_{1,j}^{S} + \frac{61}{24}A_{2,j}^{S} + \frac{25}{6}A_{2,j}^{T} + \frac{3}{4}\hat{B}_{2,j}^{P}\right) \\
&- A_{2,\mathrm{i}}^{T}\left(-\frac{4}{3}B_{1,j}^{S} + \frac{5}{6}A_{2,j}^{S} - \frac{8}{3}A_{2,j}^{T}\right) - \frac{8}{15}S_i[A_{1,i}^{S}\left(-B_{1,j}^{S} + \frac{3}{2}A_{2,j}^{S}\right) \\
&+ \left(-B_{1,i}^{S} + A_{2,i}^{S} - \frac{1}{2}A_{2,i}^{T}\right)A_{1,j}^{S}]\}R^{-12} + O\left(R^{-14}\right)
\end{aligned}
\tag{2.24}
$$

$$
8\pi\eta\alpha_{ij}^{rr}\left(R_{ij}\right) = \frac{1}{2}R_{ij}^{-3} + 6A_{2,i}^{T}A_{2,j}^{T}R_{ij}^{-13} + 30A_{2,i}^{T}A_{3,j}^{T}R_{ij}^{-15} + [\mathrm{i} \leftrightarrow j] + O\left(R_{ij}^{-17}\right) \tag{S.25}
$$

$$
\begin{aligned}
8\pi\eta\beta_{ij}^{rr}\left(R_{ij}\right) = &-\frac{1}{4}R_{ij}^{-3} + \frac{3}{4}A_{1,i}^{S}A_{1,j}^{S}R_{ij}^{-9} + A_{1,i}^{S}\left(-4B_{1,j}^{S} + 4A_{2,j}^{S} - 2A_{2,j}^{T}\right)R_{ij}^{-11} \\
&+ [\mathrm{i} \leftrightarrow j] + O\left(R_{ij}^{-13}\right)
\end{aligned}
\tag{2.26}
$$

where the notation $[\mathrm{i} \leftrightarrow j]$ indicates that the preceding terms should be repeated once with all *i* and *j* indices swapped. Once again, the various *A* and *B* terms are scattering coefficients and are provided in ref. (111).In order to compute the overall mobility along a particular mode direction, particles arranged in a perfect CsCl crystallite with lattice parameter determined by the minimum potential energy are assigned velocities that correspond to that mode and eq. (2.6) is used to calculate the corresponding particle drag forces, $\mathbf{F}_i$. For the time being, we assume that particles are freely rotating, i.e., that they are torque-free and $\boldsymbol{\tau} = \mathbf{0}$. The applied velocity vector is always scaled so that the total drag force exerted by an equivalent system of isolated

particles is the same for all modes. A normalized overall effective mobility along a given velocity vector is then defined as

$$D = \frac{\left\|\dot{\mathbf{r}}\right\|_2 / \left\|\mathbf{F}\right\|_2}{\left\|\dot{\mathbf{r}}\right\|_2 / \left\|\mathbf{F_0}\right\|_2} = \frac{\left\|\mathbf{F_0}\right\|_2}{\left\|\mathbf{F}\right\|_2}, \tag{2.27}$$

where $\mathbf{F_0}$ is the vector of drag forces in the system of isolated particles.

Shown in Figure 2.15A are the scaled mobilities as a function of (spherical) crystallite size for the three different transformation pathways, computed at the initial CsCl configuration. These results correspond to a particle diameter, d_p, of 400 nm, and particle center-to-center distance, d_c, of 420 nm as dictated by the location of the energy minimum of the potential function ($E_{AB} = 6.0\,k_B T$), i.e., $d_r \equiv d_p / d_c \sim 0.95$. Overall, the fcc-producing shear mode is found to have the highest effective mobility, while the hcp-producing zig-zag mode has the lowest. Random zero-frequency modes that do not correspond to transformation pathways exhibit mobilities that lie in between the simple shear and zig-zag limits (Figure 2.15A inset). Interestingly, the zig-zag mode and most of the random eigenvectors, are hindered by hydrodynamic correlation (scaled mobilities below unity), while the shear and Bain modes are enhanced because of 'slip-streaming'. The mobility anisotropy increases with increasing crystallite size – extrapolating the results in Figure 2.16A to the crystallite sizes in the experiment, >1000 particles, suggests a ratio of diffusive mobilities of order 50 and greater. Although we have insufficient statistical evidence to unambiguously support this prediction experimentally, we have anecdotally found that the few large CuAu-I crystallites do not contain any stacking faults.

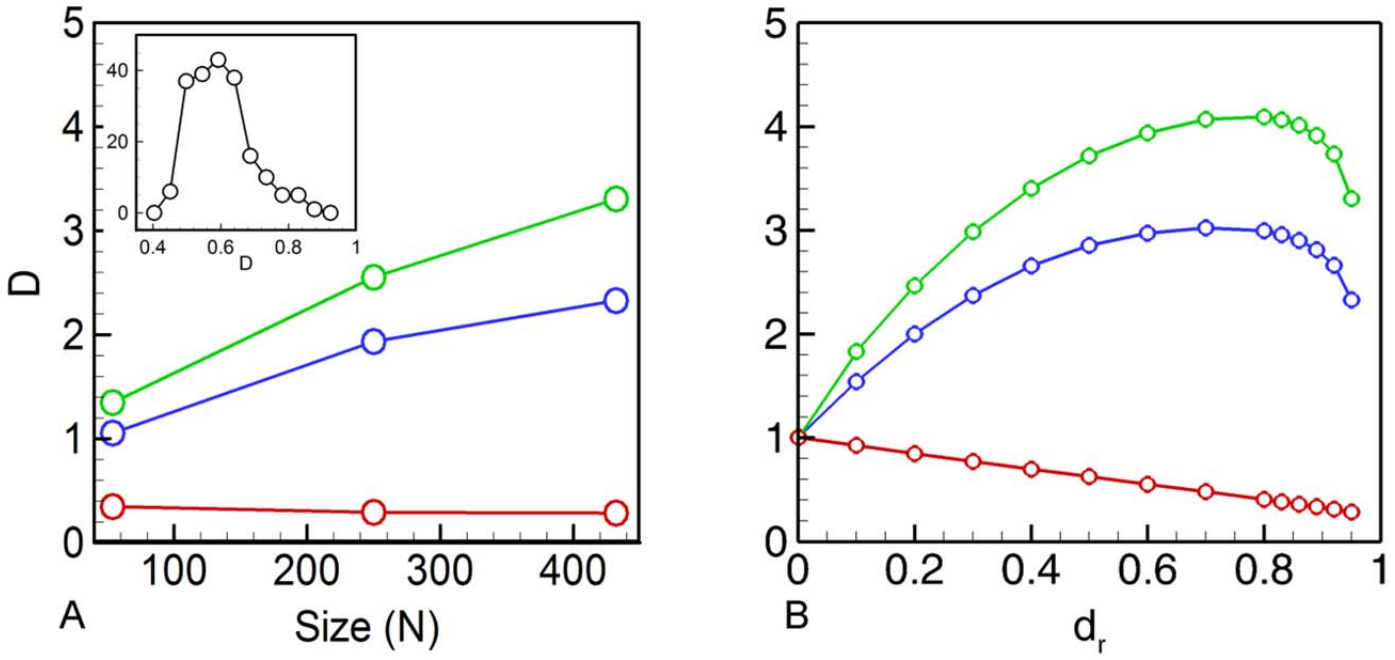

Figure 2.16: (A) Scaled mobility of zero-frequency eigenmodes as a function of spherical CsCl crystallite size for shear – green, Bain – blue, and zig-zag – red. Scaled mobilities are reported relative to mobilities for isolated particles (see eq. 2.7). Inset: Distribution of scaled mobilities for 100 randomly selected zero-frequency eigenvectors for the 54-particle crystallite. (B) Scaled mobilities for 432-particle crystallite as a function of particle size relative to separation, $d_r \equiv (d_p / d_c)^{-1}$, for: shear – green, Bain – blue, zig-zag – red.

While hydrodynamic forces clearly influence displacive transformation pathway selection, other non-equilibrium selection mechanisms, such as particle rolling or sliding, may also be operative or even dominant. The impact of assuming freely-rotating, torque-free particles was probed by repeating the mobility calculations for rotationally fixed particles, i.e., $\dot{\boldsymbol{\theta}} = \mathbf{0}$. The comparison between the two cases is shown below in Figure 2.17 and demonstrates that the difference is small and that the overall conclusions are unaffected by particle rotation.

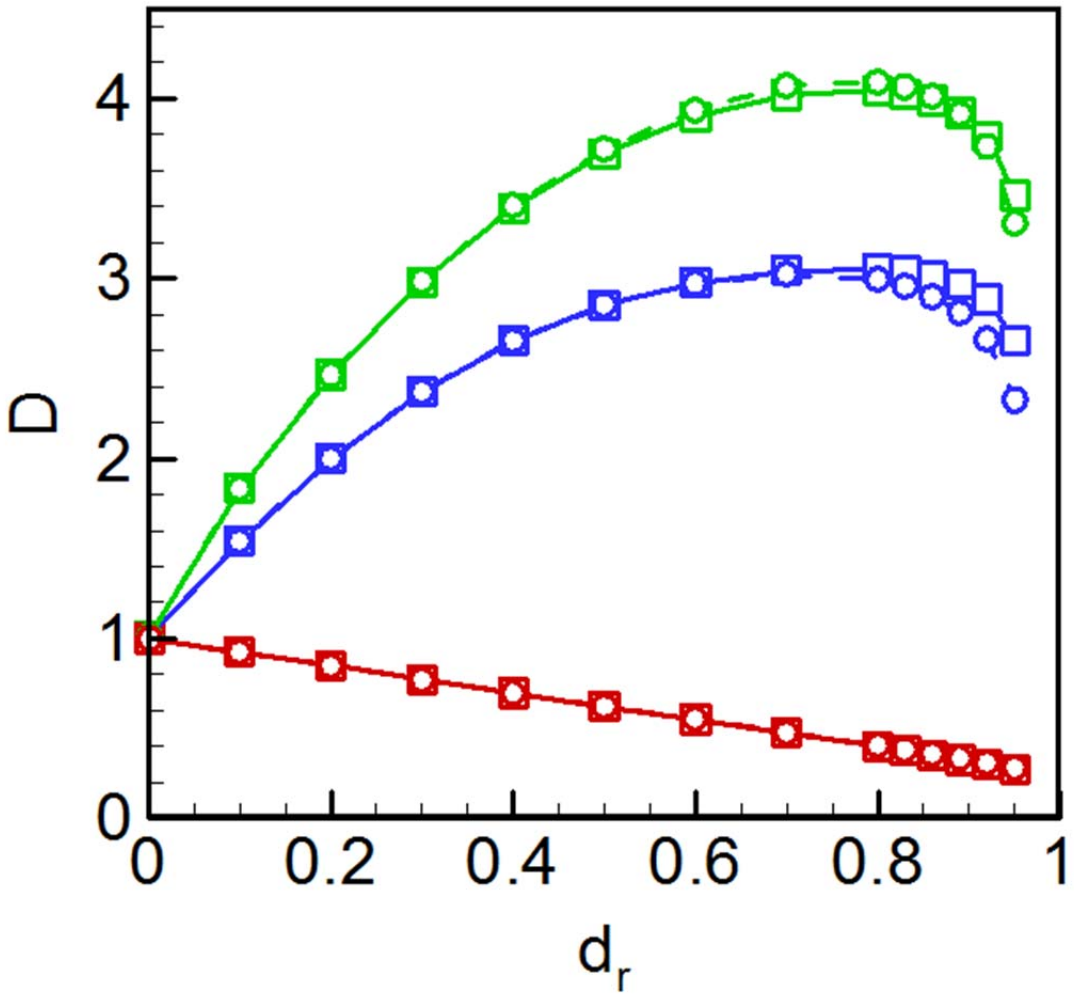

Figure 2.17: Scaled mobilities of zero-frequency eigenmodes for 432-particle CsCl crystallite as a function of particle size relative to separation (d_r) for shear (green), Bain (blue), and zig-zag (red) modes: Squares – rotation-free, circles – torque-free.

This initially surprising discovery regarding the negligible impact of particle rotation on overall mode mobility can be explained by noting that significant particle rotation is not present during the various displacive transformations considered here

because of rotational frustration arising from multiple simultaneous particle-particle interactions. This observation has an important implication, namely that particles must be *sliding* past each other, rather than *rolling* over each other, during the transformations. Equally crucially, the total extent of sliding during each of the different transformation pathways is essentially equal. As a result, any sliding friction due to DNA brush interactions or DNA bridge breakage and/or formation kinetics is not likely to be an important factor in the selection between the different transformation pathways, even if it alters the overall kinetics of the transformation process(es). Taken together, these observations leave hydrodynamic correlations as the likely dominant mechanism for transformation pathway biasing and structure selection.

In summary, our results indicate that hydrodynamic coupling between particles leads to highly anisotropic diffusion within the zero-frequency manifold in configuration space. The biasing mechanism may be interpreted in the context of a reaction network in which the “reactant” (CsCl) can transform into a number of energetically degenerate “products” (the various cp configurations). First, note that the energetic degeneracy of all products implies that, at equilibrium, the product distribution should correspond to the statistical distribution of the mode distribution identified by vibrational analysis – most of the crystallites should be rhcp. In the language of reaction kinetics, this is equivalent to stating that the equilibrium constant (the ratio of the forward and backwards rates) for every pathway is the same but since there are many more reactions that produce various rhcp states, this type of product will dominate.

The anisotropic diffusion created by the hydrodynamic correlations alters the forward and backward rates of each the various pathways, but does so in a way that

preserves the equilibrium constant of each pathway (and therefore the overall equilibrium state). The apparent persistence of the non-equilibrium distribution in the experiments can be reconciled by considering that at some point during the transition from bcc to cp, two new like bonds are formed for every particle, significantly lowering the crystallite energy. In other words, the forward rates are much higher than the backward rates and the equilibrium constants are very large. As a result, the non-equilibrium distribution is expected to persist for very long times – for like interactions of $O(k_BT)$, and crystals containing $O(10^3)$ particles, the transformations are practically irreversible and the anisotropic diffusivity dictates the observed distribution.

2.5 Conclusions

The notion that pre-programmed DNA-grafted particles can be used to deterministically produce equilibrium assemblies is overly simplistic. Several studies have already demonstrated that the processing history to which a population of DNA-grafted particles is subjected can strongly influence the final structure. Most obviously, rapid quenching can trap a system into a high energy, disordered non-crystalline state. However, the influence of kinetic factors also can be much more subtle, acting to select between multiple possible crystalline configurations, either during the crystallization process or, as was shown in our recent experiments, after crystallization via an unexpected displacive transformation.

In this chapter, we uncover yet another source of kinetic influence, namely the solvent in which the particle assembly forms. While externally applied flows have been used previously to influence assembly in a variety of systems, we believe this is the first evidence for an autogenous mechanism in which self-induced hydrodynamic drag forces

in an otherwise quiescent solvent lead to non-equilibrium structure selection. In particular, we provide strong evidence that hydrodynamic correlation between particles establishes a dynamic anisotropy that results in bias towards certain configurations over others during a CsCl→CuAu-I displacive transformation of binary superlattice crystallites. The extent of the anisotropy appears to be closely tied to the ratio of particle size and DNA oligomer length, possibly obfuscating otherwise simple size scaling laws. We emphasize that the outcome of this study is not simply that DLPA processing is complicated: the ability to intentionally direct DLPAs towards non-equilibrium (and useful) configurations greatly increases the versatility of these materials, provided that such effects are well understood.

Finally, while this study was focused on the specific action of anisotropic diffusion during displacive transformations of DNA-linked particle assemblies, we hypothesize that similar effects may occur in a variety of colloidal model systems. The principal defining feature of the system we consider in this chapter is structural transformation involving the cooperative motion of large numbers of colloidal particles, corresponding to the system moving along narrow pathways on flat energy subspaces in configuration space. The same description would apply equally well to glasses and super-cooled fluids of hard-sphere colloids, which display highly cooperative rearrangements termed dynamical heterogeneity (112, 113). Moreover, our CsCl parent crystals are held together by short-range reversible interactions, in insufficient numbers to give rise mechanical rigidity, reminiscent of so-called attractive glass colloidal systems (114). Thus, we hypothesize that hydrodynamic selection/biasing can play a role in multiple systems of considerable current interest, in which the details of microscopic

rearrangements often remain poorly understood and experimental results frequently do not resemble those from matched simulations.

3. EXPLORING ZERO-ENERGY PHASE TRANSFORMATIONS IN ASYMMETRIC BINARY SYSTEMS

3.1 Introduction

As shown in Chapter 2, CsCl crystallites constructed from micron-sized DNA-functionalized colloidal particles are capable of multiple solid-solid phase transformations. This is due to both the short interaction range relative to the particle size and the relatively low bonding coordination between particles in the CsCl superlattice, both of which lead to a non-rigid structure exhibiting a large number of zero-frequency vibrational modes. In principle, this lack of rigidity allows CsCl crystallites to undergo four unique transformations: the (1) Bain and (2) shear transformations, which both produce the face-centered cubic CuAu (CuAu-fcc) superlattice, the (3) zig-zag transformation which produces the hexagonal close-packed CuAu superlattice (CuAu-hcp) and (4) a random combination of the zig-zag and shear transformations, which produces a random hexagonal close-packed (rhcp) superlattice. As discussed in the previous Chapter, hydrodynamic biasing leads to a preponderance of CuAu-fcc in systems with equally-sized particles, which is presumably formed by the low-drag shear deformation pathway.

Recent experiments in the Crocker lab have produced results which appear to contradict the observations and conclusions described in Chapter 2. Here, CuAu-hcp crystallites were observed, suggesting that the apparently high hydrodynamic resistance zig-zag transformation mode was operational. . An example of such a crystallite is shown below in Figure 3.1. This result is at odds with the theoretical picture presented in

Chapter 2, and also raises the question of why CuAu-hcp was not observed in earlier experiments.

The apparent discrepancy may be resolved by noting that the new experiments differ from the ones in Chapter 2 in an important way: the binding strength between particles of the same type was not kept constant across particle types, that is $E_{AA} \neq E_{BB}$, unlike the symmetric conditions employed in the prior experiments. On the other hand, this difference in the particle interaction matrix should have no impact on the hydrodynamic biases preventing the production of CuAu-hcp. In order to explain this explain this unexpected phenomenon we return to the mode tracking methods developed in Chapter 2, and apply them to determine how the interaction asymmetry leads to such a significant qualitative difference.

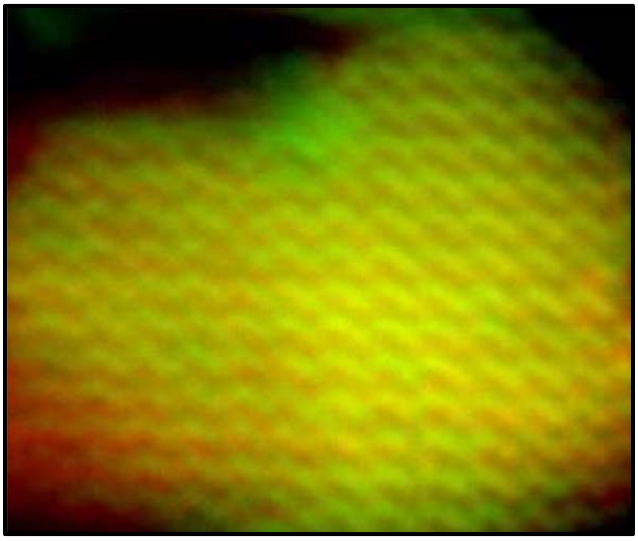

Figure 3.1: Example hcp crystallite observed in the Crocker Lab. This crystallite was observed when interactions between particles of type A (shown in red) were disabled, such that A particles only interact with B particles (shown in green) while B particles can

also interact with other B particles. Interactions between pairs of type A particles are purely repulsive.

In the following analysis, we employ the same Langevin dynamics simulations and vibrational analysis methods developed in Chapter 2 in order to understand the existence of these experimentally observed CuAu-hcp lattices. Additionally, we expand the approach to understand how the CsCl system behaves when the two particle species are unequal in size. Finally, we briefly examine how our approach may be used to model phase transformations unrelated to the CsCl superlattice.

3.2 Asymmetric Interaction Matrices

In an attempt to replicate in simulation the experimentally observed CsCl to CuAu-hcp transformation, a series of Langevin Dynamics simulations were performed using the LAMMPS software package (102). These simulations were initialized with CsCl crystallites containing 1837 particles each 400nm in diameter, with the viscosity of the implicit fluid set to 1% that of water. Note again that the viscosity does not appear to play a role in the establishing the hierarchy of transformation pathways—the 1% value was used solely to accelerate the simulations. In order to replicate experimental conditions, the binding strength between unlike particles were set to $6k_BT$, the binding strength between A particles was varied from 0 to $2k_BT$, and the binding strength between B particles was varied from 0.5 k_BT to $2k_BT$. Each simulation was allowed to evolve until the potential energy had reached some equilibrium value.

For simulations where the binding strength between A particles was less than $1k_BT$, the presence of a previously unobserved structure, which we refer to as Pseudo Close-Packed (pcp), was discovered; see Figure 3.2. The unit cell of the pcp lattice is orthorhombic with relative edge lengths of 1.0, 1.1, and 9.3. There are 16 particles per unit cell with type A particles located at (1/4-0.01, 1/4, 0.269), (1/4-0.01, 3/4, 0.269), (3/4-0.01, 1/4, 0.774), (3/4-0.01, 3/4, 0.774), (3/4+0.01, 1/4, 0.269), (3/4+0.01, 3/4, 0.269), (1/4+0.01, 1/4, 0.774), (1/4+0.01, 3/4, 0.774) and B particles are located at (1/2, 0, 0.0323), (1/2, 0, 0.505), (1/2, 1/2, 0.323), (1/2, 1/2, 0.505), (0, 0, 0.011), (0, 0, 0.538), (0, 1/2, 0.011), (0, 1/2, 0.538). Each particle exhibits 8 unlike particle contacts, B particles have one like particle contact, while A particles have zero like particle contacts.

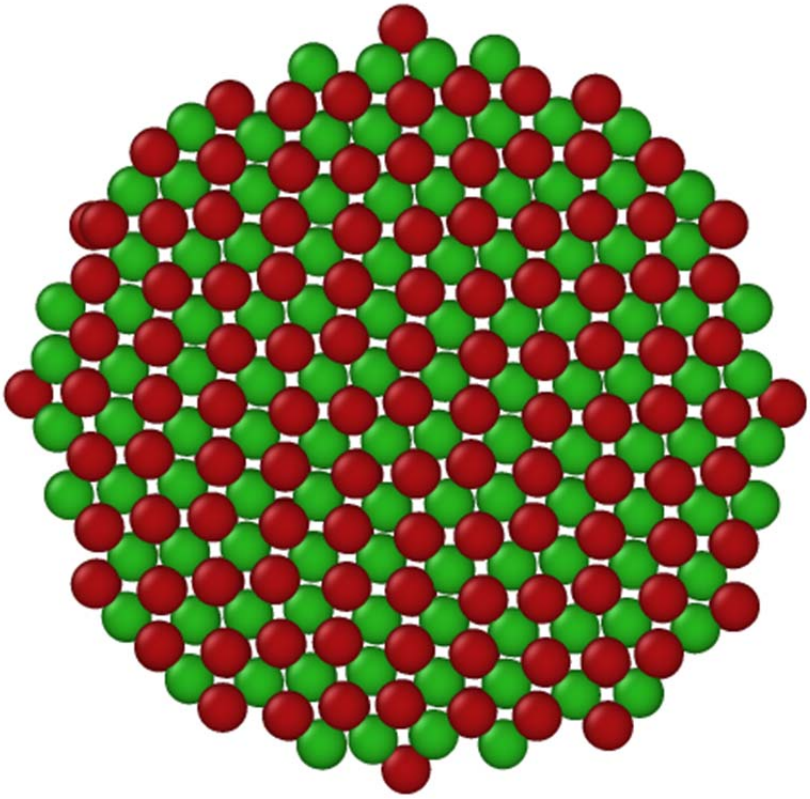

Figure 3.2: Example of the pcp structure observed in LD simulation. This structure was produced by performing an LD simulation on a CsCl crystallite seed containing 1837 particles. Binding strengths between A particles (shown in red) were set to $0k_BT$, between B particles were (shown in green) set to $1k_BT$ and between particles of unlike type were set to $6k_BT$. The CsCl crystallite rapidly transformed into the structure shown.

The pcp structure remains stable as long as the binding strength between A particles is ~$1k_BT$ lower than the binding strength between B particles, and the binding strength between B particles is below ~$2k_BT$. However, increasing either of these binding strengths beyond these limits will cause the crystallite to rapidly transform a second

time, producing rhcp. An overview of the two observed transformations is shown below in Figure 3.3.

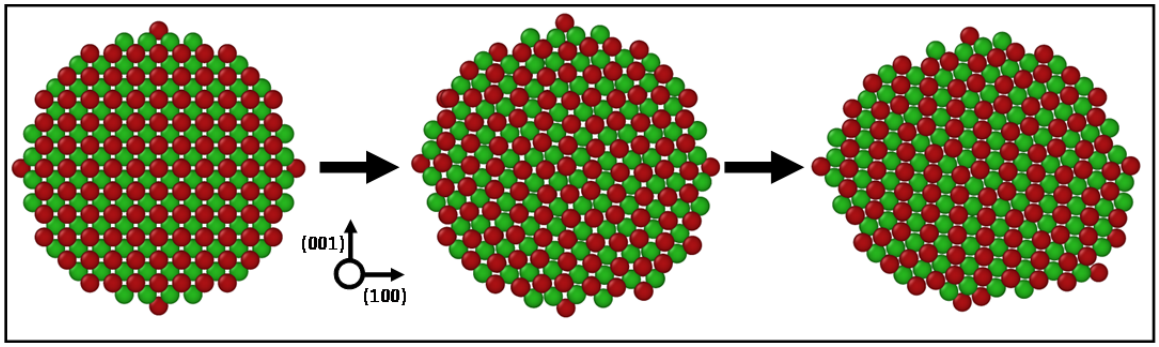

Figure 3.3: Overview of the CsCl to pcp and pcp to RHCP transformations observed in LD simulations. The initial configuration, shown on the left, is a CsCl crystallite containing 1837 particles. Performing an LD simulation with this CsCl crystallite as the seed structure, with binding strengths between A particles (shown in red) set to $0k_BT$, between B particles (shown in green) set to $1k_BT$ and between particles of unlike type set to $6k_BT$, results in rapid transformation into the pcp crystallite shown in the center. Upon increasing binding strengths between A particles to $1k_BT$, the crystallite transforms a second time, producing the rhcp crystallite shown on the right.

It is not immediately obvious how to model this transformation using the zero-frequency mode analysis method presented in Section 2.3. However, close examination of the transformation makes it clear that previous analysis of the transformation pathways available to the CsCl superlattice had been unnecessarily constrained. In all prior transformations we had assumed that every adjacent (110) modelet must move relative to one another in order for the crystallite to transform. However, after the pcp

producing transformation has occurred, every other pair of adjacent (110) planes has experienced little to no relative motion. With this in mind, it becomes clear that in order to replicate the pcp producing transformation using the zero-frequency mode evolution method we must require that each modelet only moves relative to *one* of its two neighboring modelets.

Before describing the specifics of the transformation, it is worth noting that similarly to the CP producing transformations, which can produce CuAu-fcc, CuAu-hcp, or CuAu-rhcp, this transformation type has two variants, which produce either pcp or random psuedo close-packed (rpcp). The pcp producing transformation, which we refer to as the “half-step” transformation requires that every other pair, and only every other pair, of adjacent modelets move relative to one another, in a single direction, which must be consistent across the entirety of the crystallite. Using the notation introduced in Section 2.4, an example of a valid pathway described as the relative motion between sequential adjacent modelets would be: +c, 0, +c, 0, where c is an arbitrary measure of the relative velocity between (110) modelets. The pcp producing transformation is shown below in Figure 3.4 along with the corresponding CsCl modelets. The rpcp producing transformation differs from the pcp producing transformation only in that it does not necessitate that all motion between adjacent modelets be in a single direction across the crystallite.

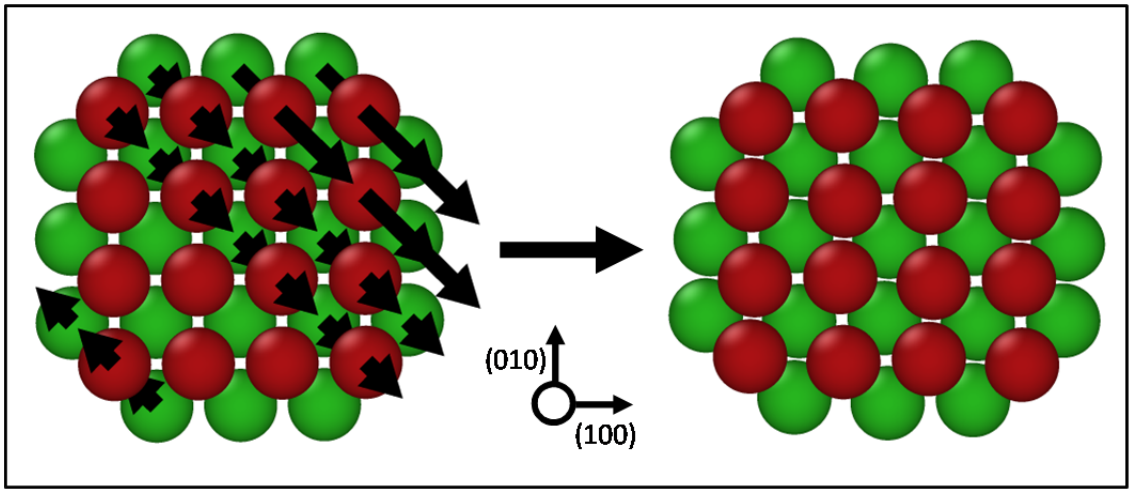

Figure 3.4: (001) view of the pcp producing transformation. The initial transformation pathway is shown on the left, superimposed on a CsCl crystallite. The resulting pcp crystallite is shown on the right. The pcp lattice was produced by evolving a CsCl crystallite seed containing 200 particles each with a diameter of 400nm along the pcp transformation pathway using the method described in Section 2.3. A particles are shown in red, B particles are shown in green.

While the pcp and rpcp lattices are both mechanically stable, we can also observe them "completing" their transformation into a close-packed lattice. Although the stationary modelet pairs associated with the pcp transformation are no longer fully non-rigid, their rigidity is very weak, allowing us to continue to employ the zero-frequency evolution method in the same manner as previously used for zero-frequency modelets by treating any vibrational mode with a frequency eight orders of magnitude smaller than that of a single particle pair as if it had a frequency of zero. The transformation pathway itself, which we refer to as either "psuedo-shear", if it produces CuAu-fcc, or "psuedo-zig-

zag", if it produces CuAu-hcp, is simply the "complement" of the pathway taken to produce the pcp lattice. For example, given that the shear pathway to directly transform a CsCl lattice into CuAu-fcc is: +c, +c, +c, +c and that the pcp lattice can be produced via the pathway:+c, 0, +c, 0, transforming the pcp lattice into CuAu-fcc requires the pathway:0, +c, 0, +c. Examples of pcp to CuAu-hcp and CuAu- fcc transformations are shown below in Fig 3.5.

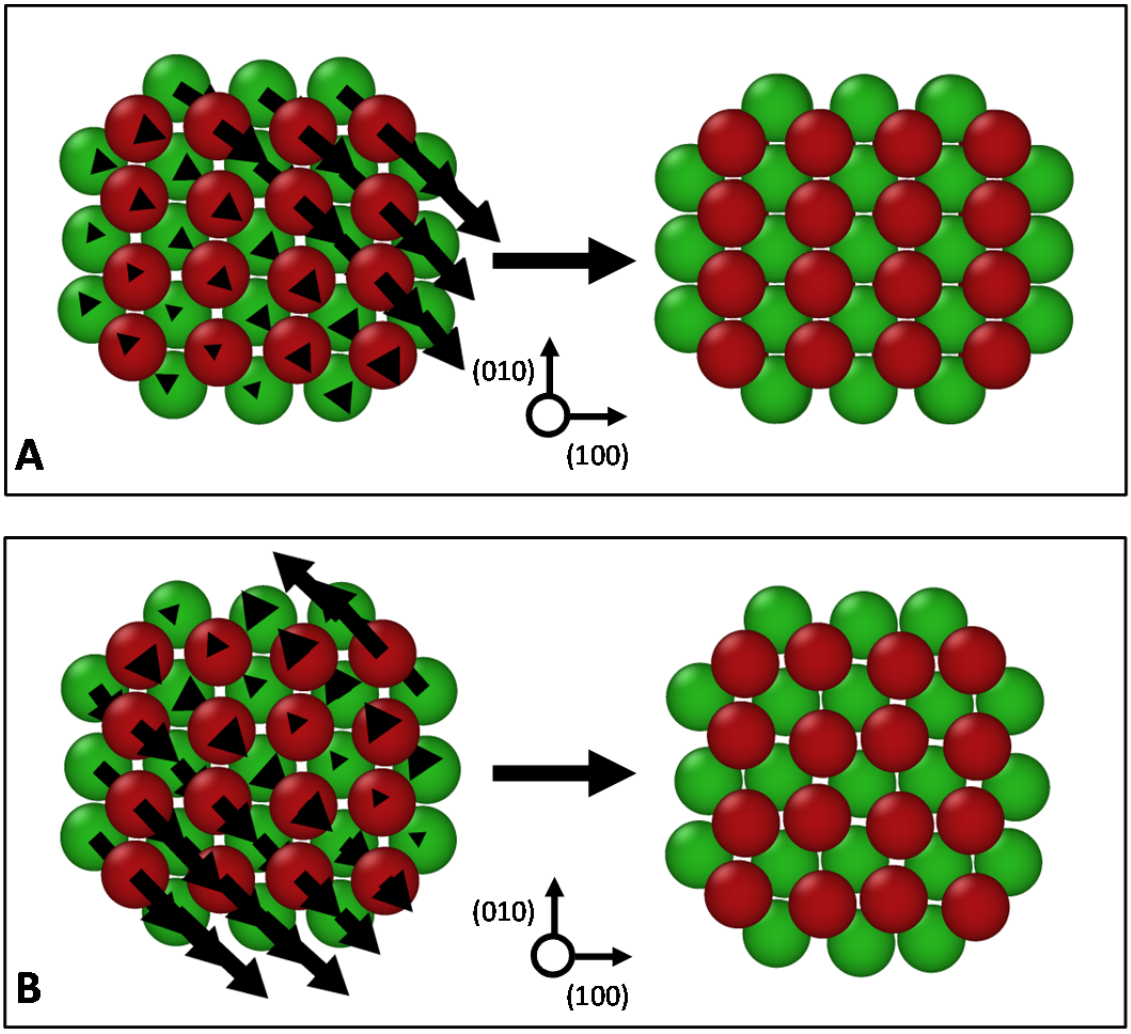

Figure 3.5: (001) view of the pcp to CuAu-fcc (A) and CuAu-hcp (B) producing transformations. The initial transformation vector is shown on the left, superimposed on a pcp crystallite. The crystallites resulting from these transformations are shown on the right. The transformations were performed by evolving a pcp crystallite seed containing 200 particles with a diameter of 400nm along the “psuedo-shear” and “psuedo-zig-zag” transformation pathways using the zero-frequency mode evolution method described in Section 2.3. A particles are shown in green, B particles are shown in red.

The most interesting aspect of the two-step transformation, $CsCl \rightarrow PCP \rightarrow CP$, is that it allows for a hydrodynamically favorable pathway from CsCl to CuAu-hcp. If one considers only direct $CsCl \rightarrow CP$ transformations, no CuAu-hcp producing transformation is available, as the only CuAu-hcp producing pathway: $+c,-c,+c,-c$ requires alternating modelet pairs to move in opposite directions, which is hydrodynamically unfavorable, as detailed in Section 2.4. However, with an already transformed pcp lattice produced via the pathway $+c,0,+c,0$, it is clear that this lattice can transform into either CuAu-hcp via the pathway $0,-c,0,-c$ or CuAu-fcc, using $0,+c,0,+c$. These transformations are hydrodynamically equivalent. In both cases, all movement during a single step of the transformation is in the same direction, and so both transformations experience the same total drag force. Thus, if at any point during the crystallite growth process, system conditions change from favoring pcp to cp, one would expect to see a roughly 50/50 split between perfect CuAu-hcp and CuAu-fcc crystallites. This explains the experimental presence of CuAu-hcp as discussed in Section 3.1. An overview of the full transformation network connecting CsCl, CuAu-hcp, CuAu-fcc, and pcp is shown below in Figure 3.6.

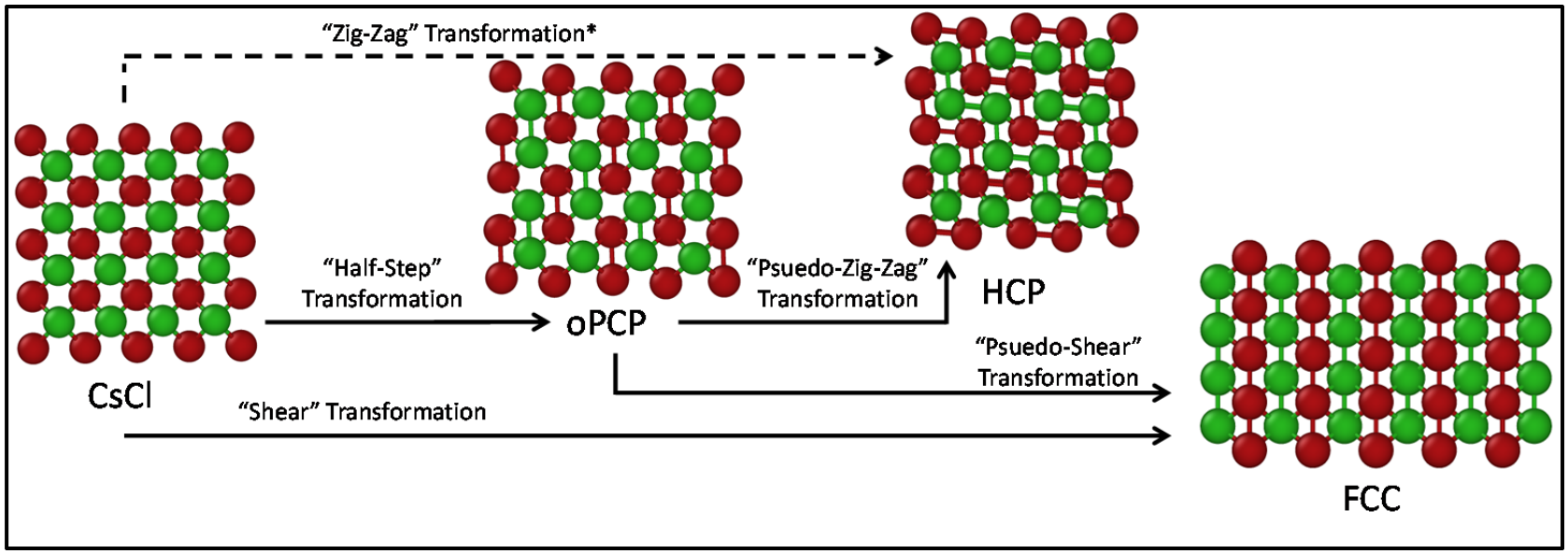

Figure 3.6: Complete diagram illustrating the transformations available to the CsCl superlattice. A particles are colored red, B particles are colored green. Bonds connecting neighboring particles indicate only that they are within interaction range of one another. The CsCl lattice is shown from its (100) orientation, and all other lattices show the same face after it has been transformed. The dotted line directly connecting CsCl to hcp indicates that while the transformation is physically possible, it is not experimentally observed due to a negative hydrodynamic bias.

3.3 Asymmetry in Size and Interaction

Additional experiments have recently been performed using particles of different sizes. Here, four distinct crystalline superlattices are observed: CsCl, CuAu-fcc, and two variants of the IrV superlattice, which we refer to as the “Basketweave” (BIrV) and “Herringbone” (HIrV) variants. Two factors immediately suggest that solid-solid phase transformations may play a role in this new system: first, the CsCl superlattice has retained its non-rigid properties at this size ratio and second, the CuAu-fcc superlattice is still observed. This suggests that at least one of the two CsCl to CuAu-fcc transformations may still exist. In order to determine if any transformations indeed exist in this system we will analyze it using the methods developed in Section 2.

First, in order to determine if the IrV lattices are in fact connected to the CsCl superlattice through some transformation, a series of LD simulations were performed under conditions chosen to match the experiments as closely as possible. These simulations were initialized with CsCl crystallites containing 1500 to 4285 particles, with the large (B) particles set to a diameter of 500nm and the small (A) particles set to a diameter of 425nm. Binding strengths between unlike particles were set to $6k_BT$, like particle binding strengths between Type A and Type B particles were independently varied from 0 to $4k_BT$. The viscosity of the fluid was again set to 1% that of water. Each simulation was allowed to evolve until the potential energy had equilibrated. For runs where the binding strength between B particles was at least 1 k_BT, the crystallite was observed to transform into a random mixture of HIrV and BIrV superlattice structures,

which we henceforth refer to as RIrV. An overview of this transformation is shown below in Figure 3.7.

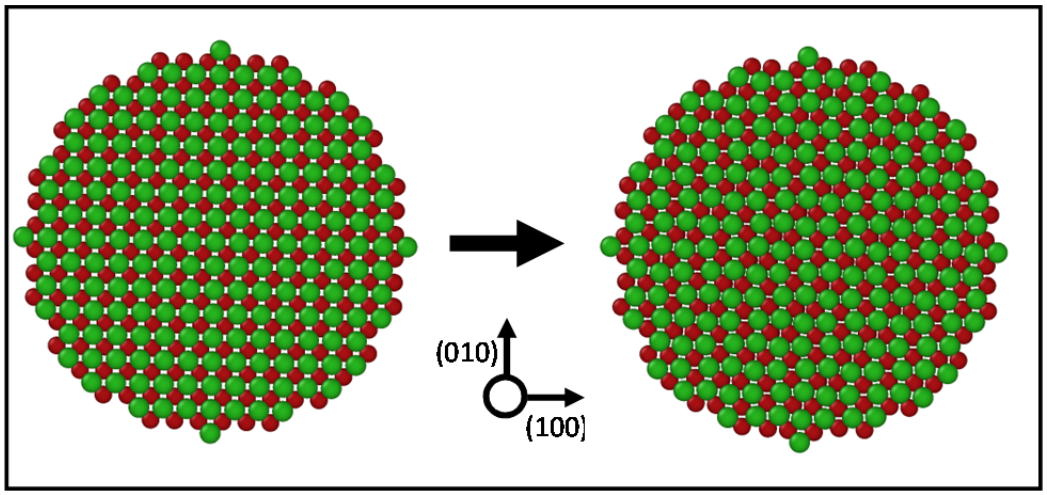

Figure 3.7: Overview of the CsCl to RIrV transformation process observed in LD simulations. The initial configuration, shown on the left is a CsCl crystallite containing 4285 particles. Performing an LD simulation with this CsCl superlattice as the seed structure, with binding strengths between A particles (shown in red) set to $0k_BT$, between B particles (shown in green) set to $1k_BT$ and between particles of unlike type set to $6k_BT$, results in a RIrV crystallite, shown on the left. The RIrV lattice is a random combination of the HIrV and BIrV lattices.

The behavior observed in these LD simulations is very similar to what was observed in the simulations performed on same-size binary systems described in Section 2.2, with both sets of simulations producing random mixtures of two superlattice

configurations. This equivalence suggests that the transformation occurring at the 0.85 size ratio may be similar to the random combination of shear and zig-zag transformations observed at the 1.0 size ratio. In order to determine if there is in fact such a connection, both the shear and zig-zag transformation pathways were used to evolve a 0.85 size ratio CsCl crystallite using the zero-frequency mode evolution method described in section 2.3. These simulations were found to be only partially successful. While it was possible to produce both HIrV and BIrV by transforming along a path which is initially identical to the zig-zag and shear modes, the paths were found to change abruptly partway through the transformation when some of the larger particles came into contact. At this point in the transformation, the number of zero frequency modes was found to be reduced dramatically by up to ~95%, depending on the shape and size of the crystallite, forcing the system to change direction and find a new pathway to continue the transformation. Using small crystallites containing fewer than ~30 particles it was possible to reduce the remaining zero frequency modes to one, allowing for easy isolation of the final transformation vector. The resulting “two-step” transformation pathways which produce HIrV and BIrV are illustrated below in Figure 3.8.

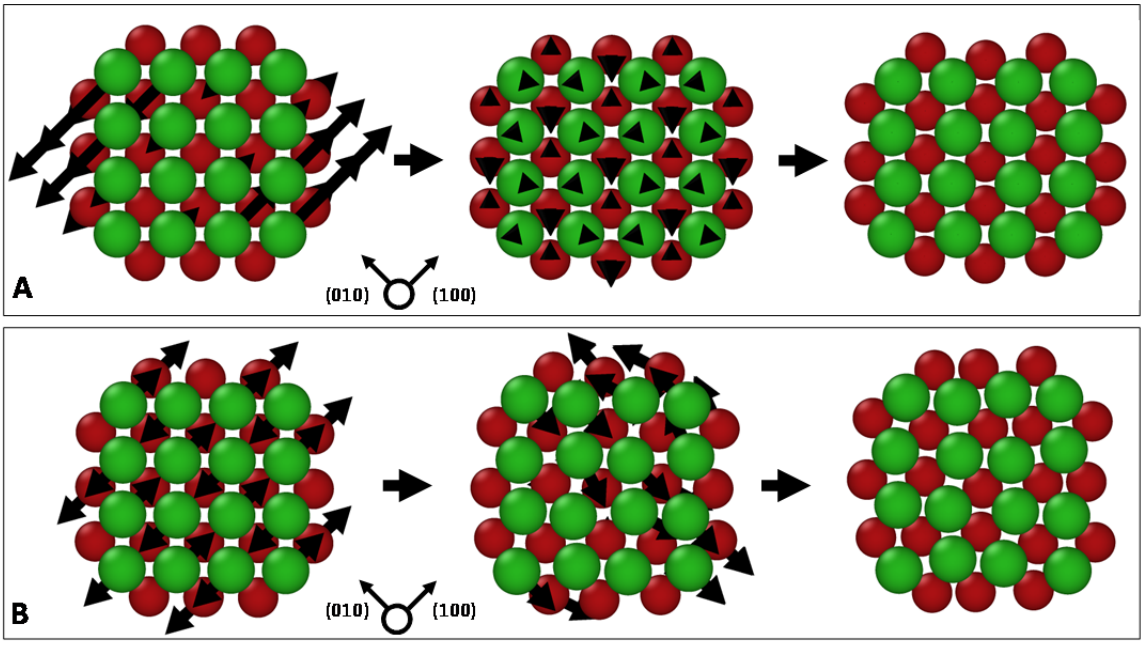

Figure 3.8: Overview of the transformation pathways between the CsCl superlattice and the BIrV (A) and HIrV (B) superlattices. Arrows indicate the displacement direction at the start of the transformation. The initial CsCl crystallite is shown on the left. The middle crystallites indicate the structure once the initial transformation direction no longer exists. The crystallites shown on the right indicate the final IrV structure resulting from the transformation, and are generated by following the transformation pathways indicated on the middle crystallite. Transformation pathways were generated and followed using the method described in Section 2.3. The 500nm type B particles are shown as green and the 425nm type A particles are shown as red.

While these transformations do explain some of the experimental results, two outstanding issues remain unresolved. First, the shear mode, which produced CuAu-fcc in the 1.0 size ratio CsCl crystallites, produces BIrV in the 0.85 size ratio system, as

shown in Figure 3.8. However, CuAu-fcc is still observed experimentally at this size ratio. Secondly, the HIrV-producing transformation utilizes the same zig-zag pathway which was previously demonstrated to be hydrodynamically unfavorable in Section 2.4. Below we show that both of these apparently unresolved discrepancies may be resolved straightforwardly.

Regarding the first issue, while it is true the shear transformation is no longer capable of producing CuAu-fcc, the Bain transformation, which is still operational at the 0.85 size ratio, may be invoked. The 0.85 size ratio CuAu-fcc Bain transformation is demonstrated below in Figure 3.9. While the Bain transformation is not hydrodynamically favored against the shear transformation, the frequency with which CuAu is observed experimentally is much lower in the 0.85 size ratio system, with fewer than 5% of crystallites exhibiting CuAu-fcc characteristics, as opposed to nearly 100% of transformed crystallites in the 1.0 size ratio system. This frequency appears to be reasonable given the lower hydrodynamic favorability of the only CuAu-fcc producing transformation.

The hydrodynamic bias against the zig-zag transformation can be explained by invoking the pcp lattice. Here, the pcp lattice acts as an intermediate structure between the CsCl and HIrV at a size ratio of 0.85 in much the same way as it did between the CsCl and CuAu-hcp lattices at a size ratio of 1.0. The CsCl to pcp to HIrV transformation is demonstrated below in figure 3.10.

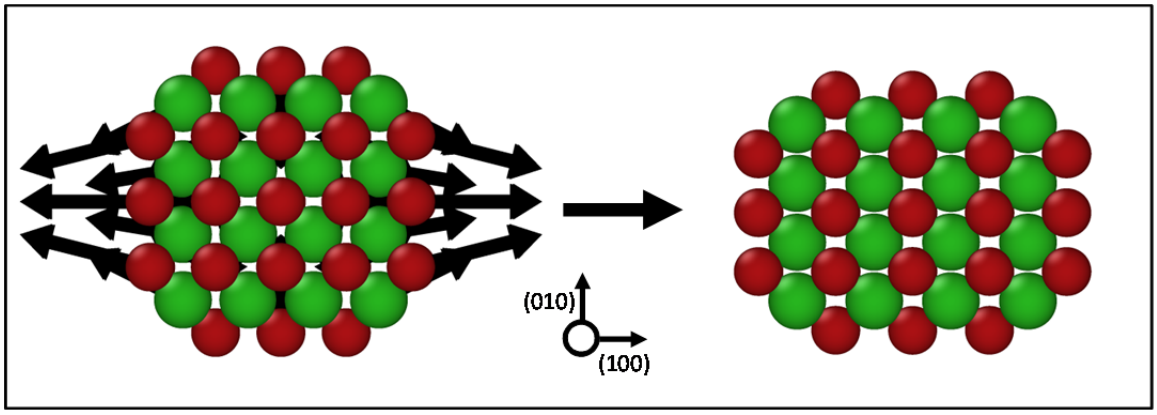

Figure 3.9: Overview of the Bain transformation pathway between the CsCl superlattice and the CuAu-fcc superlattice at a size ratio 0.85. Arrows indicate the displacement direction at the start of the transformation. The initial CsCl crystallite is shown on the left, and the fully transformed CuAu-fcc crystallite is shown on the right. The transformation pathway was generated and followed using the method described in Section 2.3. 500nm B particles are shown as green and 425nm A particles are shown as red.

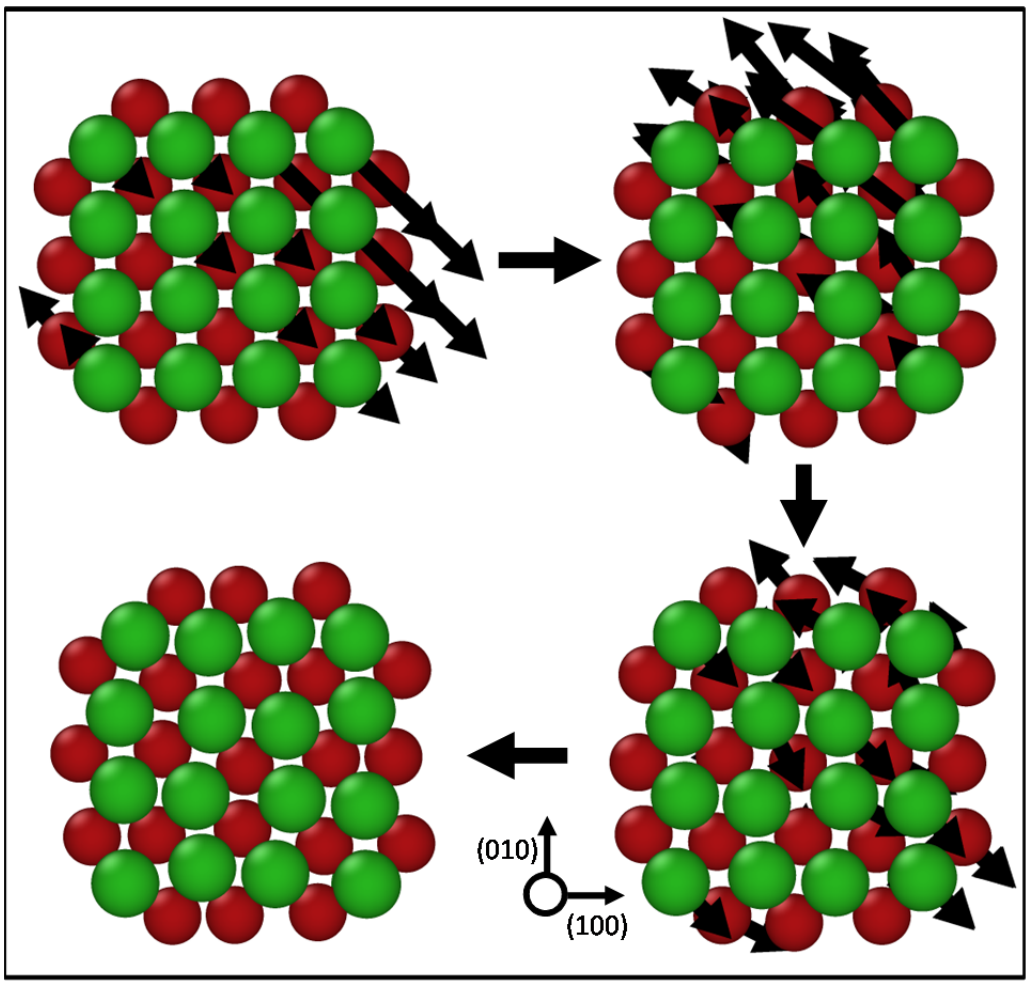

Figure 3.10: Overview of the CsCl to HIrV transformation using the pcp phase as an intermediate. Arrows indicate the displacement direction at the start of the transformation. The transformation proceeds clockwise starting from the initial CsCl crystallite shown in the upper left. The second crystallite has a pcp structure, the third structure is an intermediate between CsCl and HIrV and the fourth structure is HIrV. The 500nm B particles are shown as green and the 425nm A particles are shown as red.

Ultimately, the full network of transformations available to the CsCl superlattice at a size ratio of 0.85 closely mirrors that of the 1.0 size ratio system. The 0.85 size ratio IrV producing transformations are very similar to the 1.0 size ratio cp producing transformations, with both having two potential variants: Herringbone and Basketweave, in the case of IrV, and CuAu-hcp and CuAu-fcc in the case of cp. Beyond the cp to IrV comparison the only real difference is that, while the Bain transformation produces CuAu-fcc at both size ratios, the shear transformation does not. The overall transformation network for the 0.85 size ratio CsCl system is summarized below in Figure 3.11.

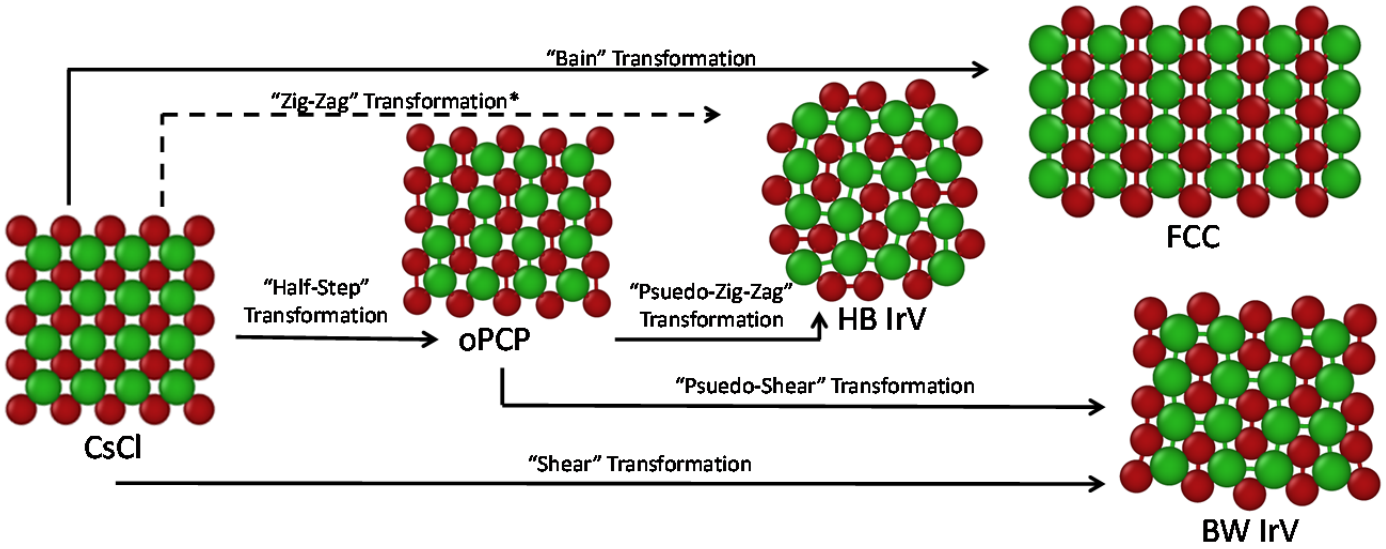

Figure 3.11: Complete diagram illustrating the transformations available to the CsCl superlattice at a size ratio of 0.85. A particles are colored red, B particles are colored green. Bonds connecting neighboring particles indicate are within interaction range. The CsCl lattice is shown from its (100) orientation, and all other lattices show the same face after it has been transformed. The dotted line directly connecting CsCl to HIrV indicates that while the transformation is physically possible, it is not experimentally observed due to hydrodynamic biases.

3.4 Phase Transformations Beyond the CsCl Superlattice Family

The CsCl superlattice is not alone in exhibiting zero frequency deformation modes. The NaCl superlattice is observed experimentally to be the stable morphology for binary systems with a size ratio between 0.41, where its structure is rigid and 0.565. An overview of the size ratios accessible to the CsCl and NaCl superlattices is shown below in Figure 3.12. At any size ratio above its minimum value of 0.41, this structure exhibits zero frequency vibrational modes. In fact, at size ratios where the NaCl superlattice is non-rigid, it exhibits far more of these modes than the CsCl system, and cannot be fully described using the (110) modelet basis. Depending on shape, a NaCl crystallite 110 particles in size will have approximately 80 zero-frequency modes while a CsCl crystallite of the same size will have only approximately 30.

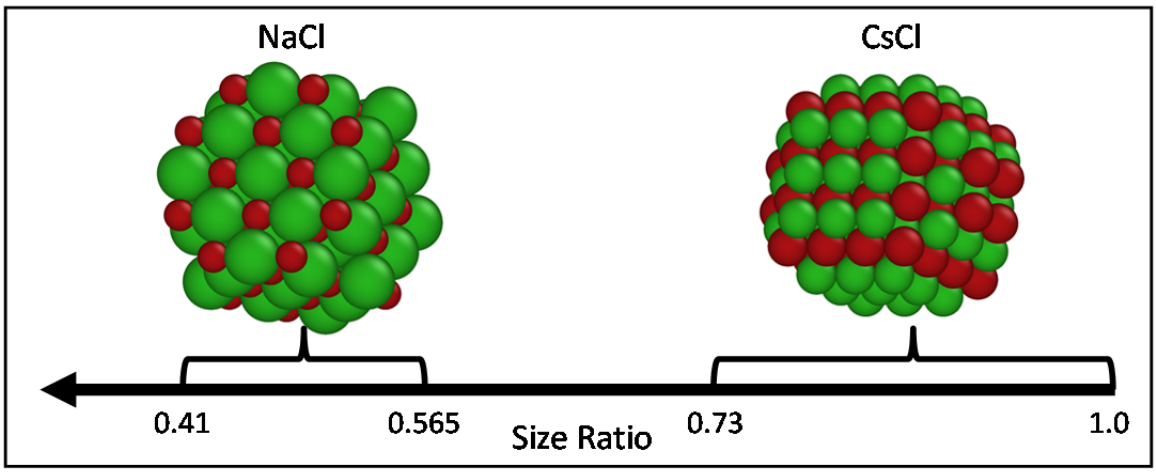

Figure 3.12: Parent structures of DNA linked colloidal assemblies and their associated size ratio ranges. Example CsCl and NaCl crystallites are shown at size ratios of 0.85

and 0.565, respectively. In the range between 0.565 and 0.73, no crystallites have been observed experimentally.

The “pinning” technique, used to identify (110) modes as the fundamental modelet of the CsCl superlattice in Section 2.3, was also used here to determine the fundamental modelet of the NaCl system. The fundamental NaCl modelet was found to be a single column of particles aligned along a (100) vector moving in the same direction as that (100) vector. An example of such a modelet is shown below in Figure 3.13.

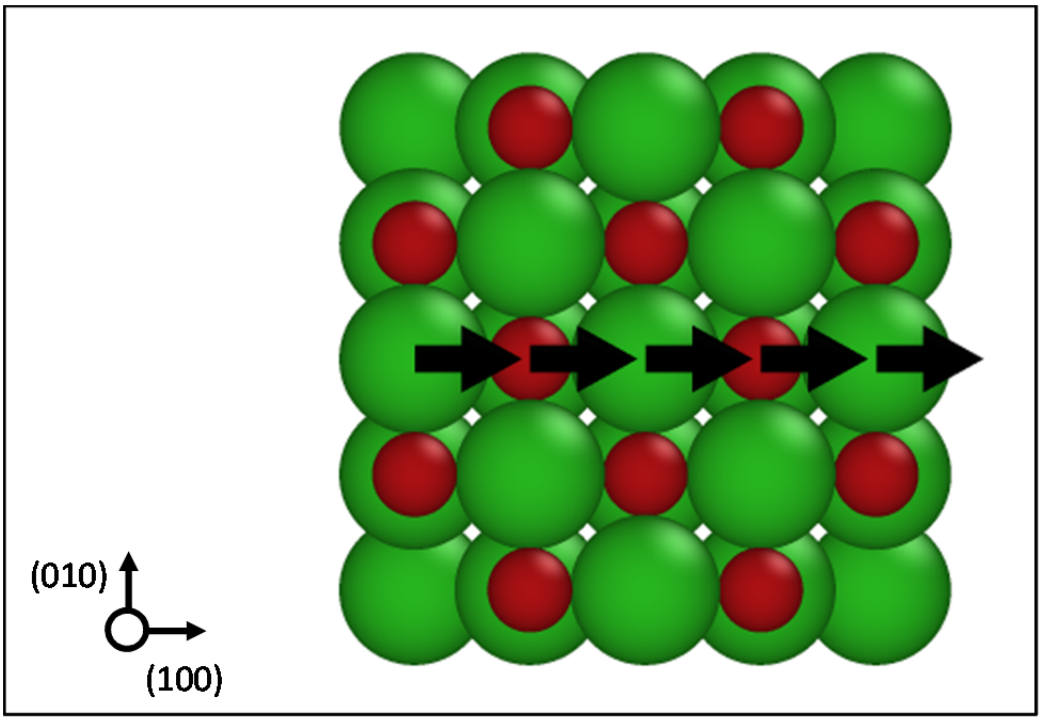

Figure 3.13: Example of a single (100) NaCl superlattice modelet. Only a single column of particles in the (100) direction are associated with this modelet. Particles are shown at

a size ratio of 0.565. Type A particles are colored red and have a radius of 158nm, type B particles are colored green and have a radius of 280nm.

While the highly flexible nature of the NaCl superlattice suggests access to a significant number of transformations, only one transformation has been observed experimentally, a crystal-wide shear of the (001) facing planes in the (110) direction at a particle size ratio of 0.565. In order to identify the transformation vector associated with this deformation, we begin with the assumption that the direction of the initial transformation vector for each individual particle is close to the total displacement vector over the full transformation, which we refer to as $\Delta\mathbf{x}_{total}$. With this assumption in mind, we are able to determine an initial set of transformation modelets using eq (2.14) from Section 2.3, shown again below.

$$\mathbf{v}_T^{new} = \mathbf{K}\left[\left(\mathbf{K}^T\mathbf{K}\right)^{-1}\left(\mathbf{K}^T\mathbf{v}_T^{old}\right)\right] \tag{3.1}$$

This expression is used to project the previous step in a zero-frequency mode evolution, $\mathbf{v}_T^{old}$, onto the current kernel of the Hessian matrix, $\mathbf{K}$, in order to determine the next step in the system evolution, $\mathbf{v}_T^{new}$. Here we replace $\mathbf{v}_T^{old}$ with our previously described guess at the initial (110) shear transformation vector, $\Delta\mathbf{x}_{total}$. Solving the resulting expression for $\mathbf{v}_T^{new}$ provides us with the zero-frequency pathway in the NaCl crystallite which is closest to $\Delta\mathbf{x}_{total}$. This approach has proven to be successful, and the initial transformation pathway calculated using this approach and fully transformed structure are shown below in Figure 3.14.

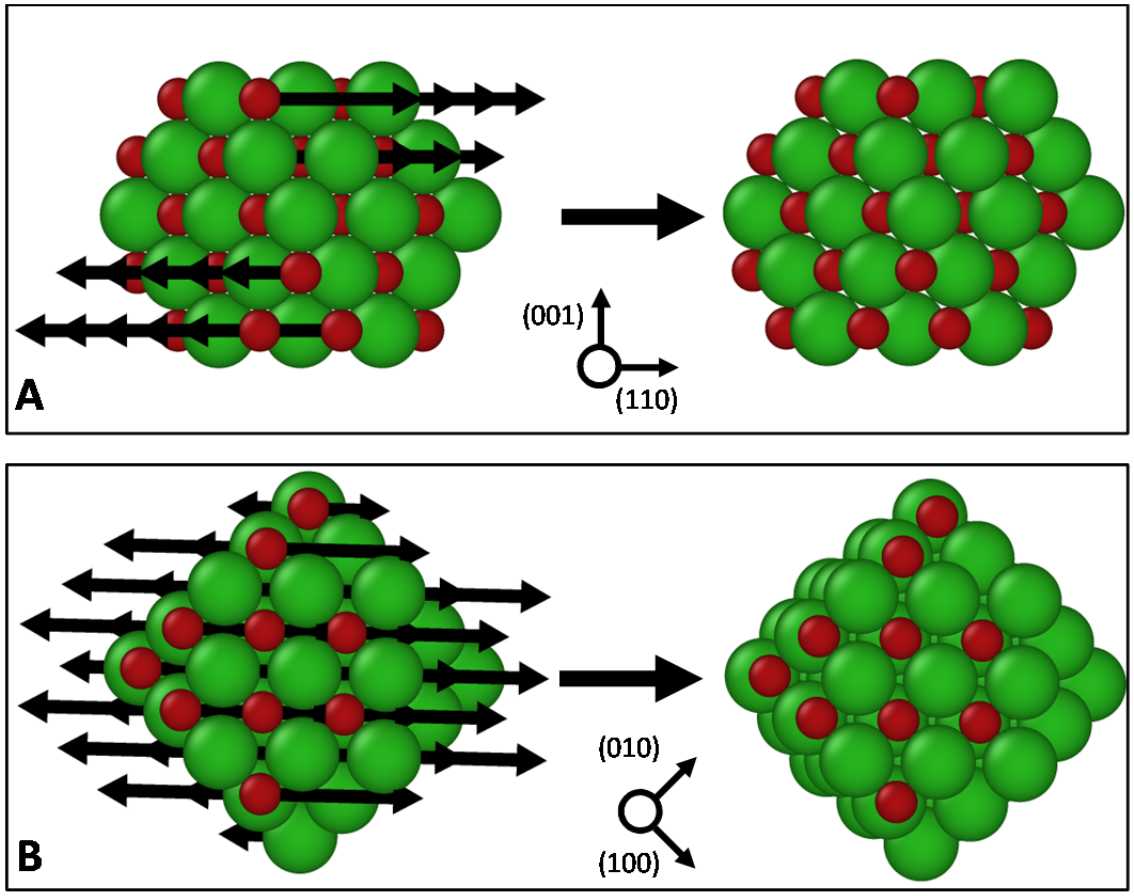

Figure 3.14: (-110) (A) and (001) (B) perspective of the (110) shear in the NaCl superlattice. The initial transformation pathway is shown on the left, the final product structure is shown on the right. A crystallite containing 110 particles at a size ratio of 0.565 was used. A particles are colored red and have a radius of 158nm, B particles are colored green and have a radius of 280nm.

3.5 Conclusions

Previous work on the 1.0 size ratio CsCl superlattice had indicated that there were four competing solid-solid phase transformations: two producing CuAu-fcc, one producing CuAu-hcp and one producing CuAu-rhcp. However, these studies were constrained to systems in which both like-particle binding strengths were equal, that is $E_{AA} = E_{BB}$. Upon discarding this constraint, the presence of the pcp phase and its "partial" phase transformation from CsCl was revealed. While this is noteworthy by itself, the pcp lattice is also capable of transforming further, producing either CuAu-fcc or CuAu-hcp. Furthermore, the two step nature of this transformation allows the CuAu-hcp producing transformation to occur without experiencing the enhanced hydrodynamic drag effect previously thought to prevent the formation of the CuAu-hcp lattice in experiment. As a result, this two-step transformation pathway provides the only known mechanism for producing high quality CuAu-hcp from systems of DNA functionalized colloidal particles.

Study of CsCl crystallites constructed of particles at a size ratio of 0.85 revealed that the set of transformations available is qualitatively similar to those available at a size ratio of 1.0. The zig-zag and shear transformations still exist, but now follow slightly altered pathways and produce BIrV and HIrV, in place of CuAu-hcp and CuAU-fcc, respectively. Additionally, the pcp lattice can still be used to bypass the hydrodynamic bias against the zig-zag transformation, as seen at a size ratio of 1.0. Finally, study of the NaCl superlattice constructed from size ratio 0.565 particles reveals that phase transformations in systems of DNA functionalized colloidal particles exist outside the CsCl superlattice system. The zero-frequency mode spectrum of the NaCl superlattice

can be described using (100) modelets in the same manner the CsCl superlattice can be described using (110) modelets. While the NaCl superlattice is significantly less rigid than the CsCl superlattice, it has only been observed to undergo one transformation in experiments to date, namely a simple (110) shear of the (100) facing planes, which is easily replicated using the zero-frequency mode evolution method.

Both the prevalence and complexity of solid-solid phase transformations in crystallites constructed from DNA-functionalized colloidal particles is significantly greater than previously thought. Transformations pathways previously believed to be inaccessible due to hydrodynamic biases can now be bypassed entirely by making use of a newly identified intermediate phase: pcp. Additionally, it has been determined that solid-solid phase transformations exist at both size ratios outside of 1.0 and even in lattices completely unrelated to CsCl, such as NaCl.

4. THE SUPRISING ROLE OF INTERACTION HETEROGENEITY IN COLLOIDAL CRYSTALLIZATION

4.1 Introduction

The ability to arbitrarily design DNA oligonucleotide sequences for use in DNA functionalized self-assembly allows for the creation of a large library of distinct interactions among a collection of particles (33, 115-117). Numerous modeling and simulation efforts, based on accurate descriptions of the inter-particle interactions (40, 69, 82, 84, 96), have identified thermodynamic (42, 87, 118) and kinetic (9, 68, 99, 119-121) bottlenecks for successful crystallization. Perhaps most fundamental of these is the need for moderate inter-particle binding strengths—too weak and the nucleation rate of crystallites is slow or fails to occur altogether, too strong and the system is trapped irreversibly in a disordered state (119, 122-126). The *width* of this crystallization window, which in DNA-mediated assembly typically corresponds to a narrow temperature range for crystal formation, appears crucial. Micron-scale DNA colloids, in particular, are characterized by very narrow crystallization windows due to the short-ranged attraction relative to the particle size, being in the so-called 'sticky-sphere' limit (123, 125-127) made worse by the sharpness of the DNA melting transition. Consequently, several approaches for engineering the crystallization window have been proposed, including temperature cycling (120), introducing mobile DNA strands on particle surfaces (128, 129), and via intra-particle interactions to modify the phase behavior (49, 70, 130, 131). Despite these advances, it remains the case that while some particle formulations crystallize readily, other formulations with seemingly similar physical parameters (e.g., DNA density) do not crystallize at all (53) for reasons that remain poorly understood.

More generally, other sticky sphere systems (such as micellar depletion attraction between micron-scale colloids) are observed to crystallize under some conditions (132-135) while theoretically gelation is expected and more typically observed (125).

Here, we propose, based on a computational analysis, that the currently unexplained variability of the crystallization of DNA-grafted microspheres (and other types of sticky-sphere colloids) is attributable to a previously unrecognized factor—interaction heterogeneity. Specifically we show that *population* heterogeneity in the grafted DNA oligonucleotide density across particles (distinct from *single-particle* heterogeneity in the spatial distribution of strands on one particle), which produces a distribution of interaction strengths, also leads to increased crystallization robustness by (1) lowering the mean binding energy needed for crystallization, and (2) increasing the width of the crystallization window. This is unexpected given that heterogeneity of any type is conventionally regarded as being detrimental to crystallization, e.g., particle size polydispersity greater than 6% tends to inhibit crystallization in hard-sphere systems (136). There is anecdotal support of our finding in the literature: Casey (137) has reported that one DNA-colloid formulation approach that led to better crystallization also led to a wider dispersion in the DNA density among individual particles. More generally, we suggest a practical route for engineering more robust nucleation and crystallization behavior, through the intentional control of interaction heterogeneity.

4.2 Method

We consider a single-component system of 1 micron-diameter spherical particles that interact via the coarse-grained model of Rogers *et al*.(82). For this system, the close-packed rhcp crystal is the ground state configuration that forms upon

crystallization. Inter-particle interaction heterogeneity was modeled by randomly assigning each particle, i, a binding multiplier, b_i, where the value of b_i is generated from a Gaussian distribution with unit mean and standard deviation *p*. The interaction potential energy between two particles, *i* and *j*, is given by

$$U_{ij}(r) = b_i b_j U_{DNA}(r), \tag{4.1}$$

where $U_{DNA}(r)$ represents the base DNA potential energy as a function of inter-particle separation. One possible physical origin of such heterogeneity would be if different particles contained differing, fixed amounts of grafted DNA, which would lead to a multiplicative effect approximately as in eq. (4.1). For example, the experiments by Casey (137) reported a heterogeneity of *p* = 0.15 was favorable for crystallization.

Nucleation free energy profiles for crystallites as a function of size were computed using an approach based on a recently-introduced, computationally efficient, variant of umbrella sampling (138). To demonstrate this approach we begin by considering the probability of observing a crystallite of a particular size, $\hat{n}$, in a system under the influence of some bias energy, U_B, such that

$$P_B(\hat{n}) = \frac{1}{Z_B}\int e^{-\beta\left(H(\mathbf{r})+U_B(n(\mathbf{r}))\right)}\delta(n,\hat{n})d\mathbf{r}, \tag{4.2}$$

where Z_B is the partition function of the biased system and $H(\mathbf{r})$ is the Hamiltonian of the unbiased system for a (3*N*-dimensional) particle configuration, **r**. Separating out the biased contribution to the system energy gives the expression

$$P_B(\hat{n}) = \frac{Z}{Z_B}e^{-\beta U_B(\hat{n})}\frac{1}{Z}\int e^{-\beta(H(\mathbf{r}))}\delta(n,\hat{n})d\mathbf{r}, \tag{4.3}$$

where Z is the partition function of the unbiased system. This expression may be restated as

$$P_B(n) = \frac{Z}{Z_B} e^{-\beta U_B(n)} P(n), \tag{4.4}$$

where the 'hat' designation has been dropped. Taking the natural logarithm and defining the free energy of all microstates corresponding to crystallite size *n* as $\beta A(n) = -\ln P(n)$ eq. (4.4) becomes

$$\beta A(n) = \beta A_B(n) - \beta U_B(n) + \ln\left(\frac{Z}{Z_B}\right). \tag{4.5}$$

Next we take the derivative of this expression with respect to n to obtain

$$\frac{\partial A(n)}{\partial n} = \frac{\partial A_B(n)}{\partial n} - \frac{\partial U_B(n)}{\partial n} + \frac{\partial}{\partial n}\ln\left(\frac{Z}{Z_B}\right). \tag{4.6}$$

Note that two simplifications may be made to this expression. First, the value of the term $\frac{\partial}{\partial n}\ln\left(\frac{Z}{Z_B}\right)$, is always zero, because the partition functions are integrated over all particle configurations and are thus independent of the instantaneous configuration. Second, at equilibrium in the biased ensemble $\frac{\partial A_B(n)}{\partial n}$ is also zero. Finally, assuming that the equilibrium value of n is close to its ensemble average, $\langle n \rangle_k$, and choosing a bias energy of the form

$$U_B = \frac{k}{2}(n - n_T)^2, \tag{4.7}$$

where k is the bias strength (0.125 $k_B T$ for all simulations) and n_T is the target crystallite size gives

$$\left\langle \frac{\partial A}{\partial n} \right\rangle_k = -\left\langle \frac{dU_B}{dn} \right\rangle_k = -k\left(\langle n \rangle_k - n_T \right). \tag{4.8}$$

Performing biased simulations over a range of target crystallite sizes then allows for the calculation of a free energy profile as a function of crystallite size using a finite difference approximation for eq. (4.8), i.e.,

$$\frac{A\left(\langle n \rangle_k^{i+1}\right) - A\left(\langle n \rangle_k^{i}\right)}{\langle n \rangle_k^{i+1} - \langle n \rangle_k^{i}} \approx -\frac{1}{2}k\left(\langle n \rangle_k - n_T \right)^{i+1} - \frac{1}{2}k\left(\langle n \rangle_k - n_T \right)^{i}, \tag{4.9}$$

where the superscript *i* represents the i^{th} biased simulation. The free energy is defined to be zero in the limit of zero crystallite size. The nucleation free energy barrier height is then simply the highest point on the free energy profile.

The umbrella sampling simulations were each initiated by placing a roughly spherical rhcp crystallite of a desired size in an equilibrated colloidal fluid at a volume fraction of 10%. This was carried out by first equilibrating the bulk fluid and then removing particles from a spherical region and replacing them with the crystallite. The size of the crystallite was estimated using an approach based on the Steinhardt bond-orientational parameter (139-141). The first step of this approach is to generate a list of nearest neighbors for each particle in the system. For this purpose, a pair of particles are considered neighbors if they are within 1.1 times their equilibrium (rhcp) separation distance. For each particle we calculate the term

$$q_{6m}(i) = \frac{1}{N_b(i)} \sum_{j=1}^{N_b(i)} Y_{6m}(\hat{\mathbf{r}}_{ij}), \tag{4.10}$$

for values of m ranging from -6 to 6, where the summation is performed over the $N_b(i)$ neighbors of particle i, $Y_{6m}(\hat{\mathbf{r}}_{ij})$ is a spherical harmonic and $\hat{\mathbf{r}}_{ij}$ is the normalized center to center vector between particles i and j. Once $q_{6m}(i)$ has been calculated, we consider every pair of neighbor particles and evaluate the expression

$$\mathbf{q}_6(i) \cdot \mathbf{q}_6(j) = \sum_{m=-6}^{6} q_{6m}(i) \cdot q_{6m}^*(j), \tag{4.11}$$

where $q_{6m}^*(j)$ is the complex conjugate of $q_{6m}(j)$. If the value of $\mathbf{q}_6(i) \cdot \mathbf{q}_6(j)$ is found to be greater than 0.5 for a pair of neighbor particles, they are considered connected. If any particle is connected to more than four neighbors it is considered to be crystalline. If two connected particles are found to be crystalline, they are considered members of the same cluster. Following this rule allows for all clusters in a system to be distinctly identified.

Simulations were executed by generating sequences of 1000 MMC sweeps over all particles using the usual Metropolis criterion to accept and reject each particle displacement attempt (142). Each 1000-sweep sequence was then accepted or rejected according to an additional Metropolis test based on the change in the bias potential, ΔU_B across the trajectory. A simulation was terminated once the average crystallite size, $\langle n \rangle_B$, was converged (typically ~10^6 sweeps).

In addition to the calculation of nucleation free energy barriers, direct simulations of colloidal crystallite nucleation and growth also were carried out with either Brownian dynamics (BD) simulations or NVT-ensemble Metropolis Monte Carlo (MMC). In each of these simulations a periodic system of 2000 particles at a volume fraction of 10% was first equilibrated in the fluid phase by artificially lowering the interaction strength. The interaction strength and heterogeneity were then increased to the desired levels and the system allowed to evolve without constraint until crystallization was observed or a certain amount of time had elapsed. The appropriate use of MMC for non-equilibrium growth simulations has been discussed in detail in previous work (68, 143), where the equivalence of BD and MMC for generating overdamped Langevin dynamics trajectories has been demonstrated.

4.3 Results

The nucleation free energy barriers, $\Delta G_{\max}$, for several average binding energies, $3.0 \le \langle \beta U \rangle \le 4.0$, as a function of interaction heterogeneity, *p*, are shown in Figure 4.1(a). Note that the quantity, $\langle \beta U \rangle$, here refers to the average value of the maximum attractive energy (scaled by $k_B T$), or potential 'well-depth', between a pair of particles. The free energy barriers represent the peaks of the nucleation free energy curves that were computed with umbrella sampling across a range of crystallite sizes—examples of these curves are shown in Figure 4.1(b). The impact of interaction heterogeneity on the nucleation barrier is profound, particularly for weak average binding. For binding energy $\langle \beta U \rangle = 3.2$ (blue), the addition of just 15% heterogeneity (*p* = 0.15) causes the barrier to drop from 75 $k_B T$ (no heterogeneity) to only 5 $k_B T$! For a

slightly weaker binding energy, $\langle \beta U \rangle = 3.0$, the barrier for the heterogeneity-free system is effectively infinite because the fluid phase is the ground state—again, for p = 0.15, the barrier drops below 10 $k_B T$. For typical diffusion coefficients exhibited by micron-scale particles in water, these differences imply that a uniform system with average binding strength in the range $3.0 \leq \langle \beta U \rangle \leq 3.2$ would not be expected to exhibit any crystallization, while the heterogeneous ones would crystallize rapidly in minutes to hours. Unsurprisingly, the impact of heterogeneity is more limited for higher binding strengths where the nucleation barrier is already small.

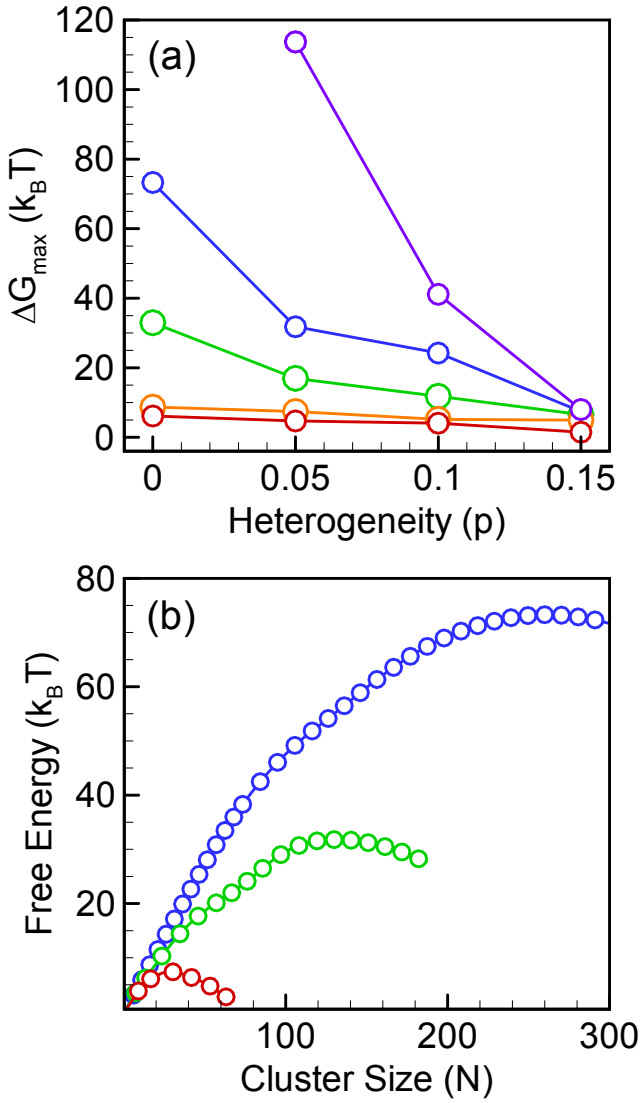

Figure 4.1: Interaction heterogeneity reduces nucleation barrier height and critical nucleus size, particularly at weaker average binding. (a) Barrier height as a function of heterogeneity: purple – $\langle \beta U \rangle = 3.0$, blue – $\langle \beta U \rangle = 3.2$, green – $\langle \beta U \rangle = 3.4$, orange – $\langle \beta U \rangle = 3.8$, red – $\langle \beta U \rangle = 4.0$. (b) Free energy profiles as a function of cluster size for $\langle \beta U \rangle = 3.2$: blue – $p = 0$, green – $p = 0.05$, red – $p = 0.10$.

The origin of this nucleation facilitation can be understood qualitatively as being due to particle fractionation: the subset of the most strongly interacting particles reduce the overall nucleation barrier by assembling into nuclei that are more stable than ones formed from 'average' particles, and which subsequently seed the growth of clusters from weaker binding particles. Evidence for this mechanism is provided in Figure 4.2, which shows the radial distribution of normalized binding energies in clusters that were spontaneously nucleated at three combinations of average binding strength and population heterogeneity. At low average binding energy and high heterogeneity (blue, $\langle \beta U \rangle = 3.0$, $p = 0.39$), the binding energy at the cluster cores is significantly higher than the mean value, decreasing rapidly towards the mean with increasing radius. As the average binding strength increases, the impact of heterogeneity becomes less important because larger fractions of the population participate in spontaneous nucleation events, resulting in more uniform spatial distributions of binding energy in each cluster—no measurable fractionation is observed for $\langle \beta U \rangle = 5.4$, $p = 0.05$ (black). The insets in Figure 4.2 show examples of mid-plane slices through crystallites at each of the three conditions, with the binding strength of each particle indicated by the sphere color.

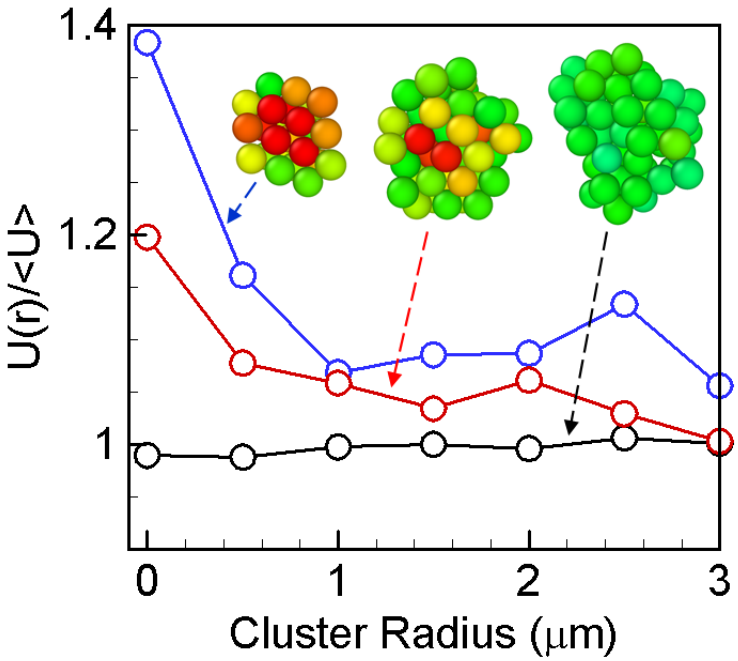

Figure 4.2: Radial fractionation of binding strengths in clusters: blue – $\langle \beta U \rangle = 3.0$, $p = 0.39$, red – $\langle \beta U \rangle = 3.4$, $p = 0.25$, and black – $\langle \beta U \rangle = 5.5$, $p = 0.05$. Insets: mid-plane slices through crystallites showing binding strength distribution; green is the mean value (b = 1), yellow/red is higher, cyan/blue is lower.

The effect of population heterogeneity on nucleation barrier height, and therefore the nucleation rate, of colloidal crystals may be significant but is not obviously of practical importance—increases in the nucleation rate also may be readily achieved by simply increasing the average binding energy. Closer inspection, however, reveals a further mechanism by which population heterogeneity facilitates practical crystal growth: by inhibiting competing processes that lead to less ordered assemblies. A large number of direct, non-equilibrium crystallization simulations at various combinations of

population heterogeneity and average binding strength were performed using the protocol described above. In each simulation, the crystallite size distribution was monitored in time and the maximum crystallite number density recorded. Only crystallites larger than 10 particles were used in the count, although the results were insensitive to this threshold in the range 3-15. Examples of the temporal evolution of the crystallite number density are shown in Figure 4.3(a) for three situations. In the first case (black diamonds, $\langle \beta U \rangle = 5$, $p = 0$), the nucleation rate is slow and only a few large crystallites are able to grow. By contrast, the high nucleation rate case (green squares, $\langle \beta U \rangle = 5.4$, $p = 0$) shows a large number of crystallites forming rapidly, followed by a decrease in the count due to crystallite coalescence. Finally, an intermediate case is shown in which the nucleation rate is increased by the presence of a small amount of heterogeneity (blue circles, $\langle \beta U \rangle = 4.8$, $p = 0.05$).

Samples of the final particle configurations (typically after about 10^6 MMC sweeps) for various cases are shown in Figure 4.3(b)-(g). The top row exhibits configurations that result without interaction heterogeneity across a binding energy interval $4.8 \le \langle \beta U \rangle \le 5.8$, in which the system transitions sensitively from exhibiting no nucleation, to showing a few isolated, highly crystalline clusters, to gelation in which a connected network of elongated clusters is formed across the entire domain. The latter configuration is very reminiscent of the gelled states observed experimentally by Lu et al. (125) in a depletion-driven micron-scale system. The remarkable impact of population heterogeneity is demonstrated in the bottom row, which shows configurations that result with $p = 0.15$ over an average binding energy interval $3.6 \le \langle \beta U \rangle \le 4.6$. Two features in

particular may be noted. First, the relevant binding energy has been shifted to lower mean values. Second, and much more significantly, the configurations now exhibit a gradual increase in the nucleation rate—remaining crystalline and exhibiting a collection of isolated, nearly spherical crystallites across the binding energy interval.

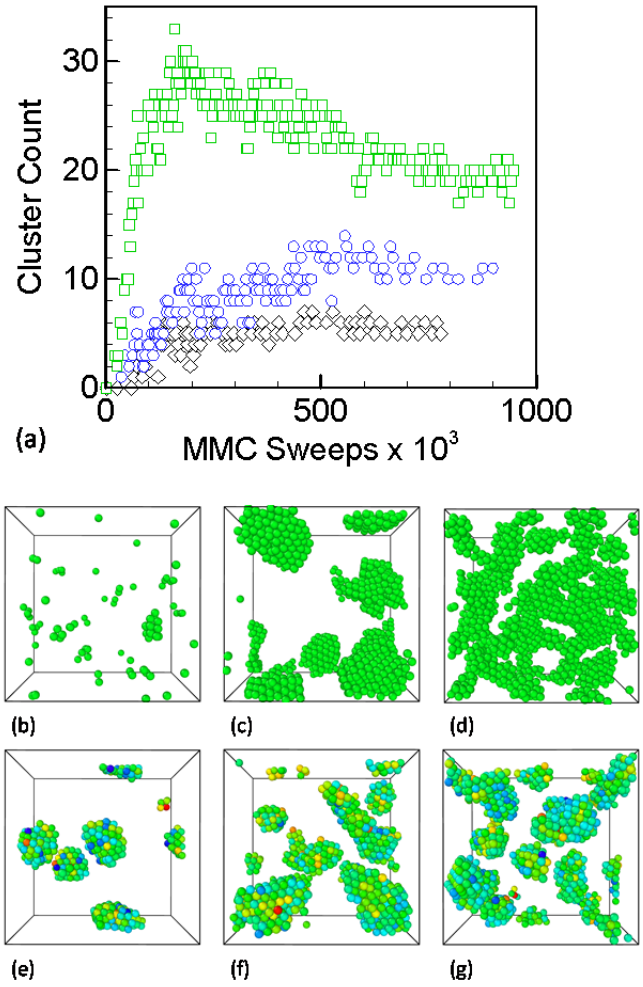

Figure 4.3: Interaction heterogeneity strongly influences the dynamical evolution and final configurations of colloidal crystallites by lowering and widening the crystallization window. (a) Evolution of the crystallite count for different combinations of average

binding strength and population heterogeneity: black diamonds – $\langle \beta U \rangle = 5$, $p = 0$; blue circles – $\langle \beta U \rangle = 4.8$, $p = 0.05$; green squares – $\langle \beta U \rangle = 5.4$, $p = 0$. (b-g) Final configurations as a function of interaction strength for p = 0 [top row, $\langle \beta U \rangle =$ 4.8 (b), 5.2 (c), and 5.8 (d)] and p = 0.15 [bottom row, $\langle \beta U \rangle =$ 3.6 (e), 4.0 (f), and 4.6 (g)]. Particle color represents binding strength: green is the mean value, red is higher, blue is lower.

These observations are summarized into a more comprehensive view in Figure 4.4, which shows a field map of the maximum cluster number density (ϕ, reported in units of clusters per cm^3) as a function of average binding strength and population heterogeneity. The crystallite number density is used here as a proxy for distinguishing between crystallization and gelation outcomes. The blue region in the lower left ($\phi < 2 \times 10^8$ cm^{-3}) corresponds to situations in which no crystallites are observed over the length of our simulations, while the white region in the upper right of the figure ($\phi > 2.5 \times 10^9$ cm^{-3}) generally corresponds to gelation outcomes with large numbers of aggregates forming a connected and arrested network; see Ref. (125). In between these limits exists a bounded region that, roughly speaking, is the target zone for practical crystallization. Superposed on the color field are isolines of nucleation barrier that are broadly aligned with the overall morphological outcome: the nucleation barriers increase as the plot is traversed diagonally from top-right to bottom-left. The impact of population heterogeneity now becomes clearly visible—it widens the crystallization window (denoted by the solid horizontal lines for p = 0.15 and p = 0) to include lower nucleation

barriers that in a heterogeneity-free system would have led to gelation. Moreover, since the strength of DNA interactions is typically an exponential function of temperature, the translation of the crystallization window to weaker interactions means the temperature window for crystallization shows an even greater widening than indicated here. The reasons for this stabilization effect may be attributed to the 'buffering' action of interaction heterogeneity—strong binders that locally drive nucleation of crystallites are dispersed among weaker binders that interfere with the onset of the system-wide spinodal decomposition associated with gelation that was described in Ref. (125).

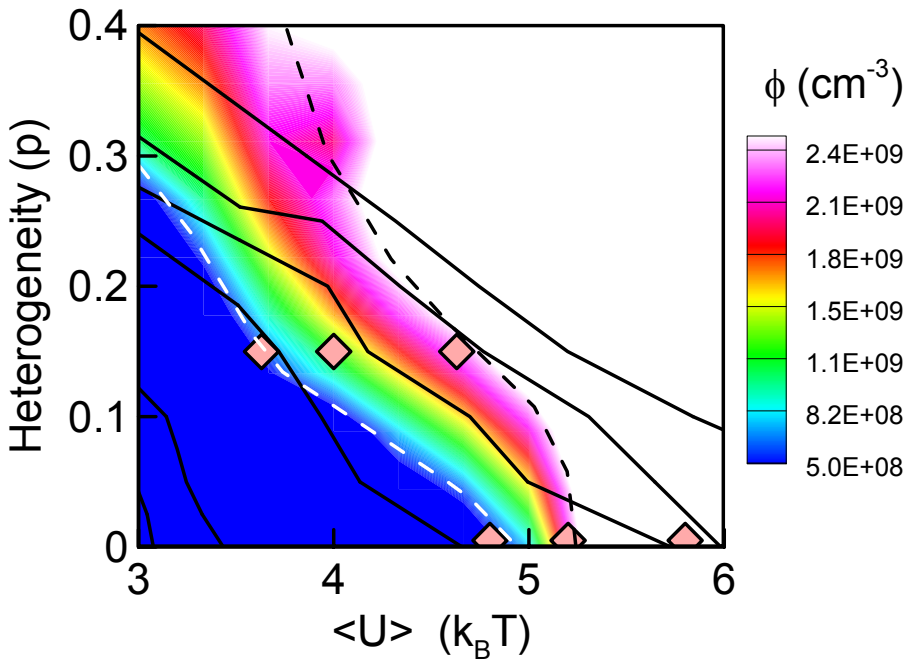

Figure 4.4: Interaction heterogeneity lowers and widens the window for crystallization. Color field denotes the maximum cluster number density, ϕ, as a function of average binding strength and heterogeneity. Thin lines represent isolines of nucleation barrier height, $\beta\Delta G_{\max}$, with values (upper left to lower right): 1, 2, 3, 5, 30, and 90 $k_B T$. Dashed

lines schematically denote crystallization window. Diamond symbols show locations of corresponding to the configurations snapshots shown in Figure 4.3.

Finally, we emphasize that our findings are not specific to DNA-mediated interactions. In fact, it is worth noting that the coarse-grained potential we employed in this work does not explicitly resolve individual DNA strand hybridization events and therefore does not capture the kinetics of particle-on-particle rolling or sliding. Depending on the nature of the DNA strand design, the thermal annealing program, and the particle size, rolling and sliding may become limiting factors for structural relaxation of a metastable, disordered aggregate into its ground-state, crystalline configuration (127). This pathway to system-wide disorder is distinct from the gelation process considered here and in Ref. (125) (which is driven by depletion-mediated entropic forces). That said, for suitably high DNA strand densities on micron-scale particles, kinetic limitations to rolling and sliding are not generally relevant, i.e., the timescale for DNA binding and unbinding is fast relative to the translational diffusivity of the particle (96). It is less clear what would cause interaction heterogeneity in depletion systems (132-135) but one possibility would be slight zeta-potential variations between different particles altering the excluded volume associated with charged depletant species.

4.4 Conclusions

In summary, our results suggest a facile avenue for optimizing crystallization behavior in systems where the interactions may be tuned across a population of particles, such as the DNA-driven one we consider here. This pathway for engineering

crystallization is likely to be particularly useful for micron-scale particles, where the crystallization window is intrinsically narrow unless other design routes are taken to increase it (49, 70, 120, 129, 130). Going forward, one may imagine that the normal distribution of binding energies we considered here, which was motivated by the emergent heterogeneity in experimental systems, could be simplified into an easily realized mixture of two or more populations having discrete and different binding strengths. With such an approach, designed heterogeneity could become a powerful tunable property for optimization of an assembling system.

5. EXTRACTING POTENTIALS FROM PARTICLE TRAJECTORIES

5.1 Introduction

The ensemble of trajectories for a system of interacting particles contains, at least in principle, detailed information about particle-particle, particle-boundary, and particle-external field interactions. Extracting *useful* information from this very high dimensional dataset – three times the number of particles in the most general case – is a fundamental 'big-data' challenge. The forward problem, which comprises the mapping of high-dimensional particle trajectories onto macroscopically meaningful, low-dimensional properties such as diffusion coefficients, density distribution functions, or thermodynamic properties, is well established within the realm of statistical mechanics. In this case, a suitable average over a portion of the degrees-of-freedom directly produces the desired property. While some quantities are more difficult to compute, e.g., free energies, the procedure is nonetheless quite straightforward.

By contrast, the inverse problem associated with determining the inter-particle interaction potential of a given system from measures of its structural and thermodynamic properties is far more challenging (144-147). For atomic and molecular systems, the canonical approach is to postulate a functional form for the potential based on an understanding of the interaction physics and then apply a database of properties (e.g., cluster energies, cohesive energies, elastic constants, phase stability ordering, defect energies, etc.), obtained by experimental measurements and/or electronic structure calculations (145, 148-152), to fit multiple adjustable parameters. The potential may be expressed analytically in closed-form based on some physical arguments (150, 153), or by sets of interpolating functions or tables (154-156), or some combination of

both. This overall strategy for atomic/molecular potential development has led to the development of a vast array of highly successful empirical and semi-empirical potentials for an immense number of material systems.

For disordered atomic systems like vapors, liquids, and glasses, the ability to measure experimentally, e.g., with x-ray or neutron diffraction, the structure factor, *S(q)*, and therefore its real-space equivalent, the pair distribution function, offers a more 'direct' approach for potential construction (157-161). In this regard, a large number of methods have been proposed to iteratively compute an interaction (usually pairwise) potential by comparing a simulated pair distribution function to the target one. Many variations on this general theme have been proposed, which differ in the initially assumed form of the potential, the nature of additional information input in the form of constraints, and the particular details of the iterative strategy used to converge to a final pair potential (144, 162-164). Overall, these approaches have been successful in generating pair potentials that reproduce both structural and thermodynamic measures of the target system. However, they also are generally quite computationally demanding because the pair distribution function, by its very nature, requires extensive configurational sampling, and therefore long simulations, to determine accurately as the trial potential is being refined. Moreover, uncertainties in the input pair distribution function also pose a problem as good potential extraction requires that the target pair distribution function be known well across the interaction range (161, 165). It should also be noted that the satisfactory (implicit) capture of many-body interactions with effective pair-potentials generated from pair distributions is far from guaranteed, and in any case requires input that may be difficult to obtain experimentally or by other means.

At the colloidal scale, inter-particle interactions have classically been inferred from experiments on analogous macroscopic surfaces in a surface force apparatus (166). More recently, the interactions of multi-micron sized particles (with each other or with flat walls) have been measured directly using an AFM cantilever (167), or using thermal fluctuations with total internal reflection microscopy (TIRM) (168-172). Colloidal interactions also can be inferred from optical tracking of pairs of micron-sized particles in optical tweezers (173); specifically from their equilibrium separation distributions in line optical tweezers (174-178) or from their non-equilibrium motion in blinking optical tweezers (179, 180). These methods come with technical challenges: the AFM or optical instrumentation required to make these measurements is often rather complex compared to a simple imaging system, many interesting particles have sizes, shapes or compositions that are not amenable to optical manipulation or have interactions that are too strong or weak to be readily measured with one or more of the above methods. Finally, analogous to the methods for disordered atomic systems, colloidal interactions also may be inferred from equilibrium distributions of ensembles of particles (181-183). However, these approaches are limited to thermal energy scale potentials, require careful treatment of liquid structure effects, and exhibit demanding constraints on statistical sampling.

Following this long line of methodological developments, here we describe a new approach for extracting interaction potentials from particle trajectory data alone (184). In essence, particle trajectories are used to compute numerical estimates of positional derivatives, i.e., velocities and/or accelerations, which are then used to infer forces as a function of inter-particle separation. The method does not place a constraint on the

number of interacting particles being observed, nor on whether the trajectories represent equilibrium or non-equilibrium conditions, and only requires that the particle positions be recorded as a function of time with sufficient fidelity. As we will demonstrate throughout this chapter, the current approach is flexible enough to enable the consideration of various dynamical situations, as long as some information regarding the nature of the dynamics is available.

The approach described here shares some important aspects with, and differs in key ways from, the force-matching (FM) technique or iginally proposed by Ercolessi and Adams (185) for the parametrization of empirical potentials using *ab initio* data, and later generalized into a powerful coarse-graining framework by Voth and coworkers (186-188) and others (189-192). Essentially, both the present approach and the numerous FM variants seek to fit a pairwise force field using information obtained from some reference system. However, while the FM technique uses forces computed from configurations obtained from simulations performed with a reference (known) force-field to fit a simpler one, the present approach numerically estimates forces from trajectories of particles that are subject to some *unknown* interparticle interaction force-field. Moreover, here we consider the possibility that the particle trajectories used to approximate forces maybe additionally be impacted by thermal fluctuations, measurement uncertainty, and hydrodynamic effects.

The remainder of this chapter is structured as follows. The general methodological details are presented in Section 5.2. In Section 5.3, we first consider the case of noiseless trajectories in both the fully inertial and overdamped limits. In Section 5.4, the impact of noise on particle trajectories is considered. We first discuss noise

produced by thermal fluctuations (5.4.A) and then consider noise introduced by positional measurement uncertainty (5.4.B). In Section 5.5, we address the impact of hydrodynamic coupling between particle trajectories. Finally, conclusions are presented in Section 5.6.

5.2 Method

Consider a system of two particles, *i* and *j*, with known trajectories, interacting through a pairwise potential, $U(r_{ij})$, where r_{ij} is the particle center-to-center separation. If these particles are otherwise isolated, this pairwise interaction is entirely responsible for the net force, $f_{i,\alpha}$, that each particle, *i*, experiences along each coordinate direction, α. For this simple two-particle system, the force profile as a function of interparticle separation distance is given by

$$F(r_{ij}) = -\frac{\partial U}{\partial r_{ij}} = f_{i,\alpha}\frac{r_{ij}}{r_{i,\alpha} - r_{j,\alpha}}, \tag{5.1}$$

where $F(r_{ij})$ is the force along the center-to-center direction and $r_{i,\alpha}$ is the α-coordinate of particle *i*. Repeating this calculation for many separation distances and binning $F(r_{ij})$ over discrete values of $r_{i,\alpha}$ produces an approximation to the complete force profile. As shown in eq. (5.1), the interaction potential energy function then may be generated by integrating over the discretized force profile.

Now consider a system of three or more particles, again with known trajectories, where the total force acting on each particle is attributed to multiple interactions. To

extract a pairwise force profile from such a system we first rewrite eq. (5.1) for a particle experiencing an arbitrary number of interactions, i.e.,

$$f_{i,\alpha} = \sum_{\substack{j=1 \\ j\neq i}}^{n} \frac{r_{i,\alpha} - r_{j,\alpha}}{r_{ij}} F(r_{ij}), \tag{5.2}$$

which may be restated as the system of linear equations,

$$\mathbf{f}_\alpha = \mathbf{C}_\alpha \mathbf{F}. \tag{5.3}$$

Here, $\mathbf{f}_\alpha \in \mathbb{R}^n$ represents the forces acting on all *n* particles along a single Cartesian direction α, $\mathbf{F} \in \mathbb{R}^{n(n-1)}$ is the vector of pairwise forces between each particle pair, and $\mathbf{C}_\alpha \in \mathbb{R}^{n\times n(n-1)}$ is a matrix with coefficients

$$C^{\alpha}_{i,(jk)} = \begin{cases} \dfrac{r_{i,\alpha} - r_{j,\alpha}}{r_{ij}} & k = i \\ 0 & k \neq i \end{cases}. \tag{5.4}$$

In principle, the system of equations (3) may be written and solved for $\mathbf{F}$ independently along each direction, α, or as a combined system along all 3 directions simultaneously, i.e.,

$$\mathbf{f} = \mathbf{C}\mathbf{F}. \tag{5.5}$$

However, while the number of constraints (rows in $\mathbf{C}$) increases linearly with particle count, the number of unknowns (columns) scales as the number of particle *pairs*. Consequently, eq. (5.3) is, in general, singular for *n*>3. As described in the force

matching literature (185), the problem may be recast so that the unknowns are the coefficients, g_m, of a discretized approximate function, $\tilde{F}(r_{ij})$, where

$$\tilde{F}\left(r_{ij}\right)=\sum_{m=1}^{M} g_m \phi_m\left(r_{ij}\right), \tag{5.6}$$

and $\phi_m\left(r_{ij}\right)$ are a set of *M* basis functions used to construct the approximation. The choice of basis for $\tilde{F}(r_{ij})$ has been discussed in some detail in Ref. (189). Here, we consider, for simplicity, a "square wave" basis in which the basis functions are constant over each interval between adjacent discretization points, i.e.,

$$\phi_m^{sq}(r)=1, \tag{5.7}$$

as well as a linear basis (defined on the unit interval [-1,1]),

$$\begin{aligned}\phi_{m,1}^{lin}\left(r\right)&=\frac{1}{2}\left(1-r\right)\\ \phi_{m,2}^{lin}\left(r\right)&=\frac{1}{2}\left(1+r\right)\end{aligned}. \tag{5.8}$$

Equation (2) now becomes

$$f_{i,\alpha}=\sum_{\substack{j=1\\ j\neq i}}^{n}\left[\frac{r_{i,\alpha}-r_{j,\alpha}}{r_{ij}}\sum_{m=1}^{M} g_m \phi_m\left(r_{ij}\right)\right], \tag{5.9}$$

or

$$\mathbf{f}=\mathbf{C}^{*}\mathbf{G}, \tag{5.10}$$

where $\mathbf{f} \in \mathbb{R}^{3N}$, $\mathbf{G} \in \mathbb{R}^{M}$ and $\mathbf{C}^{*} \in \mathbb{R}^{3N \times M}$. The system of equations (10) is over-constrained for *M<3N* so that **G** may be obtained using the least-squares approximation, i.e.,

$$\mathbf{G} = \left(\mathbf{C}^{*T}\mathbf{C}^{*}\right)^{-1}\mathbf{C}^{*T}\mathbf{f}\,. \tag{5.11}$$

In the case where the force vector, $\mathbf{f}$, is obtained from simulation configurations using a known interaction potential, eq. (5.11) corresponds to the well-established technique of force matching(186-192), which is usually applied to match a coarse-grained pair force model, $\tilde{F}(r_{ij})$, to forces generated by a more detailed interaction model. Here, however, we consider a fundamentally different application for eq. (5.11): *can one robustly and accurately calculate a pairwise force model from an experimentally measured set of particle trajectories subject to unknown interparticle interactions*? Consider first the general case of a system of particles that are subject to Langevin dynamics dictated by a combination of interparticle forces as well as forces due to the presence of an implicit solvent, i.e.,

$$m\ddot{\mathbf{r}} = \mathbf{f} - \frac{k_B T}{D}\dot{\mathbf{r}} + \left(\sqrt{2\gamma m k_B T}\right)\mathbf{R}\,, \tag{5.12}$$

where **r** is the time-dependent vector of particle positions, $\mathbf{f}$ represents interparticle forces, D is the single particle diffusivity, $k_B T / D$ is the damping, or friction, coefficient ($k_B T / D \equiv \gamma$) and $\mathbf{R}(t)$ is a random Brownian force modeled as a delta-correlated Gaussian process with zero mean so that $\left\langle \mathbf{R}(t) \right\rangle = 0$ and $\left\langle \mathbf{R}(t)\mathbf{R}(t') \right\rangle = \delta(t - t')$.

Assuming, for example, that the dynamics are noise-free and fully inertial, so that $\mathbf{R} = 0$ and $k_B T / D = 0$, particle forces therefore are dictated by Newton's Second Law of Motion, $\mathbf{f} = m\ddot{\mathbf{r}}$. Substitution into eq. (5.11) then gives

$$\mathbf{G} = \left(\mathbf{C}^{*T}\mathbf{C}'\right)^{-1}\mathbf{C}^{*T}\left(m\ddot{\mathbf{r}}\right), \tag{5.13}$$

in which the vector of particle accelerations, $\ddot{\mathbf{r}}$, may be estimated from three sequential snapshots of the trajectories using a second-order central difference approximation,

$$\ddot{r}_{i,\alpha}(t) \sim r_1(t)\frac{r_{i,\alpha}(t-\Delta t) - 2r_{i,\alpha}(t) + r_{i,\alpha}(t+\Delta t)}{\Delta t^2} + O\left(\Delta t^2\right) \tag{5.14}$$

where $r_{i,\alpha}(t)$ is the position of particle *i* in direction α at time *t*, and Δt is the time interval between sequential snapshots. In practice, the minimum appropriate time interval between trajectory observations is dictated by trajectory fluctuations due to measurement error and/or Brownian motion; the impact of trajectory noise is discussed in Chapter 4. Once $\ddot{\mathbf{r}}$ has been calculated, eq. (13) is solved for the pairwise force profile and interaction potential. Equation (5.11) may be similarly applied to overdamped systems where $\mathbf{R} = 0$ and $\ddot{\mathbf{r}} = 0$, so that $\mathbf{f} = \gamma\dot{\mathbf{r}}$. Once again, substitution of the equation of motion into eq. (11) gives a system of equations that may be used to extract the force and interaction potential profiles, i.e.,

$$\mathbf{G} = \left(\mathbf{C}^{*T}\mathbf{C}^{*}\right)^{-1}\mathbf{C}^{*T}\left(\gamma\dot{\mathbf{r}}\right), \tag{5.15}$$

Note that only two snapshots are required to compute the velocity, $\dot{\mathbf{r}}$ in eq. (5.15), in contrast to the three snapshots needed for calculation of the acceleration.

5.3 Noiseless Dynamics

In order to demonstrate the application of Eqs. (5.13) and (5.15) for noiseless trajectories, we consider a periodic system containing 64 Lennard-Jones (LJ) particles at reduced particle density, $\rho^* \equiv \rho\sigma^3 = 0.04$, and reduced temperature, $T^* \equiv k_B T / \varepsilon = 1$; these conditions correspond to a homogeneous fluid phase. The LJ potential function is truncated at 4.0σ, and a cubic polynomial function is used to smoothly zero the potential at 4.5σ. Newtonian and overdamped dynamics were simulated in the NVE (constant density and Energy) and NVT (constant density and Temperature) ensembles, respectively. Particle configuration snapshots were stored at $\Delta t = 0.001\sqrt{m\sigma^2/\varepsilon}$ intervals (particle mass, *m*, and the potential parameters, σ and ε, are all set to unity throughout). The impact of the time step is discussed in the context of other experimental constraints in Section 5.4.C. The pairwise force profile and associated interaction potential function were computed with eq. (5.13) for inertial dynamics and eq. (15) for overdamped dynamics with $\gamma = 1$). The basis function set was chosen to be a series of 60 square waves over the interval $0 \le r \le 4.5\sigma$, each with width 0.075σ. The profiles were smoothed by repeating the force evaluation over 500 sets of sequential snapshots, each time shifting the trajectory observations by Δt. The extracted profiles for both the inertial and overdamped cases are shown in Figure 5.1 (symbols), along with the corresponding input profiles (lines); the agreement generally is excellent across the range of the interaction.

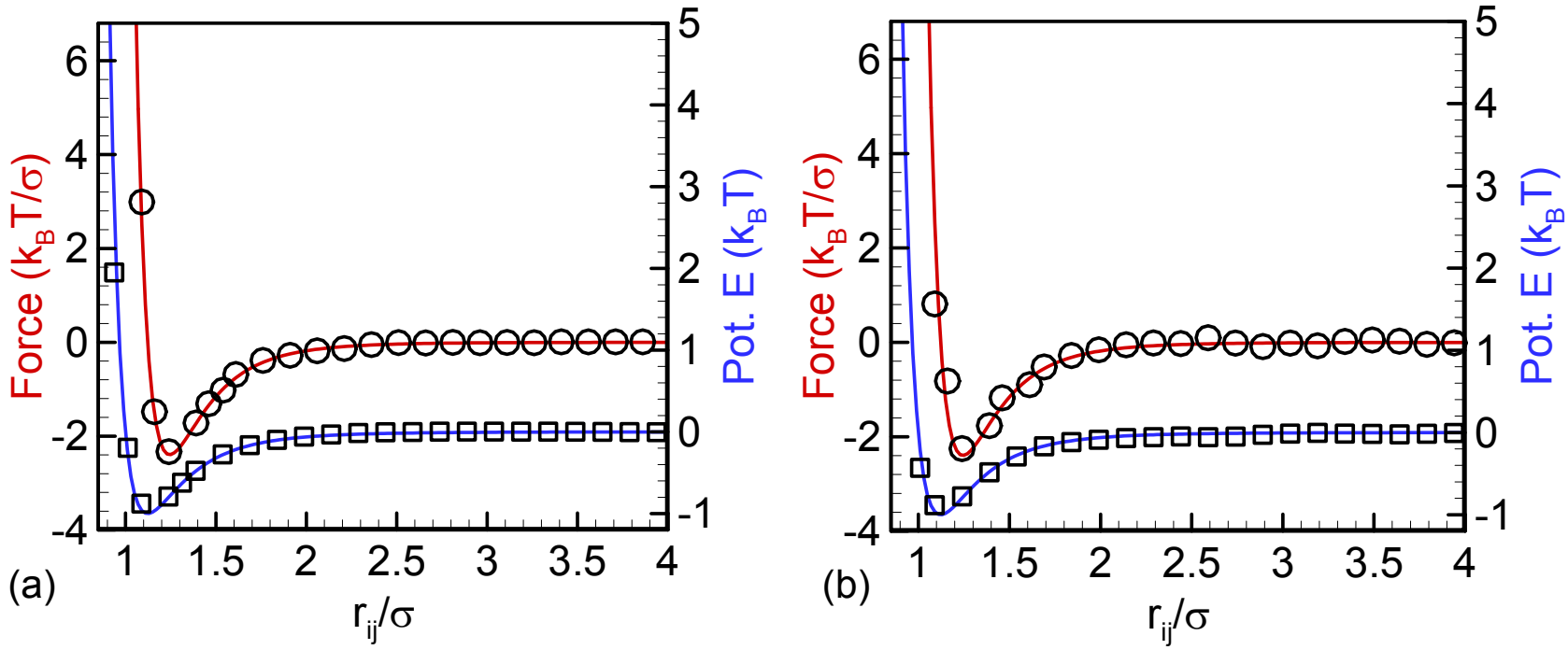

Figure 5.1: Pair interaction potentials (blue lines and squares) and force profiles (red lines and circles) extracted from observing a system of 64 Lennard-Jones particles evolving via (a) inertial dynamics and (b) overdamped dynamics. Extracted profiles, which are generated using 60 0.075σ-width square wave basis functions, are shown by symbols; input profiles are denoted by the solid lines. 500 force evaluations were used to construct the profiles in each case.

The *numerical* error associated with extracting a force profile from a noiseless trajectory (i.e., without Brownian fluctuations or any measurement uncertainties) is dependent on two primary factors: (1) the type and number of basis functions used to discretize the force profile, and (2) the number of force evaluations over which the extracted force profile is averaged. The latter factor is relevant because as the number of samples increases, the average particle pair separation sampled in each discrete interval converges to the interval center. The dependence of the numerical error in the force profile as a function of these factors is shown in Figure 5.2. As expected, the error decreases as the number of force evaluations increases. However, as with any spatial discretization technique, the minimum (systematic) error achieved depends on the number (and type) of basis functions used. Indeed, as the number of intervals is increased from 5 to 60, the residual numerical error decreases from ~1 to 0.03. Also shown in Figure 5.2, given an identical number of basis functions and force evaluations, the linear basis set always produces a more accurate force profile then the square wave basis set. Importantly, the linear basis set error also converges to its minimum value with approximately an order-of-magnitude fewer force evaluations than the square wave case. Interestingly, the number of particles considered in the system does not appear to significantly impact the statistical quality of the extracted profiles, presumably because additional particles (beyond the 64 considered here) do not sample distinct configurations. We emphasize again that the errors shown in Figure 5.2 are intrinsic to the numerical procedure used to extract the force profile from exact, noiseless particle

trajectories; additional errors due to experimental measurement uncertainties and thermal trajectory fluctuations are addressed in detail below.

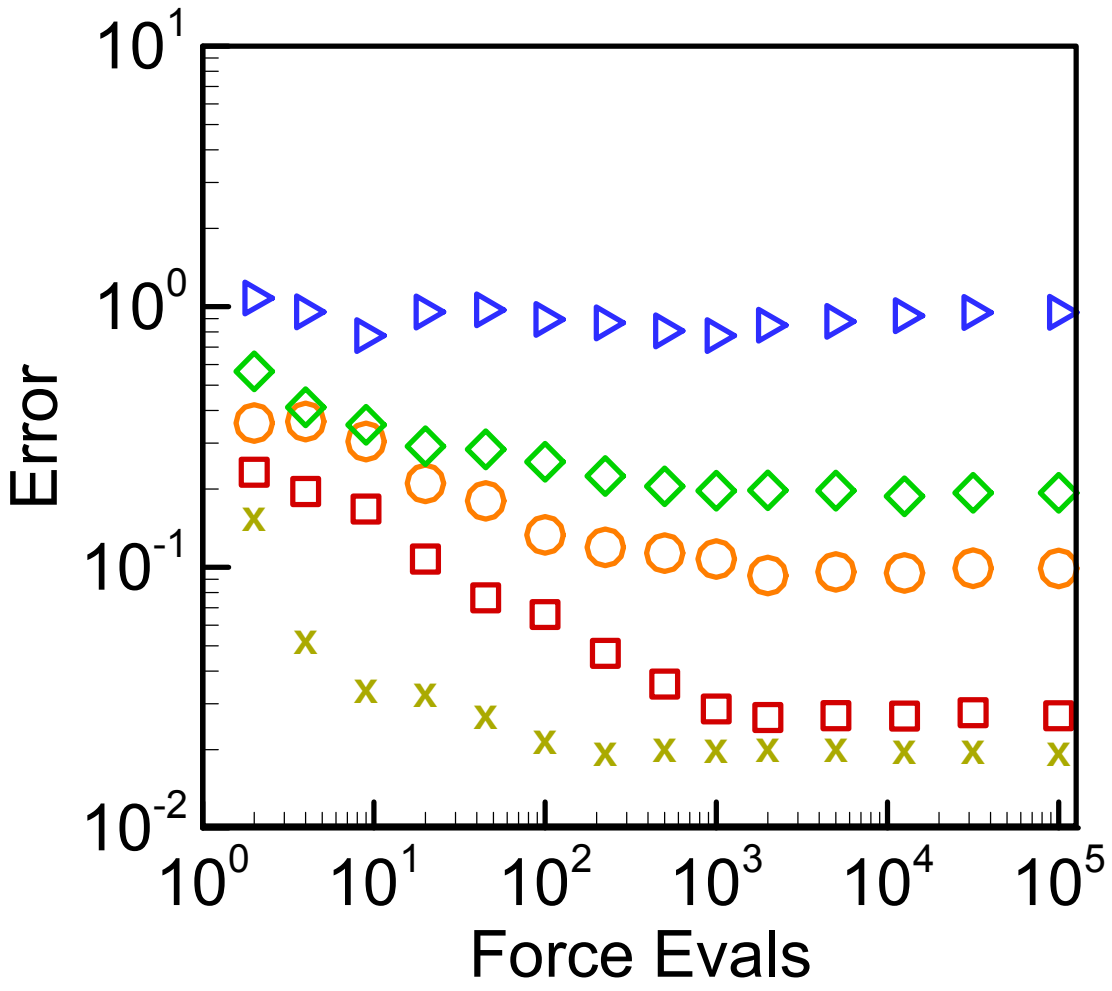

Figure 5.2: Error as a function of total trajectory data points for a system of 64 Lennard-Jones particles evolving via inertial dynamics. Error is calculated as $\left\|\mathbf{F}^{*}-\mathbf{F}\right\|_{2}/\sqrt{M}$, where $\mathbf{F}^{*}$ contains the force calculated from eq. (5.13) at the midpoint of each basis function, $\mathbf{F}$ is the actual force at each of these points, and *M* is the number of comparison points (bins). Error is computed over the range $1.2\sigma \le r \le 4.5\sigma$, which is sampled by all trajectories. Four square wave discretization levels were considered: 60 basis functions (red squares), 20 basis functions (orange circles), 10 basis functions

(green diamonds) and 5 basis functions (blue triangles) over the interval $0 \le r \le 4.5\sigma$. Also shown is the error for the 60 line-segment basis function set (gold crosses).

5.4 Trajectory Noise

5.4.A. Thermal Fluctuations

In many cases (e.g., nanoparticles in solution), particle trajectories are subject to solvent-induced thermal fluctuations. Returning to the Langevin equation [eq. (5.12)], we now consider the same system used to generate the dynamics for Figure 5.1, but with non-zero Brownian fluctuations and with friction coefficient $\gamma = 1$, so that the governing Brownian dynamics are given by $\mathbf{f} = \gamma \dot{\mathbf{r}} - \mathbf{R}$. Shown in Figure 5.3 are the force profile and potential function extracted from a set of BD trajectory data. The quality of agreement between the input and output force and interaction potentials is very similar to what is seen in the noiseless overdamped case. Note that we do not consider here the case of correlated Brownian fluctuations (i.e., Stokesian dynamics(109)), where systematic impacts on the extracted profiles may be present. The inset of Figure 5.3 shows the (subtractive) difference in the error between the noiseless, overdamped and the BD cases, which represents the scatter in the extracted profiles due entirely to the thermal fluctuations in the particle trajectories. For small force evaluation counts (<50), the presence of thermal fluctuations in the trajectories does lead to higher statistical errors, but the same residual (numerical) error as in the noiseless case can be achieved once $O(10^2)$ force evaluations are used. Further discussion of the errors associated with

thermal fluctuations is provided along with the discussion of measurement uncertainties in the following sections.

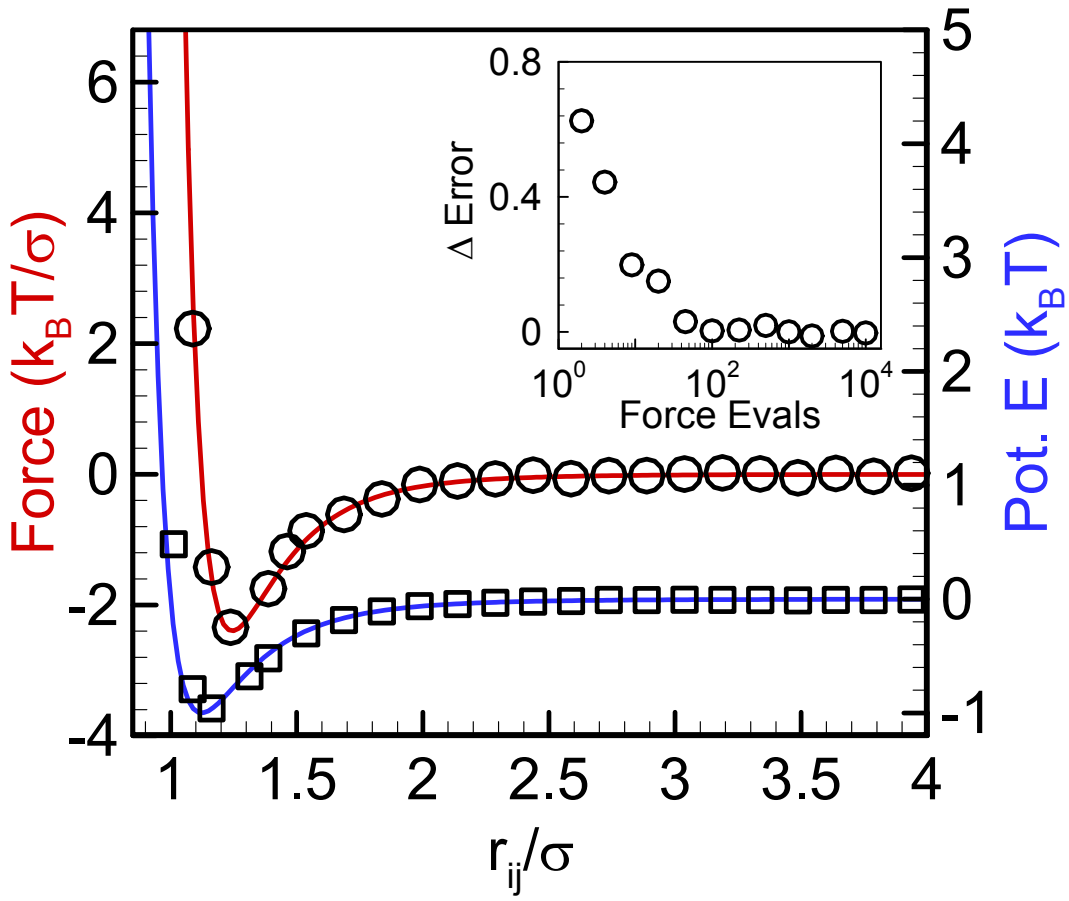

Figure 5.3: Potential function (blue line and squares) and force profile (red line and circles) extracted from a system of 64 Lennard-Jones particles evolving via Brownian dynamics. Extracted profiles, which are generated using 60 0.075σ-wide square wave basis functions, are shown by symbols; input profiles are denoted by solid lines. 500 force evaluations were used to construct the profiles. Inset: Error difference in the force profiles extracted from overdamped (fluctuation free) and Brownian dynamics trajectories.

5.4.B. Measurement Uncertainty

The practical application of the present method to experimental observations of particle trajectories in a wide variety of settings depends crucially on its robustness with respect to measurement uncertainty. The difference between measurement uncertainty and thermal fluctuations is qualitatively apparent by considering that thermal fluctuations act cumulatively over time to progressively alter particle trajectories, while measurement uncertainty is reset every snapshot. Here, we consider a situation in which each snapshot of particle positions is subjected to artificial 'measurement uncertainty' by displacing each particle a different random vector with an average magnitude of 3%, 30%, and 150% of the average particle displacement between sequential snapshots.

Shown in Figure 5.4 are force profiles, extracted from inertial, thermal fluctuation-free dynamics trajectories (all system parameters remain as given previously) for each of the three 'measurement uncertainty' amplitudes, extracted using either 500 or 10,000 force evaluations. Two important features are apparent. First, as expected, the scatter in the extracted profiles grows as the trajectory uncertainty grows – it becomes difficult to even discern any type of force profile with 500 evaluations for the 150% uncertainty case. However, as the number of evaluations is increased to 10,000, a high-quality force profile is once again obtained.

Interestingly, as the measurement uncertainty magnitude increases, it becomes evident that the extracted force profile does not converge to the input profile and becomes increasingly distorted, exhibiting a deeper attraction well (dashed blue lines). In fact, the converged force profiles are empirically found to correspond to LJ force

profiles multiplied, or magnified, by a constant larger than unity that depends on the magnitude of trajectory uncertainty (see Figure 5.5). The source of the force profile magnification may be qualitatively understood by considering that particle forces are calculated from observed particle displacements between trajectory snapshots. When particle coordinates are perturbed randomly, which is the case for measurement error, the average distance a particle is observed to travel between snapshots increases on average. Put another way, although the random perturbation averages to zero at a given time instant, the net perturbation *across a time interval* does not. This effect causes the apparent acceleration and velocity of the particle to increase, which is in turn reflected by the magnification of the extracted force profile.

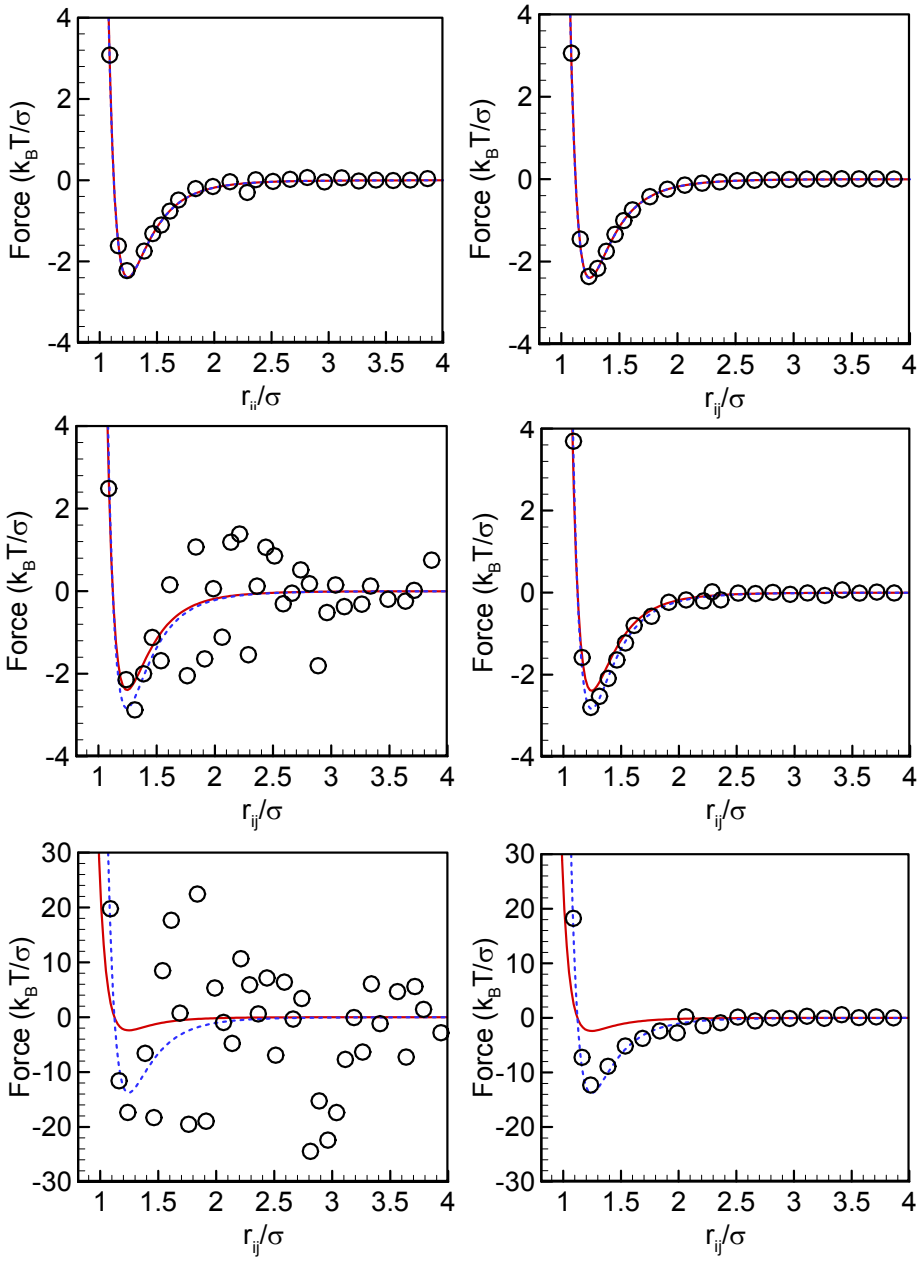

Figure 5.4: Force profiles extracted from inertial trajectories free of thermal fluctuations but subject to measurement uncertainty using 500 (left column) or 10000 (right column) force evaluations. Measurement uncertainty magnitude is 0.03 (top row), 0.3 (middle row), and 1.5 (lower row) of the mean particle displacement between two successive

observations. In each panel, the input force profile is shown as a solid red line. The dashed blue line represents the best-fit LJ force profile using a single scalar multiplier. All extracted profiles are generated using 60 square wave basis functions of width 0.075 σ.

A key question now arises: how do we extract the undistorted force profile in the (usual) situation for which the measurement uncertainty is not *a priori* known? We define μ as the multiplicative factor (>1) that the actual force profile needs to be multiplied by in order to correspond the extracted force. As shown in Figure 5.5, the reduced force magnification factor, $\mu^* \equiv \mu - 1$, scales as the square of the noise amplitude, so that

$$\mu^* = a\eta^2, \tag{5.16}$$

where η is the average effective particle displacement due to measurement error relative to mean particle displacements magnitude between sequential snapshots.

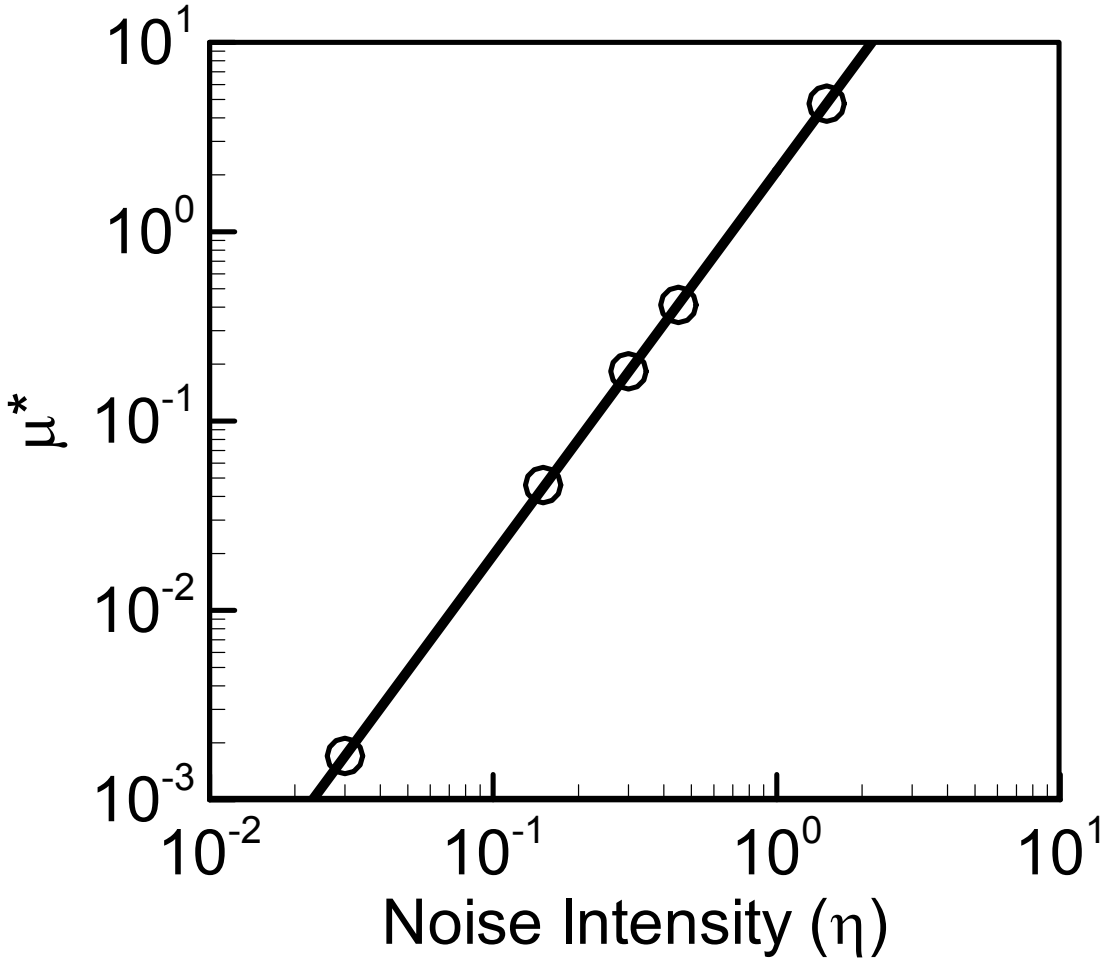

Figure 5.5: Reduced magnification factor as a function of noise intensity amplitude; black line shows quadratic fit (see text for details).

Now consider a sequence of particle positions measured at regular time intervals along some trajectory that are used to compute two force profiles – one in which the data at every interval is used and a second in which only every other observation is used, effectively doubling the time between snapshots. It then follows that η in the second case will be reduced by a factor of two, i.e., $\eta_2 = 0.5\eta_1$, assuming that the particle velocity is constant across the time step interval. The validity of this assumption is subject to constraints on the time step size (or the imaging framerate; see Section 5.4.C) and the rate of velocity change or acceleration, i.e., $a\Delta t / v = \Delta v / v << 1$. The relative magnification effect between the two extracted profiles (which is known) is then given by

$$\mu_r = \frac{\mu_2^* + 1}{\mu_1^* + 1} = \frac{1 + a\left(\eta_1/2\right)^2}{1 + a\eta_1^2}. \tag{5.17}$$

Rearranging for the reduced magnification factor for the first profile then gives

$$\mu_1^* = a\eta_1^2 = \frac{\mu_r - 1}{1/4 - \mu_r} - 1. \tag{5.18}$$

Equation (18) was tested by considering a relative noise intensity of 0.525 (corresponding to a reduced magnification factor of 0.58) applied to the inertial dynamics situation considered in Figure 5.4. Shown in Figure 5.6 are force profiles extracted with (squares) and without (circles) correcting for measurement uncertainty using eq. (5.18). It is readily apparent that the magnification correction provided by eq. (5.18) robustly accounts for the distortion, although some scatter remains in the extracted profile – this is addressed next.

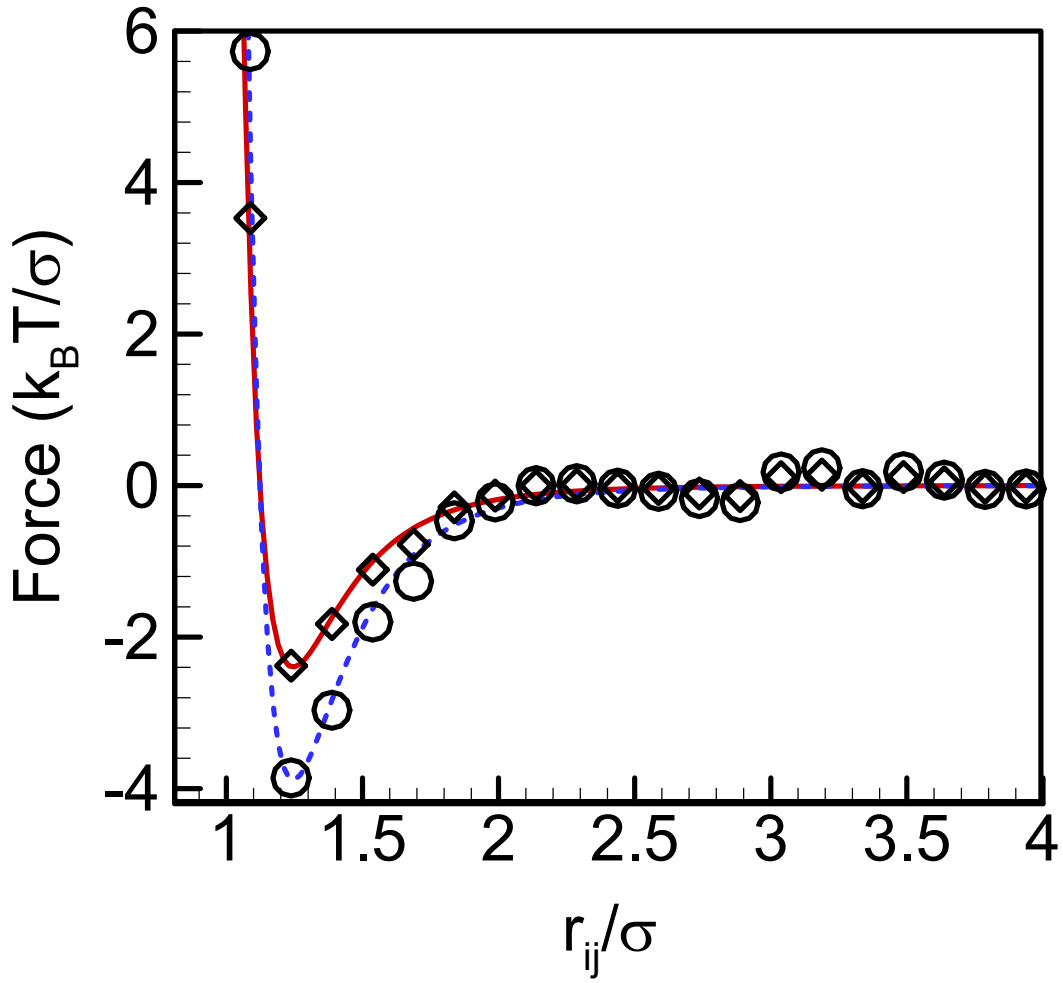

Figure 5.6: Force profiles extracted from observing a system of 64 Lennard-Jones particles evolving via inertial dynamics subject to measurement uncertainty of amplitude 0.525. Extracted profiles are shown by symbols (uncorrected force – circles, corrected force – diamonds), the input force profile is denoted by the solid red line. The dashed blue line shows the best-fit LJ force profile for the uncorrected force assuming that the input force is scaled by a single multiplier of 1.58. Both extracted profiles are generated using a set of 60 square wave basis functions of width 0.075σ.

The residual impact of measurement uncertainty on the error in the extracted force may be assessed by computing the difference in the force profile error obtained for noisy (Figure 5.4) and exact (Figure 5.1(a)) inertial dynamics trajectories. Figure 5.7 shows the subtractive error difference between these two cases as a function of evaluation count for several noise amplitudes. As in the case for thermal fluctuations (see inset of Figure 5.3), measurement uncertainty or trajectory noise leads to additional scatter in the extracted profiles that may be systematically reduced with additional force evaluations.

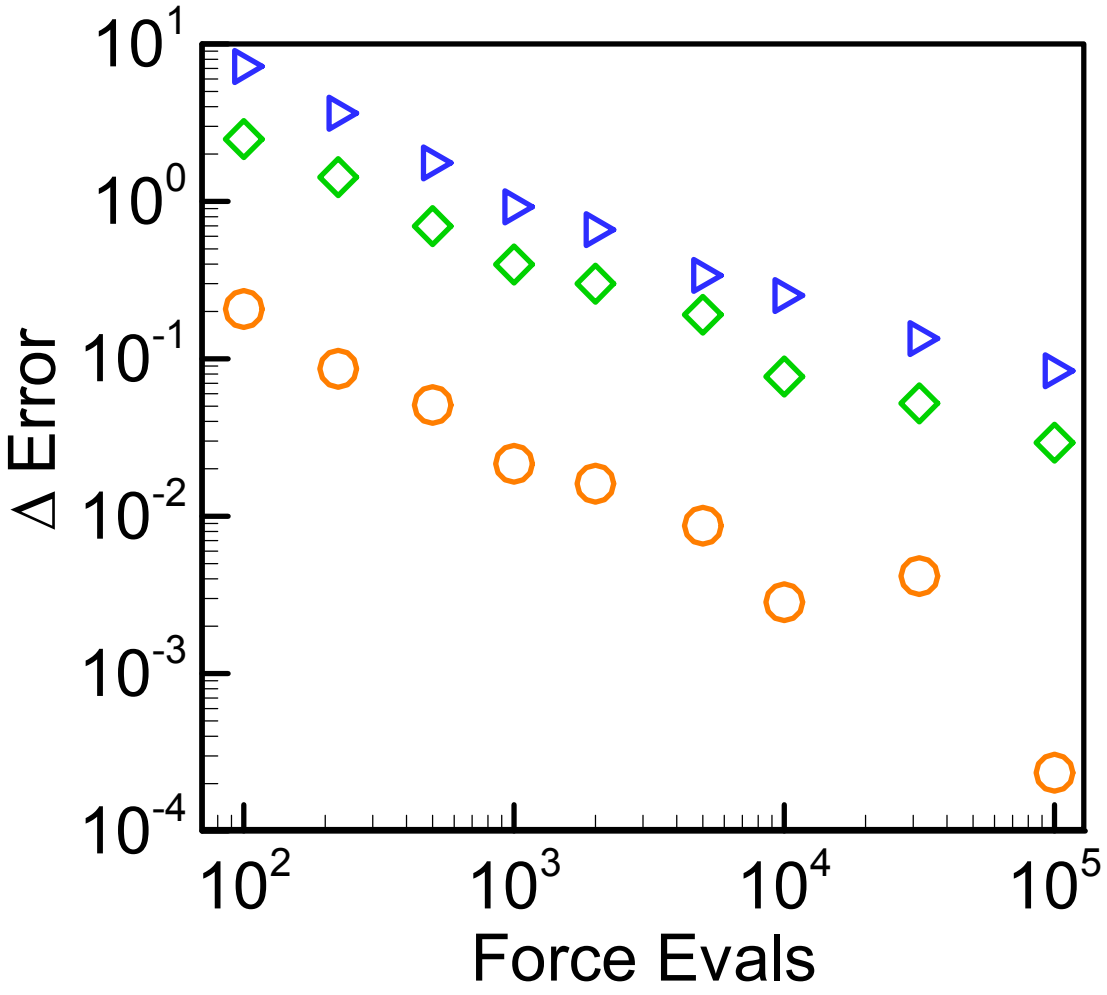

Figure 5.7: Difference in the force profile error extracted from noisy and exact inertial dynamics trajectories as a function of the force evaluation count calculated for several measurement uncertainty amplitudes (relative to average particle displacement): orange circles –described in the text (which has been corrected for using eq. (5.18)).

5.4.C. Error Analysis in the Context of Experiment

The preceding analyses demonstrate that both thermal fluctuations and trajectory measurement noise increase scatter in the extracted force profiles, but which may be reduced by increasing the number of force evaluations used to construct the profile. The impact of such scatter in the context of realistic experimental constraints is the subject of this section. We begin by considering the trajectory impact of Brownian diffusion and measurement uncertainty, relative to that of interparticle interactions (the signal). In this context, two noise-to-signal ratios may be defined,

$$\alpha \equiv \frac{\sqrt{Df}}{v}, \tag{5.19}$$

and

$$\beta \equiv \frac{e_M f}{v}, \tag{5.20}$$

where f is the framerate at which images may be recorded, e_M is the trajectory displacement due to measurement error, D is Brownian diffusivity, and v is the signal, or drift, velocity, i.e., the velocity due to interparticle interactions. Consequently, α represents the ratio of apparent diffusion velocity (over a time interval dictated by the framerate) and the drift velocity which may represent either overdamped or inertial particle dynamics. Similarly, β represents the ratio of an effective velocity due measurement uncertainty relative to the signal velocity, v.

For reference, consider a system of 1 μm beads suspended in water at 300K being video imaged at a framerate of 50 Hz. For such a system, a typical measurement

uncertainty of 0.01μm is expected (~1% of the particle size), along with a Brownian diffusivity of ~0.5 $\mu m^2/s$. Consequently, for a single force evaluation the conditions α, β <<1 require that $v>>1$ μm/s, i.e., the interparticle force must be many $k_B T$ in magnitude to be captured accurately. However, as evidenced by the convergence of the profiles in Figures 4, even if α and/or β are not small, the associated error may be systematically reduced by increasing the number of force evaluations. The 150% uncertainty case in Figure 7, for example, corresponds to α =0, β =1.5, and shows clearly that the force profile may be recovered well beyond the O(1) error expected from eq. (5.20), as long as a sufficient number of force evaluations are used. The convergence of force profiles extracted from noisy trajectories with respect to the number of evaluations is readily understood by considering Eqs. (19) and (20) – the averages of both D and e_M tend to 0 as the number of samples increases.

The expressions in Eqs. (19) and (20) suggest that α and β also may be arbitrarily reduced by simply lowering the imaging framerate. In fact, this is not the case – the distance a particle travels between sequential snapshots (either by drift or by diffusion) also must be small relative to the length scale of the potential function, L, otherwise the extracted potential will be blurred. Two additional constraints for extracting accurate force profiles may therefore be identified as

$$\gamma \equiv \frac{v}{Lf} << 1, \tag{5.21}$$

$$\delta \equiv \frac{1}{L}\sqrt{\frac{D}{f}} << 1. \tag{5.22}$$

Here, γ and δ represent ratios of the drift and diffusion distances, respectively, relative to the interparticle potential length scale, L. For v~1 μm/s, D~1 μm^2/s, and a potential function of order the particle size (1 □m), the lower bound on the framerate due to drift and diffusion is f~1 s^{-1}. However, as the potential becomes shorter ranged, this lower bound becomes more severe: for example, a DNA-mediated interaction potential is characterized by L~10 nm, necessitating a minimum framerate of ~100 s^{-1}.

The impact of framerate on the error was investigated using the exact, noiseless (inertial) trajectories considered in Figure 5.1(a). Shown in Figure 5.8 is the error, as defined in Figure 5.2, as a function of the time interval size; recall that all preceding analysis was performed with a time step, $\Delta t = 0.001\sqrt{m\sigma^2/\varepsilon}$, which corresponds to a (dimensionless) framerate of 1000. For time interval sizes less than ~0.05-0.1, the error is insensitive to the time step size and corresponds to the minimum error attainable with the discretization level and basis function choices. Above this time step size, the error increases rapidly to O(1), where the force profile details are essentially lost.

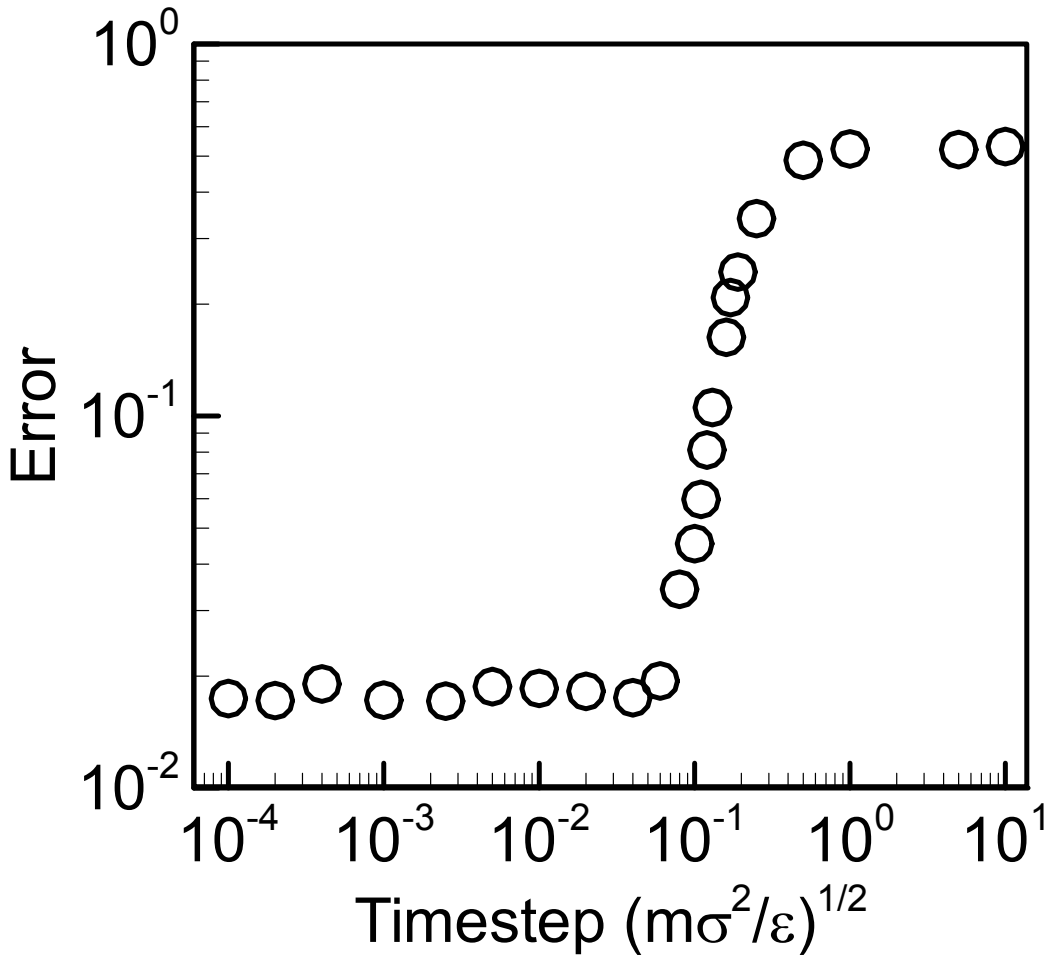

Figure 5.8: Error as a function of time step size for a system of 64 Lennard-Jones particles evolving via exact, noiseless, inertial dynamics. Extracted force profiles, are generated using 60 0.075σ-wide line segment basis functions. Error is calculated as $\left\|\mathbf{F}^{*}-\mathbf{F}\right\|_{2}/\sqrt{M}$, where $\mathbf{F}^{*}$ contains the force calculated from eq. (5.13) at the midpoint of each basis function, $\mathbf{F}$ is the actual force at each of these points, and *M* is the number of comparison points (bins).

5.5 Hydrodynamic Correlations

Colloidal particle trajectories are unavoidably measured in some liquid medium, typically water. As each particle moves through the fluid, it perturbs it and creates a flow field that in turn impacts surrounding particles' trajectories (110, 111, 193). Collectively, these hydrodynamic couplings lead to an effectively many-body interaction between the particles (or between particles and a wall), and must be accounted for if the intrinsic inter-particle interactions are to be isolated. Our aim here is not to extract a many-body interaction potential that mimics the hydrodynamic forces on each particle, although even this may be, in principle, possible. Instead, we seek to demonstrate that the hydrodynamic coupling can be effectively removed from the trajectory observations, allowing for the intrinsic pair-interaction (i.e., the LJ potential) to be recovered from the particle trajectories. Hydrodynamic correlations in incompressible fluids may be included in eq. (5.12) by replacing the single particle diffusivity, *D*, with the full mobility tensor, $\mathbf{D}$. The individual components of the mobility tensor used here are summarized in Section 6.6.

Consider an overdamped system subject to hydrodynamic correlations and with no Brownian fluctuations such that the dynamics are given by $\mathbf{f} = k_B T \mathbf{D}^{-1} \dot{\mathbf{r}}$. Substitution into eq. (5.11) then results in the following system of equations which may be solved to extract a force profile from a hydrodynamically correlated system.

$$\mathbf{G} = \left(\mathbf{C}^{*T} \mathbf{C}^{*} \right)^{-1} \mathbf{C}^{*T} \left(k_B T \mathbf{D}^{-1} \dot{\mathbf{r}} \right). \tag{5.23}$$

Note that the mobility tensor must be recalculated for every particle configuration, as it is dependent on particle coordinates. An example of a profile extracted using eq. (5.23) is

shown in Figure 5.9 for the case where the viscosity of the ambient fluid, η, is 0.07 $\sigma^2/\sqrt{\varepsilon m}$ and the particle radius is 0.45σ. These parameters were chosen such that γ is unchanged relative to the case shown in Figure 5.1(b), while introducing a sufficiently large particle radius to ensure significant hydrodynamic correlations between the particles. All other parameters were set to be the same as those used in Figure 5.1(b). As shown in Figure 5.9(a), ignoring the hydrodynamic correlations, i.e., using eq. (5.15) instead of eq. (5.23) when extracting the force profile, leads to large errors. Although not shown, these errors are configuration-dependent and in general cannot be removed once the force profile has been extracted from the particle trajectories. In Figure 5.9(b), the correct force and potential function are obtained by accounting for hydrodynamic correlations using eq. (5.23). Statistical and systematic errors are similar to the cases in which hydrodynamic correlations are not present.

It should be noted that, as formulated, our method requires the mobility tensor, $\mathbf{D}$, as input in order to separate out the influence of hydrodynamics from the intrinsic inter-particle interactions. While this is straightforward for simple, unbounded geometries, it becomes more challenging for situations in which the medium is constrained by interfaces or walls. In such cases, complementary approaches such as the methods in refs. (180, 183) may be employed to determine the relevant mobility tensor. In these studies, a Smoluchowski equation is fit to equilibrium distributions of particle-wall or particle-particle separations in order to simultaneously extract the interaction potentials and hydrodynamic mobilities.

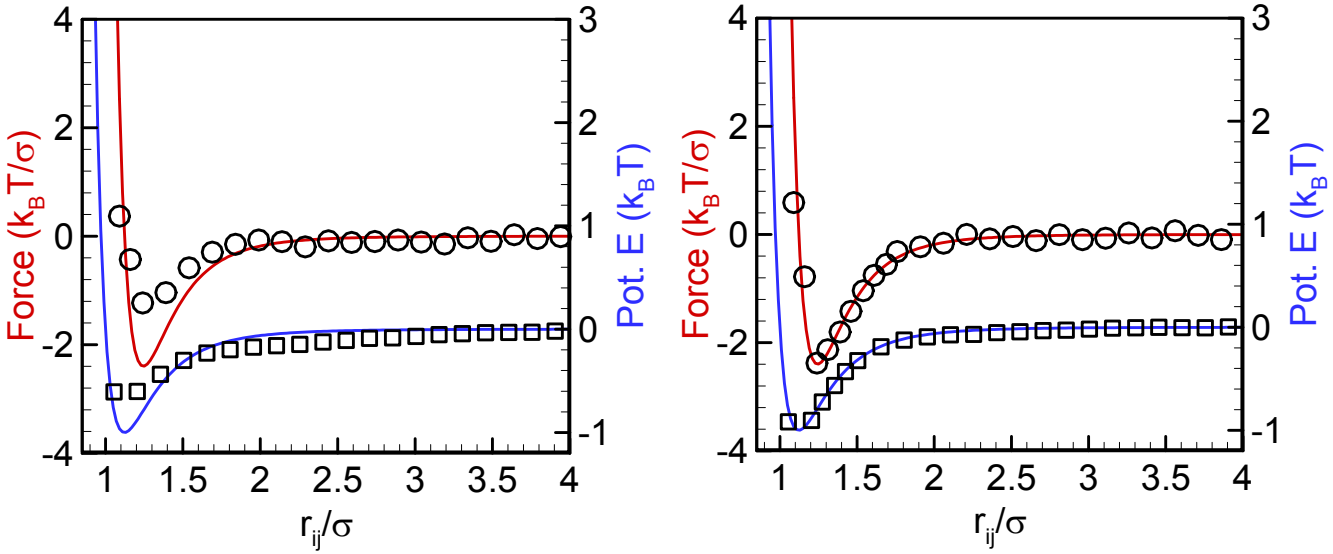

Figure 5.9: Pair potential functions and force profiles extracted from a system of 64 Lennard-Jones particles evolving via overdamped dynamics with hydrodynamic correlations. The profiles shown on the left were extracted assuming simple overdamped dynamics with no hydrodynamic correlations ($D_{i,j\neq i} = 0$). The profiles shown on the right were calculated while including hydrodynamic corrections. Extracted profiles are shown by symbols (force – circles, potential energy – squares), input profiles are denoted by solid lines. A total of 500 trajectory snapshots were used to extract the profiles. Both extracted profiles are generated using a set of 60 square wave basis functions of width 0.075σ.

5.6 Conclusions

In this chapter we have presented a computationally efficient and robust method for reliably extracting pair potential functions from arbitrary sets of multiple particle trajectories with no special constraints on particle configuration or system equilibration. We expect that this flexibility will greatly increase the scope of the systems that are amenable to interparticle interaction analysis, especially in situations where equilibration is difficult to confirm or achieve. Our approach relies on some knowledge of the equations of motion that govern the particle trajectories but otherwise places no assumptions on the nature of the (pairwise) inter-particle interactions. Importantly, the same mathematical approach can be applied to systems having different fundamental equations of motion, i.e. underdamped, overdamped, with hydrodynamic interactions, or without. It is shown to be robust with respect to particle tracking error and the presence of Brownian motion. The latter can be mitigated by simply averaging over additional uncorrelated trajectory data, while the former, which is shown to introduce systematic errors, can be eliminated using a simple procedure without any *a priori* knowledge of the tracking error.

Further developments will be required to address additional relevant situations including particle anisotropy (194), many-body interactions (175), particle polydispersity (195), and hydrodynamic effects in more general situations (180). One notable limitation with regards to hydrodynamic correlations is that our approach requires that the motion be a function only of the particle positions and its derivative—this will not be the case for particles in viscoelastic fluids, for instance. In the context of the first two issues, we note

that the method does not formally require a pairwise target potential, and can be readily generalized for use on more complex, anisotropic or multi-body potential functions, with no fundamental methodological changes necessary. That said, increasing the dimensionality of the variable space upon which the potential function is dependent (e.g. orientation for anisotropic potentials) will place increased demands on the tracking data.

6. CONCLUSIONS

6.1 A Case Study: Phase Transformations in CsCl Superlattices

We have uncovered a previously unknown source of kinetic influence on solid-solid phase transformations in colloidal systems, namely the solvent in which the particle assembly forms. While externally applied flows have been used previously to influence assembly in a variety of systems, we believe this is the first evidence for an autogenous mechanism in which self-induced hydrodynamic drag forces in an otherwise quiescent solvent lead to non-equilibrium structure selection. In particular, we provide strong evidence that hydrodynamic correlation between particles establishes a dynamic anisotropy that results in bias towards certain configurations over others during a CsCl→CuAu-I displacive transformation of binary superlattice crystallites. The extent of the anisotropy appears to be closely tied to the ratio of particle size and DNA oligomer length, possibly obfuscating otherwise simple size scaling laws. We emphasize that the outcome of this study is not simply that DLPA processing is complicated: the ability to intentionally direct DLPAs towards non-equilibrium (and useful) configurations greatly increases the versatility of these materials, provided that such effects are well understood.

Finally, while this study was focused on the specific action of anisotropic diffusion during displacive transformations of DNA-linked particle assemblies, we hypothesize that similar effects may occur in a variety of colloidal model systems. The principal defining feature of the system we consider in this chapter is structural transformation involving the cooperative motion of large numbers of colloidal particles, corresponding to the

system moving along narrow pathways on flat energy subspaces in configuration space. The same description would apply equally well to glasses and super-cooled fluids of hard-sphere colloids, which display highly cooperative rearrangements termed dynamical heterogeneity (112, 113). Moreover, our CsCl parent crystals are held together by short-range reversible interactions, in insufficient numbers to give rise mechanical rigidity, reminiscent of so-called attractive glass colloidal systems (114). Thus, we hypothesize that hydrodynamic selection/biasing can play a role in multiple systems of considerable current interest, in which the details of microscopic rearrangements often remain poorly understood and experimental results frequently do not resemble those from matched simulations.

6.2 Exploring Zero-Energy Phase Transformations in Asymmetric Binary Systems

Previous study of the CsCl superlattice assembled from DNA functionalized colloidal particles had indicated that the lattice was capable of undergoing four distinct solid-solid phase transformations: two producing CuAu-fcc, one producing CuAu-hcp and one producing rhcp. However, these studies were constrained to systems in which both like-particle binding strengths were equal, that is $U_{AA} = U_{BB}$. Upon discarding this constraint the presence of the pcp phase and its "partial" phase transformation from CsCl was revealed. While this is noteworthy by itself, the pcp lattice is also capable of transforming further, producing either CuAu-fcc or CuAu-hcp. Furthermore, the two step nature of this transformation allows the CuAu-hcp producing transformation to occur without experiencing the enhanced drag effect previously thought to prevent the formation of the CuAu-hcp lattice in experiment. As a result, this two-step transformation

pathway provides the only known mechanism for producing high quality CuAu-hcp from systems of DNA functionalized colloidal particles.

Study of CsCl crystallites constructed of particles at a size ratio of 0.85 revealed that the set of transformations available is qualitatively similar to those available at a size ratio of 1.0. The zig-zag and shear transformations still exist, but now follow slightly altered pathways and produce BIrV and HIrV, in place of CuAu-hcp and CuAU-fcc, respectively. Additionally, the pcp lattice can still be used to bypass the hydrodynamic bias against the zig-zag transformation, as seen at a size ratio of 1.0. Finally, study of the NaCl superlattice constructed from size ratio 0.565 particles reveals that phase transformations in systems of DNA functionalized colloidal particles exist outside the CsCl superlattice system. The zero-frequency mode spectrum of the NaCl superlattice can be described using (100) modelets in the same manner the CsCl superlattice can be described using (110) modelets. While the NaCl superlattice is significantly less rigid than the CsCl superlattice, it unfortunately has only been observed to undergo one transformation in experiment, a simple (110) shear of the (100) facing planes, which is easily replicated using the zero-frequency mode evolution method.

Both the prevalence and complexity of solid-solid phase transformations in crystallites constructed from DNA-Functionalized Colloidal Particles is significantly greater than previously thought. Transformations pathways previously believed to be inaccessible due to hydrodynamic biases can now be bypassed entirely by making use of a newly identified intermediate phase: pcp. Additionally, it has been determined that solid-solid phase transformations exist at both size ratios outside of 1.0 and even in lattices completely unrelated to CsCl, such as NaCl.

6.3 The Surprising Role of Interaction Heterogeneity in Colloidal Crystallization

While the particular design challenges associated with any given self-assembly route may be unique, the conventional wisdom is that particle heterogeneity of any nature is an undesirable feature. This is likely to be always true for particle size. However, our results suggest that this is not the case for inter-particle interactions: under some conditions, it may in fact be beneficial to purposefully introduce small amounts of interaction heterogeneity. The mechanism responsible for the favorable effects arises from a combination of thermodynamic and kinetic processes. At a given mean binding strength, a broader distribution of particle interaction strengths introduces a sub-population of 'strong binders' that stabilizes small, sub-critical nuclei and dramatically increases the nucleation rate (by lowering the nucleation free energy barrier). In one sense, these anomalously strongly bound nuclei may be considered as heterogeneous nucleation sites. Equally importantly, the presence of relatively weak binders serves to temper the kinetics of the overall aggregation process, providing a buffer between crystallites and preventing a system-wide gelation process.

These mechanisms are not obviously restricted to DNA-mediated interactions, or to the particular volume fraction, particle size, and heterogeneity distributions considered here. We expect qualitatively similar findings for more complex systems containing multiple particle species, although further study will be required to assess the impact of interaction heterogeneity across different systems. On the other hand, the DNA-

mediated assembly system does offer a particularly convenient route for introducing interaction heterogeneity, which is not necessarily true for other interaction sources, e.g., electrostatics or depletion. It is in fact quite likely that some amount of DNA grafting density variation across a population of particles is unavoidable, and it may very well be that this 'quality control' issue is a beneficial feature of the system.

6.4 Extracting Potentials from Particle Trajectories

We have presented a computationally efficient and robust method for reliably extracting pair potential functions from arbitrary sets of multiple particle trajectories with no special constraints on particle configuration or system equilibration. We expect that this flexibility will greatly increase the scope of the systems that are amenable to interparticle interaction analysis, especially in situations where equilibration is difficult to confirm or achieve. Our approach relies on some knowledge of the equations of motion that govern the particle trajectories but otherwise places no assumptions on the nature of the (pairwise) inter-particle interactions. Importantly, the same mathematical approach can be applied to systems having different fundamental equations of motion, i.e. underdamped, overdamped, with hydrodynamic interactions, or without. It is shown to be robust with respect to particle tracking error and the presence of Brownian motion. The latter can be mitigated by simply averaging over additional uncorrelated trajectory data, while the former, which is shown to introduce systematic errors, can be eliminated using a simple procedure without any *a priori* knowledge of the tracking error.

Further developments will be required to address additional relevant situations including particle anisotropy (194), many-body interactions (175), particle polydispersity (195), and hydrodynamic effects in more general situations (180). One notable limitation with regards to hydrodynamic correlations is that our approach requires that the motion be a function only of the particle positions and its derivative—this will not be the case for particles in viscoelastic fluids, for instance. In the context of the first two issues, we note that the method does not formally require a pairwise target potential, and can be readily generalized for use on more complex, anisotropic or multi-body potential functions, with no fundamental methodological changes necessary. That said, increasing the dimensionality of the variable space upon which the potential function is dependent (e.g. orientation for anisotropic potentials) will place increased demands on the tracking data.

BIBLIOGRAPHY

1. Reineck P*, et al.* (2012) A Solid-State Plasmonic Solar Cell via Metal Nanoparticle Self-Assembly. *Adv Mater* 24(35):4750-4755.
2. Campbell AI, Anderson VJ, van Duijneveldt JS, & Bartlett P (2005) Dynamical arrest in attractive colloids: The effect of long-range repulsion. *Phys Rev Lett* 94(20).
3. Guo PJ, Sknepnek R, & de la Cruz MO (2011) Electrostatic-Driven Ridge Formation on Nanoparticles Coated with Charged End-Group Ligands. *J Phys Chem C* 115(14):6484-6490.
4. Timonen JVI, Latikka M, Leibler L, Ras RHA, & Ikkala O (2013) Switchable Static and Dynamic Self-Assembly of Magnetic Droplets on Superhydrophobic Surfaces. *Science* 341(6143):253-257.
5. Shevchenko EV, Talapin DV, Kotov NA, O'Brien S, & Murray CB (2006) Structural diversity in binary nanoparticle superlattices. *Nature* 439(7072):55-59.
6. Shevchenko EV, Talapin DV, Murray CB, & O'Brien S (2006) Structural characterization of self-assembled multifunctional binary nanoparticle superlattices. *J Am Chem Soc* 128(11):3620-3637.
7. Henzie J, Grunwald M, Widmer-Cooper A, Geissler PL, & Yang PD (2012) Self-assembly of uniform polyhedral silver nanocrystals into densest packings and exotic superlattices. *Nat Mater* 11(2):131-137.
8. Chung BG, Lee KH, Khademhosseini A, & Lee SH (2012) Microfluidic fabrication of microengineered hydrogels and their application in tissue engineering. *Lab Chip* 12(1):45-59.
9. Jenkins IC, Casey MT, McGinley JT, Crocker JC, & Sinno T (2014) Hydrodynamics selects the pathway for displacive transformations in DNA-linked colloidal crystallites. *Proceedings of the National Academy of Sciences* 111(13):4803-4808.
10. Whitesides GM & Grzybowski B (2002) Self-assembly at all scales. *Science* 295(5564):2418-2421.
11. Shields SP, Richards VN, & Buhro WE (2010) Nucleation Control of Size and Dispersity in Aggregative Nanoparticle Growth. A Study of the Coarsening Kinetics of Thiolate-Capped Gold Nanocrystals. *Chem Mater* 22(10):3212-3225.
12. Auer S & Frenkel D (2001) Suppression of crystal nucleation in polydisperse colloids due to increase of the surface free energy. *Nature* 413(6857):711-713.
13. Cacciuto A, Auer S, & Frenkel D (2004) Onset of heterogeneous crystal nucleation in colloidal suspensions. *Nature* 428(6981):404-406.
14. Radu M & Schilling T (2014) Solvent hydrodynamics speed up crystal nucleation in suspensions of hard spheres. *Epl-Europhys Lett* 105(2).
15. Liu D, Park SH, Reif JH, & LaBean TH (2004) DNA nanotubes self-assembled from triple-crossover tiles as templates for conductive nanowires. *P Natl Acad Sci USA* 101(3):717-722.
16. Rothemund PWK*, et al.* (2004) Design and characterization of programmable DNA nanotubes. *J Am Chem Soc* 126(50):16344-16352.

17. Winfree E, Liu FR, Wenzler LA, & Seeman NC (1998) Design and self-assembly of two-dimensional DNA crystals. *Nature* 394(6693):539-544.
18. Zheng JP*, et al.* (2009) From molecular to macroscopic via the rational design of a self-assembled 3D DNA crystal. *Nature* 461(7260):74-77.
19. Ke YG, Ong LL, Shih WM, & Yin P (2012) Three-Dimensional Structures Self-Assembled from DNA Bricks. *Science* 338(6111):1177-1183.
20. Ke YG*, et al.* (2014) DNA brick crystals with prescribed depths. *Nat Chem* 6(11):994-1002.
21. Rothemund PWK (2006) Folding DNA ro create nanoscale shapes and patterns. *Nature* 440:297-302.
22. Andersen ES*, et al.* (2009) Self-assembly of a nanoscale DNA box with a controllable lid. *Nature* 459(7243):73-U75.
23. Douglas SM*, et al.* (2009) Self-assembly of DNA into nanoscale three-dimensional shapes. *Nature* 459(7245):414-418.
24. Han DR*, et al.* (2011) DNA Origami with Complex Curvatures in Three-Dimensional Space. *Science* 332(6027):342-346.
25. Han DR*, et al.* (2013) DNA Gridiron Nanostructures Based on Four-Arm Junctions. *Science* 339(6126):1412-1415.
26. Mirkin CA, Letsinger RL, Mucic RC, & Storhoff JJ (1996) A DNA-based method for rationally assembling nanoparticles into macroscopic materials. *Nature* 382(6592):607-609.
27. Alivisatos AP*, et al.* (1996) Organization of 'nanocrystal molecules' using DNA. *Nature* 382(6592):609-611.
28. Mirkin CA, Thaxton CS, & Rosi NL (2004) Nanostructures in biodefense and molecular diagnostics. *Expert Rev Mol Diagn* 4(6):749-751.
29. Rosi NL & Mirkin CA (2005) Nanostructures in biodiagnostics. *Chemical Reviews* 105(4):1547-1562.
30. Seferos DS, Giljohann DA, Hill HD, Prigodich AE, & Mirkin CA (2007) Nano-flares: Probes for transfection and mRNA detection in living cells. *J Am Chem Soc* 129(50):15477-+.
31. Rosi NL*, et al.* (2006) Oligonucleotide-modified gold nanoparticles for intracellular gene regulation. *Science* 312(5776):1027-1030.
32. Nykypanchuk D, Maye MM, van der Lelie D, & Gang O (2008) DNA-guided crystallization of colloidal nanoparticles. *Nature* 451(7178):549-552.
33. Park SY*, et al.* (2008) DNA-programmable nanoparticle crystallization. *Nature* 451(7178):553-556.
34. Xiong HM, van der Lelie D, & Gang O (2009) Phase Behavior of Nanoparticles Assembled by DNA Linkers. *Phys Rev Lett* 102(1):-.
35. Macfarlane RJ*, et al.* (2011) Nanoparticle Superlattice Engineering with DNA. *Science* 334(6053):204-208.
36. Carter JD & LaBean TH (2011) Organization of Inorganic Nanomaterials via Programmable DNA Self-Assembly and Peptide Molecular Recognition. *Acs Nano* 5(3):2200-2205.

37. Sebba DS, Mock JJ, Smith DR, LaBean TH, & Lazarides AA (2008) Reconfigurable core-satellite nanoassemblies as molecularly-driven plasmonic switches. *Nano Lett* 8(7):1803-1808.
38. Li Z, Jin RC, Mirkin CA, & Letsinger RL (2002) Multiple thiol-anchor capped DNA-gold nanoparticle conjugates. *Nucleic Acids Res* 30(7):1558-1562.
39. Ouldridge TE, Sulc P, Romano F, Doye JPK, & Louis AA (2013) DNA hybridization kinetics: zippering, internal displacement and sequence dependence. *Nucleic Acids Res* 41(19):8886-8895.
40. Largo J, Starr FW, & Sciortino F (2007) Self-Assemblong DNA Dendrimers: A Numerical Study. *Langmuir* 23:5896-5905.
41. Chi C, Vargas-Lara F, Tkachenko AV, Starr FW, & Gang O (2012) Internal Structure of Nanoparticle Dimers Linked by DNA. *Acs Nano* 6(8):6793-6802.
42. Padovan-Merhar O, Lara FV, & Starr FW (2011) Stability of DNA-linked nanoparticle crystals: Effect of number of strands, core size, and rigidity of strand attachment. *J Chem Phys* 134(24).
43. Lee SK, Maye MM, Zhang YB, Gang O, & van der Lelie D (2009) Controllable g5p-Protein-Directed Aggregation of ssDNA-Gold Nanoparticles. *Langmuir* 25(2):657-660.
44. Licata NA & Tkachenko AV (2008) Dynamics of particles with "key-lock" interactions. *Epl-Europhys Lett* 81(4).
45. Licata NA & Tkachenko AV (2008) How to build nanoblocks using DNA scaffolds. *Epl-Europhys Lett* 84(2).
46. Feng L*, et al.* (2013) Cinnamate-based DNA photolithography. *Nat Mater* 12(8):747-753.
47. Hadorn M*, et al.* (2012) Specific and reversible DNA-directed self-assembly of oil-in-water emulsion droplets. *P Natl Acad Sci USA* 109(50):20320-20325.
48. Kim AJ, Scarlett R, Biancaniello PL, Sinno T, & Crocker JC (2009) Probing interfacial equilibration in microsphere crystals formed by DNA-directed assembly. *Nat Mater* 8(1):52-55.
49. Casey MT*, et al.* (2012) Driving diffusionless transformations in colloidal crystals using DNA handshaking. *Nat Commun* 3.
50. McGinley JT, Jenkins I, Sinno T, & Crocker JC (2013) Assembling colloidal clusters using crystalline templates and reprogrammable DNA interactions. *Soft Matter* 9(38):9119-9128.
51. Valignat MP, Theodoly O, Crocker JC, Russel WB, & Chaikin PM (2005) Reversible self-assembly and directed assembly of DNA-linked micrometer-sized colloids. *P Natl Acad Sci USA* 102(12):4225-4229.
52. Hiddessen AL, Rodgers SD, Weitz DA, & Hammer DA (2000) Assembly of binary colloidal structures via specific biological adhesion. *Langmuir* 16(25):9744-9753.
53. Kim AJ, Biancaniello PL, & Crocker JC (2006) Engineering DNA-mediated colloidal crystallization. *Langmuir* 22(5):1991-2001.
54. Leunissen ME*, et al.* (2009) Switchable self-protected attractions in DNA-functionalized colloids. *Nat Mater* 8(7):590-595.
55. Tang H*, et al.* (2012) Analysis of DNA-Guided Self-Assembly of Microspheres Using Imaging Flow Cytometry. *J Am Chem Soc* 134(37):15245-15248.

56. van der Meulen SAJ & Leunissen ME (2013) Solid Colloids with Surface-Mobile DNA Linkers. *J Am Chem Soc* 135(40):15129-15134.
57. Stell G (1991) Sticky Spheres and Related Systems. *J Stat Phys* 63(5-6):1203-1221.
58. Mekis A*, et al.* (1996) High transmission through sharp bends in photonic crystal waveguides. *Phys Rev Lett* 77(18):3787-3790.
59. Crocker JC, Kim AJ, & Biancaniello P (2003) Programming colloidal interactions with DNA hybridization. *Abstr Pap Am Chem S* 226:U341-U341.
60. Milam VT, Hiddessen AL, Crocker JC, Graves DJ, & Hammer DA (2003) DNA-driven assembly of bidisperse, micron-sized colloids. *Langmuir* 19(24):10317-10323.
61. Grest GS & Kremer K (1986) Molecular-Dynamics Simulation for Polymers in the Presence of a Heat Bath. *Phys Rev A* 33(5):3628-3631.
62. Kremer K & Grest GS (1990) Dynamics of Entangled Linear Polymer Melts - a Molecular-Dynamics Simulation. *J Chem Phys* 92(8):5057-5086.
63. Starr FW & Sciortino F (2006) Model for assembly and gelation of four-armed DNA dendrimers. *J Phys-Condens Mat* 18(26):L347-L353.
64. Stewart KM & McLaughlin LW (2004) Four-arm oligonucleotide Ni(II)-cyclam-centered complexes as precursors for the generation of supramolecular periodic assemblies. *J Am Chem Soc* 126(7):2050-2057.
65. Knorowski C, Burleigh S, & Travesset A (2011) Dynamics and Statics of DNA-Programmable Nanoparticle Self-Assembly and Crystallization. *Phys Rev Lett* 106(21).
66. Ouldridge TE, Louis AA, & Doye JPK (2010) Extracting bulk properties of self-assembling systems from small simulations. *J Phys-Condens Mat* 22(10).
67. Ouldridge TE, Louis AA, & Doye JPK (2011) Structural, mechanical, and thermodynamic properties of a coarse-grained DNA model. *J Chem Phys* 134(8).
68. Scarlett RT, Crocker JC, & Sinno T (2010) Computational analysis of binary segregation during colloidal crystallization with DNA-mediated interactions. *J Chem Phys* 132(23).
69. Leunissen ME & Frenkel D (2011) Numerical study of DNA-functionalized microparticles and nanoparticles: Explicit pair potentials and their implications for phase behavior. *J Chem Phys* 134(8).
70. Mognetti BM, Leunissen ME, & Frenkel D (2012) Controlling the temperature sensitivity of DNA-mediated colloidal interactions through competing linkages. *Soft Matter* 8(7):2213-2221.
71. Sales-Pardo M, Guimera R, Moreira AA, Widom J, & Amaral LAN (2005) Mesoscopic modeling for nucleic acid chain dynamics. *Phys Rev E* 71(5).
72. Kenward M & Dorfman KD (2009) Brownian dynamics simulations of single-stranded DNA hairpins. *J Chem Phys* 130(9).
73. Drukker K, Wu GS, & Schatz GC (2001) Modes simulations of DNA denaturation dynamics. *J Chem Phys* 114(1):579-590.
74. Sambriski EJ, Schwartz DC, & de Pablo JJ (2009) Uncovering pathways in DNA oligonucleotide hybridization via transition state analysis. *P Natl Acad Sci USA* 106(43):18125-18130.
75. Sambriski EJ, Schwartz DC, & de Pablo JJ (2009) A Mesoscale Model of DNA and Its Renaturation. *Biophys J* 96(5):1675-1690.

76. Lukatsky DB & Frenkel D (2004) Phase behavior and selectivity of DNA-linked nanoparticle assemblies. *Phys Rev Lett* 92(6).
77. Lukatsky DB & Frenkel D (2005) Surface and bulk dissolution properties, and selectivity of DNA-linked nanoparticle assemblies. *J Chem Phys* 122(21):-.
78. Martinez-Veracoechea FJ, Mladek BM, Tkachenko AV, & Frenkel D (2011) Design Rule for Colloidal Crystals of DNA-Functionalized Particles. *Phys Rev Lett* 107(4).
79. Martinez-Veracoechea FJ, Bozorgui B, & Frenkel D (2010) Anomalous phase behavior of liquid-vapor phase transition in binary mixtures of DNA-coated particles. *Soft Matter* 6(24):6136-6145.
80. Largo J, Tartaglia P, & Sciortino F (2007) Effective nonadditive pair potential for lock-and-key interacting particles: The role of the limited valence. *Phys Rev E* 76(1).
81. Theodorakis PE, Dellago C, & Kahl G (2013) A coarse-grained model for DNA-functionalized spherical colloids, revisited: Effective pair potential from parallel replica simulations. *J Chem Phys* 138(2).
82. Rogers WB & Crocker JC (2011) Direct measurements of DNA-mediated colloidal interactions and their quantitative modeling. *P Natl Acad Sci USA* 108(38):15687-15692.
83. Leunissen ME, Dreyfus R, Sha R, Seeman NC, & Chaikin PM (2010) Quantitative Study of the Association Thermodynamics and Kinetics of DNA-Coated Particles for Different Functionalization Schemes. *J Am Chem Soc* 132(6):1903-1913.
84. Mognetti BM*, et al.* (2012) Predicting DNA-mediated colloidal pair interactions. *P Natl Acad Sci USA* 109(7):E378-E379.
85. Rogers WB & Crocker JC (2012) Reply to Mognetti et al.: DNA handshaking interaction data are well described by mean-field and molecular models. *P Natl Acad Sci USA* 109(7):E380-E380.
86. Knorowski C & Travesset A (2011) Materials design by DNA programmed self-assembly. *Curr Opin Solid St M* 15(6):262-270.
87. Lara FV & Starr FW (2011) Stability of DNA-linked nanoparticle crystals I: Effect of linker sequence and length. *Soft Matter* 7(5):2085-2093.
88. Dai W, Hsu CW, Sciortino F, & Starr FW (2010) Valency Dependence of Polymorphism and Polyamorphism in DNA-Functionalized Nanoparticles. *Langmuir* 26(5):3601-3608.
89. Murphy MC, Rasnik I, Cheng W, Lohman TM, & Ha TJ (2004) Probing single-stranded DNA conformational flexibility using fluorescence spectroscopy. *Biophys J* 86(4):2530-2537.
90. Biancaniello PL, Kim AJ, & Crocker JC (2005) Colloidal interactions and self-assembly using DNA hybridization. *Phys Rev Lett* 94(5):-.
91. Licata NA & Tkachenko AV (2006) Statistical mechanics of DNA-mediated colloidal aggregation. *Phys Rev E* 74(4).
92. Dreyfus R*, et al.* (2010) Aggregation-disaggregation transition of DNA-coated colloids: Experiments and theory. *Phys Rev E* 81(4).
93. Crocker JC, Biancaniello P, & Kim AJ (2004) Measuring and modeling weak adhesion between DNA-grafted colloids. *Abstr Pap Am Chem S* 228:U489-U489.
94. Crocker JC, Kim AJ, Biancaniello P, Scarlett R, & Sinno TR (2007) PHYS 235-Colloidal crystallization, kinetics and interactions due to DNA hybridization. *Abstr Pap Am Chem S* 234.

95. Crocker JC (2008) Nanomaterials: Golden handshake. *Nature* 451(7178):528-529.
96. Rogers WB, Sinno T, & Crocker JC (2013) Kinetics and non-exponential binding of DNA-coated colloids. *Soft Matter* 9(28):6412-6417.
97. Mangonon PL & Thomas G (1970) Martensite Phases in 304 Stainless Steel. *Metall Trans* 1(6):1577-&.
98. Shaw JA & Kyriakides S (1995) Thermomechanical Aspects of Niti. *J Mech Phys Solids* 43(8):1243-1281.
99. Scarlett RT, Ung MT, Crocker JC, & Sinno T (2011) A mechanistic view of binary colloidal superlattice formation using DNA-directed interactions. *Soft Matter* 7(5):1912-1925.
100. Zhang C*, et al.* (2013) A general approach to DNA-programmable atom equivalents. *Nat Mater* 12(8):741-746.
101. Speer JG, Hackenberg RE, Decooman BC, & Matlock DK (2007) Influence of interface migration during annealing of martensite/austenite mixtures. *Phil Mag Lett* 87(6):379-382.
102. Plimpton S (1995) Fast Parallel Algorithms for Short-Range Molecular-Dynamics. *J Comput Phys* 117(1):1-19.
103. Stewart J (2003) *Calculus* (Thomson Brooks/Cole, Belmont, CA) 5. Ed pp xxv, 1204, A1136, 1210 s. +.
104. Barkwell L & Lancaster P (1992) Overdamped and Gyroscopic Vibrating Systems. *J Appl Mech-T Asme* 59(1):176-181.
105. Holmes-Cerfon M, Gortler SJ, & Brenner MP (2013) A geometrical approach to computing free-energy landscapes from short-ranged potentials. *P Natl Acad Sci USA* 110(1):E5-E14.
106. Bitzek E, Koskinen P, Gahler F, Moseler M, & Gumbsch P (2006) Structural relaxation made simple. *Phys Rev Lett* 97(17).
107. Bain EC & Dunkirk N (1924) The nature of martensite. *trans. AIME* 70(1):25-35.
108. Pasquino R, Snijkers F, Grizzuti N, & Vermant J (2010) Directed Self-Assembly of Spheres into a Two-Dimensional Colloidal Crystal by Viscoelastic Stresses. *Langmuir* 26(5):3016-3019.
109. Allen MP & Tildesley DJ (1987) *Computer Simulation of Liquids* (Oxford University Press Inc., New York).
110. Schmitz R & Felderhof BU (1982) Mobility Matrix for 2 Spherical-Particles with Hydrodynamic Interaction. *Physica A* 116(1-2):163-177.
111. Reuland P, Felderhof BU, & Jones RB (1978) Hydrodynamic Interaction of 2 Spherically Symmetric Polymers. *Physica A* 93(3-4):465-475.
112. Kegel WK & van Blaaderen A (2000) Direct observation of dynamical heterogeneities in colloidal hard-sphere suspensions. *Science* 287(5451):290-293.
113. Chen K*, et al.* (2010) Low-Frequency Vibrations of Soft Colloidal Glasses. *Phys Rev Lett* 105(2).
114. Zhang ZX, Yunker PJ, Habdas P, & Yodh AG (2011) Cooperative Rearrangement Regions and Dynamical Heterogeneities in Colloidal Glasses with Attractive Versus Repulsive Interactions. *Phys Rev Lett* 107(20).
115. Wang YF*, et al.* (2012) Colloids with valence and specific directional bonding. *Nature* 491(7422):51-U61.

116. Li WW*, et al.* (2012) Synthesis and characterization of highly dispersed TiO2 nanocrystal colloids by microwave-assisted hydrothermal method. *J Mater Sci* 47(23):7999-8006.
117. Shen CY*, et al.* (2012) Application of DLVO Energy Map To Evaluate Interactions between Spherical Colloids and Rough Surfaces. *Langmuir* 28(41):14681-14692.
118. Shen CY*, et al.* (2012) Theoretical and experimental investigation of detachment of colloids from rough collector surfaces. *Colloid Surface A* 410:98-110.
119. Di Michele L*, et al.* (2013) Multistep kinetic self-assembly of DNA-coated colloids. *Nat Commun* 4.
120. Knorowski C & Travesset A (2012) Dynamics of DNA-programmable nanoparticle crystallization: gelation, nucleation and topological defects. *Soft Matter* 8(48):12053-12059.
121. Wang Z, Chen JW, Li XH, Shao JP, & Peijnenburg WJGM (2012) Aquatic toxicity of nanosilver colloids to different trophic organisms: Contributions of particles and free silver ion. *Environ Toxicol Chem* 31(10):2408-2413.
122. Biancaniello PL, Crocker JC, Hammer DA, & Milam VT (2007) DNA-mediated phase behavior of microsphere suspensions. *Langmuir* 23(5):2688-2693.
123. Sreelakshmi Y*, et al.* (2010) NEATTILL: A simplified procedure for nucleic acid extraction from arrayed tissue for TILLING and other high-throughput reverse genetic applications. *Plant Methods* 6.
124. Varrato F*, et al.* (2012) Arrested demixing opens route to bigels. *P Natl Acad Sci USA* 109(47):19155-19160.
125. Lu PJ*, et al.* (2008) Gelation of particles with short-range attraction. *Nature* 453:499-504.
126. Linehan WM, Srinivasan R, & Schmidt LS (2010) The genetic basis of kidney cancer: a metabolic disease. *Nat Rev Urol* 7(5):277-285.
127. Di Michele L & Eiser E (2013) Developments in understanding and controlling self assembly of DNA-functionalized colloids. *Phys Chem Chem Phys* 15(9):3115-3129.
128. Liao F, Wang ZF, Guo TT, Zhang TT, & Wu ZP (2012) Synthesis of well dispersed palladium nanoparticles-decorated poly(o-phenylenediamine) colloids with excellent performance for hydrazine oxidation. *J Electroanal Chem* 673:38-42.
129. Shen CY, Wang LP, Li BG, Huang YF, & Jin Y (2012) Role of Surface Roughness in Chemical Detachment of Colloids Deposited at Primary Energy Minima. *Vadose Zone J* 11(1).
130. Wang HR*, et al.* (2012) Mechanism of supported bilayer formation of zwitterionic lipids on SiO2 nanoparticles and structure of the stable colloids. *Rsc Adv* 2(30):11336-11348.
131. Deo R*, et al.* (2013) Common genetic variation near the connexin-43 gene is associated with resting heart rate in African Americans: A genome-wide association study of 13,372 participants. *Heart Rhythm* 10(3):401-408.
132. Yuvaraj S*, et al.* (2013) Genetic and antigenic characterization of Indian foot-and-mouth disease virus serotype O isolates collected during the period 2001 to 2012. *Infect Genet Evol* 13:109-115.
133. McArthur HL*, et al.* (2007) Cardiac safety of adjuvant bevacizumab plus dose-dense doxorubicin/cyclophosphamide followed by nanoparticle albumin-bound paclitaxel in patients with early stage breast cancer. *Breast Cancer Res Tr* 106:S147-S148.
134. von Maltzahn G*, et al.* (2007) Nanoparticle self-assembly directed by antagonistic kinase and phosphatase activities. *Adv Mater* 19(21):3579-+.

135. Savage JR, Blair DW, Levine AJ, Guyer RA, & Dinsmore AD (2006) Imaging the sublimation dynamics of colloidal crystallites. *Science* 314:795.
136. Baranzini SE*, et al.* (2010) Genetic variation influences glutamate concentrations in brains of patients with multiple sclerosis. *Brain* 133:2603-2611.
137. Maroudam V, Nagendrakumar SB, Rangarajan PN, Thiagarajan D, & Srinivasan VA (2010) Genetic characterization of Indian type O FMD virus 3A region in context with host cell preference. *Infect Genet Evol* 10(5):703-709.
138. Xi E, Remsing RC, & Patel AJ (2016) Sparse Sampling of Water Density Fluctuations in Interfacial Environments. *Journal of chemical theory and computation*.
139. Auer S & Frenkel D (2005) Numerical simulation of crystal nucleation in colloids. *Advanced Computer Simulation Approaches for Soft Matter Sciences I* 173:149-208.
140. Steinhardt PJ, Nelson DR, & Ronchetti M (1983) Bond-Orientational Order in Liquids and Glasses. *Phys Rev B* 28(2):784-805.
141. Steinhardt PJ, Nelson DR, & Ronchetti M (1981) Icosahedral Bond Orientational Order in Supercooled Liquids. *Phys Rev Lett* 47(18):1297-1300.
142. Frenkel D & Smit B (2002) *Understanding Molecular Simulation* (Academic Press, New York).
143. Srinivasan B*, et al.* (2013) Designing DNA-grafted particles that self-assemble into desired crystalline structures using the genetic algorithm. *P Natl Acad Sci USA* 110(46):18431-18435.
144. Almarza NG & Lomba E (2003) Determination of the interaction potential from the pair distribution function: An inverse Monte Carlo technique. *Phys Rev E* 68(1).
145. Tersoff J (1986) New empirical model for the structural properties of silicon. *Phys Rev Lett* 56(6):632.
146. Cohen AJ, Mori-Sánchez P, & Yang W (2011) Challenges for density functional theory. *Chemical Reviews* 112(1):289-320.
147. Schueler-Furman O, Wang C, Bradley P, Misura K, & Baker D (2005) Progress in modeling of protein structures and interactions. *Science* 310(5748):638-642.
148. Skinner A & Pettifor D (1991) Transferability and the pair potential within the tight-binding bond model: an analytic study for hydrogen. *Journal of Physics: Condensed Matter* 3(13):2029.
149. Tersoff J (1986) New Empirical-Model for the Structural-Properties of Silicon. *Phys Rev Lett* 56(6):632-635.
150. Schröder K-P & Sauer J (1996) Potential functions for silica and zeolite catalysts based on ab initio calculations. 3. A shell model ion pair potential for silica and aluminosilicates. *The Journal of Physical Chemistry* 100(26):11043-11049.
151. Finnis M & Sinclair J (1984) A simple empirical N-body potential for transition metals. *Philosophical Magazine A* 50(1):45-55.
152. Hulburt HM & Hirschfelder JO (1941) Potential energy functions for diatomic molecules. *The Journal of Chemical Physics* 9(1):61-69.
153. Casanova G, Dulla R, Jonah D, Rowlinson J, & Saville G (1970) Effective pair potentials in fluids in the presence of three-body forces. *Mol Phys* 18(5):589-606.
154. Dymond J & Alder B (1969) Pair potential for argon. *The Journal of Chemical Physics* 51(1):309-320.

155. Böhm H, McDonald I, & Madden P (1983) An effective pair potential for liquid acetonitrile. *Mol Phys* 49(2):347-360.
156. Gough D, Smith E, & Maitland G (1974) The pair potential energy function for krypton. *Mol Phys* 27(4):867-872.
157. Dharma-Wardana M & Aers G (1983) Determination of the pair potential and the ion-electron pseudopotential for aluminum from experimental structure-factor data for liquid aluminum. *Phys Rev B* 28(4):1701.
158. Brennan M, Hutchinson P, Sangster M, & Schofield P (1974) Calculation of an effective pair interaction potential for liquid neon from structure factor measurements. *Journal of Physics C: Solid State Physics* 7(23):L411.
159. Bellissent-Funel M, Chieux P, Levesque D, & Weis J (1989) Structure factor and effective two-body potential for liquid gallium. *Phys Rev A* 39(12):6310.
160. Almarza NG, Lomba E, & Molina D (2004) Determination of effective pair interactions from the structure factor. *Phys Rev E* 70(2):021203.
161. Watanabe K & Klein ML (1989) Effective pair potentials and the properties of water. *Chemical Physics* 131(2):157-167.
162. Vondermassen K, Bongers J, Mueller A, & Versmold H (1994) Brownian-Motion - a Tool to Determine the Pair Potential between Colloid Particles. *Langmuir* 10(5):1351-1353.
163. Reatto L, Levesque D, & Weis JJ (1986) Iterative Predictor-Corrector Method for Extraction of the Pair Interaction from Structural Data for Dense Classical Liquids. *Phys Rev A* 33(5):3451-3465.
164. Barocchi F, Zoppi M, & Egelstaff PA (1985) Density Analysis of the Neutron Structure Factor and the Determination of the Pair Potential of Krypton. *Phys Rev A* 31(4):2732-2735.
165. Jorgensen WL, Chandrasekhar J, Madura JD, Impey RW, & Klein ML (1983) Comparison of simple potential functions for simulating liquid water. *The Journal of chemical physics* 79(2):926-935.
166. Israelachvili JN & Adams GE (1978) Measurement of Forces between 2 Mica Surfaces in Aqueous-Electrolyte Solutions in Range 0-100 Nm. *J Chem Soc Farad T 1* 74:975-&.
167. Ducker WA, Senden TJ, & Pashley RM (1991) Direct Measurement of Colloidal Forces Using an Atomic Force Microscope. *Nature* 353(6341):239-241.
168. Prieve DC & Frej NA (1990) Total Internal-Reflection Microscopy - a Quantitative Tool for the Measurement of Colloidal Forces. *Langmuir* 6(2):396-403.
169. Walz JY (1997) Measuring particle interactions with total internal reflection microscopy. *Current opinion in colloid & interface science* 2(6):600-606.
170. Bevan MA & Prieve DC (1999) Direct measurement of retarded van der Waals attraction. *Langmuir* 15(23):7925-7936.
171. Wu H-J, Pangburn TO, Beckham RE, & Bevan MA (2005) Measurement and interpretation of particle-particle and particle-wall interactions in levitated colloidal ensembles. *Langmuir* 21(22):9879-9888.
172. Fernandes GE, Beltran-Villegas DJ, & Bevan MA (2008) Interfacial Colloidal Crystallization via Tunable Hydrogel Depletants. *Langmuir* 24(19):10776-10785.
173. Furst EM & Gast AP (2000) Dynamics and lateral interactions of dipolar chains. *Phys Rev E* 62(5):6916-6925.

174. Crocker JC, Matteo JA, Dinsmore AD, & Yodh AG (1999) Entropic attraction and repulsion in binary colloids probed with a line optical tweezer. *Phys Rev Lett* 82(21):4352-4355.
175. Brunner M, Dobnikar J, von Grünberg H-H, & Bechinger C (2004) Direct measurement of three-body interactions amongst charged colloids. *Phys Rev Lett* 92(7):078301.
176. Polin M, Roichman Y, & Grier DG (2008) Autocalibrated colloidal interaction measurements with extended optical traps. *Phys Rev E* 77(5).
177. Kong YP & Parthasarathy R (2010) Different Modulation Mechanisms of Attractive Colloidal Interactions by Lipid and Protein Functionalization. *Langmuir* 26(13):10541-10545.
178. Rogers WB & Crocker JC (2014) A tunable line optical tweezers instrument with nanometer spatial resolution. *Rev Sci Instrum* 85(4).
179. Crocker JC & Grier DG (1994) Microscopic Measurement of the Pair Interaction Potential of Charge-Stabilized Colloid. *Phys Rev Lett* 73(2):352-355.
180. Sainis SK, Germain V, & Dufresne ER (2007) Statistics of particle trajectories at short time intervals reveal fN-scale colloidal forces. *Phys Rev Lett* 99(1).
181. Kepler GM & Fraden S (1994) Attractive Potential between Confined Colloids at Low Ionic-Strength. *Phys Rev Lett* 73(2):356-359.
182. Han YL & Grier DG (2003) Confinement-induced colloidal attractions in equilibrium. *Phys Rev Lett* 91(3).
183. Iacovella CR, Rogers RE, Glotzer SC, & Solomon MJ (2010) Pair interaction potentials of colloids by extrapolation of confocal microscopy measurements of collective suspension structure. *The Journal of chemical physics* 133(16):164903.
184. Jenkins IC, Crocker JC, & Sinno T (2015) Interaction potentials from arbitrary multi-particle trajectory data. *Soft Matter* 11(35):6948-6956.
185. Ercolessi F & Adams JB (1994) Interatomic potentials from first-principles calculations: the force-matching method. *EPL (Europhysics Letters)* 26(8):583.
186. Izvekov S & Voth GA (2005) Multiscale coarse graining of liquid-state systems. *The Journal of chemical physics* 123(13):134105.
187. Izvekov S, Parrinello M, Burnham CJ, & Voth GA (2004) Effective force fields for condensed phase systems from ab initio molecular dynamics simulation: a new method for force-matching. *The Journal of chemical physics* 120(23):10896-10913.
188. Izvekov S, Violi A, & Voth GA (2005) Systematic coarse-graining of nanoparticle interactions in molecular dynamics simulation. *The Journal of Physical Chemistry B* 109(36):17019-17024.
189. Das A & Andersen HC (2009) The multiscale coarse-graining method. III. A test of pairwise additivity of the coarse-grained potential and of new basis functions for the variational calculation. *The Journal of chemical physics* 131(3):034102.
190. Umeno Y, Kitamura T, Date K, Hayashi M, & Iwasaki T (2002) Optimization of interatomic potential for Si/SiO 2 system based on force matching. *Computational materials science* 25(3):447-456.
191. Li Y, Siegel DJ, Adams JB, & Liu X-Y (2003) Embedded-atom-method tantalum potential developed by the force-matching method. *Phys Rev B* 67(12):125101.

192. Wei D, Song Y, & Wang F (2011) A simple molecular mechanics potential for μm scale graphene simulations from the adaptive force matching method. *The Journal of chemical physics* 134(18):184704.
193. Hoogerbrugge P & Koelman J (1992) Simulating microscopic hydrodynamic phenomena with dissipative particle dynamics. *EPL (Europhysics Letters)* 19(3):155.
194. Botto L, Lewandowski EP, Cavallaro M, & Stebe KJ (2012) Capillary interactions between anisotropic particles. *Soft Matter* 8(39):9957-9971.
195. Pangburn TO & Bevan MA (2006) Anomalous potentials from inverse analyses of interfacial polydisperse attractive colloidal fluids. *The Journal of chemical physics* 124(5):054712.